

**Electronic and Optical Properties  
of Silicon Nanocrystals:  
a Tight Binding Study**

Fabio Trani

November 30, 2004



# Contents

<b>Introduction</b>	<b>5</b>
<b>1 Tight Binding method</b>	<b>9</b>
1.1 Introduction . . . . .	9
1.2 The model . . . . .	11
1.3 Empirical pseudopotentials . . . . .	16
1.4 Parametrizations . . . . .	19
<b>2 Linear Response Theory</b>	<b>29</b>
2.1 Introduction . . . . .	29
2.2 Response of a crystal to an external field . . . . .	30
2.3 Interaction picture and correlation functions . . . . .	34
2.4 The dielectric tensor . . . . .	37
2.5 Linear response and TB . . . . .	42
2.6 The approximation . . . . .	45
2.7 The charge conservation . . . . .	47
2.8 Results . . . . .	50
<b>3 Spherical nanocrystals</b>	<b>55</b>
3.1 Introduction . . . . .	55

3.2	The method . . . . .	56
3.3	Energy levels . . . . .	59
3.4	Dielectric function . . . . .	63
3.5	Oscillator strengths . . . . .	67
3.6	k-space projections . . . . .	69
3.7	Dielectric constant . . . . .	72
<b>4</b>	<b>Ellipsoidal nanocrystals</b>	<b>75</b>
4.1	Introduction . . . . .	75
4.2	Porous Silicon Photoluminescence . . . . .	76
4.3	Silicon ellipsoids . . . . .	78
4.4	Dielectric properties . . . . .	82
4.5	Energy levels of large ellipsoids . . . . .	89
	<b>Conclusions</b>	<b>99</b>
	<b>A Symmetries</b>	<b>103</b>
	<b>B Character Tables</b>	<b>107</b>
	<b>Acknowledgments</b>	<b>111</b>
	<b>Bibliography</b>	<b>120</b>

# Introduction

The scientific field of silicon nanostructures is a fascinating area of material science. It has a huge technological impact, because of the fundamental role of silicon in the microelectronic revolution which has changed our everyday lives. On the other side, silicon is a very bad luminescent material. It is characterized by an indirect, low energy fundamental band gap. And this means that silicon shows very long radiative electron-hole recombination lifetimes, so that non-radiative recombination paths are preferred, even at cryogenic temperatures. In the past years, it became clear that silicon nanocrystals behave in a completely different way. The chance of tuning the optical band gap and the radiative recombination lifetime with the nanocrystal size is known as the quantum confinement effect, and is a simple consequence of the quantum mechanics rules. Nevertheless, the construction in labs all over the world of nanocrystals with a strong photoluminescence in the entire optical range, have astonished the whole community of solid state scientists. The research of the last decade has been devoted to the attempts of having light-emitting silicon devices. Using both the lithographic-epitaxial and the chemical synthesis techniques, the fabrication of silicon nanocrystals have had an enormous progress in the last years, and sharper and sharper nanocrystal size distributions have been obtained. An important goal was the discovery

of a strong photoluminescence from porous silicon, which constituted a very easy and economic way for having high-performance photoluminescent silicon structures. Recently, the discovery of optical gain from silicon nanocrystals have suggested the possibility of a silicon-based laser technology.

From the theoretical point of view, still today the subject is not completely clear. While the quantum confinement effect has been recognized as the major cause of the photoluminescence, many doubts remain on the way in which the phenomenon takes place. This thesis is the result of a deep work in the understanding of the optical properties of silicon nanocrystals. The first part of the thesis is dedicated to the making-up of the theoretical model. The first chapter concerns the Tight Binding method, used in this work for the study of the nanocrystals. The advantages in the use of such a method lies in its huge efficiency: Tight Binding is the only method able to study both small and very large nanocrystals. In fact, its short range interaction parameters lead to nanocrystal Hamiltonian matrices really very sparse. This feature has been used through a diagonalization routine having a computational time which scales linearly with the matrix size. The second chapter is dedicated to a review of the linear response theory, and to the extension of the Tight Binding method to the study of the dielectric properties of a crystalline structure. This is not a trivial matter, in that the method does not easily allow an explicit knowledge of the basis wave functions. The method that we have chosen seems to work very well for the Bulk Silicon. The second part of this thesis is dedicated to the results. In the third chapter, the optical properties of spherical nanocrystals are illustrated. A comparison with the experimental results and the other calculation tools are discussed

in detail. The optical gap, the imaginary part of the dielectric function, the static dielectric function, and the radiative electron-hole recombination times have been calculated. An interesting feature is the existence of an energy gap between the energy of the first transition and the threshold of the absorption cross section. This is an indication that the electronic features of the bulk silicon are always reflected into the silicon nanocrystal physics. A very nice confirmation of this trend is the  $k$ -space projection of the nanocrystal states, which gives a fair explanation of this phenomenon. In the last chapter the shape effects on the optical properties are shown. Several sets of ellipsoidal nanocrystals, with different sizes and shapes, have been analyzed, and the effects of the geometrical anisotropy on the polarization of the dielectric tensor is discussed.



# Chapter 1

## Tight Binding method

### 1.1 Introduction

Since the fundamental paper of Slater and Koster (SK) [1], the Tight Binding interpolation scheme (TB) has been a powerful tool for electronic spectra and density of states calculations of crystalline structures. The method is based on the expansion of the wave functions into linear combinations of atomic orbitals (LCAO), with Hamiltonian matrix elements parametrized in such a way to reproduce first-principles calculations and/or experimental data. Compared to the methods based on the Plane Wave basis sets (PW), the TB scheme is very efficient in problems where localized functions are required. In fact, the method has been widely used especially in impurity states calculations [2], where it is computationally advantageous because it only needs a small number of localized orbitals. Over the years, many variants of the TB have been developed, based on different kinds of parametrizations, and the possibilities of the method have been extended beyond the simple band structure calculations [3]. An interesting field has concerned the study

of the TB parameters transferability [4], that allows the method to be used in structural optimization problems. Nowadays, total energy calculations and Monte Carlo simulations [5, 6] are currently performed within the TB formalism.

With the increasing of computer performances, *ab initio* TB models have been attracting a great interest. In fact, the TB interpolation schemes are empirical tools, often called *Empirical Tight Binding*, in which we usually do not have an explicit knowledge of neither the basis functions, nor the real space Hamiltonian. On the other hand, the *ab initio* approaches are based on the explicit construction of both the localized atomic orbitals and the Hamiltonian matrix elements. The *ab-initio* TB models can be very accurate and powerful, but they are computationally more demanding. Therefore, for the great simplicity of the original SK formulation, and the huge precision reached in getting accurate band structures, the Empirical TB models are still today very attractive calculation tools.

In this chapter, we discuss the ETB scheme as it is usually used in band structure calculations. As a first step, in the next section the method will be illustrated, according to the usual Slater-Koster scheme. Then, a brief description of the Empirical Pseudopotential method (PP), often used as an important comparison scheme, will be given, trying to explain the reasons for its great efficiency for the bulk structures, and the huge computational effort that it requires for the nanocrystals. After this, we will compare several TB parametrizations available in literature for the crystalline silicon, the material of major interest in this thesis. Finally, a comparison with the experimental data of gap energies and effective masses will be shown.

## 1.2 The model

The starting point of every Tight Binding model is the definition of a suitable set of atomic-like orbitals. In the following we shall only consider bulk crystalline structures, with atoms located in the positions of a Bravais lattice with a basis; we indicate with  $\mathbf{R}$  the lattice vectors, and  $\boldsymbol{\mu}$  the atomic positions within the unit cell. Therefore, all the atoms contained in the structure lie in the positions:

$$\mathbf{R}_\mu \equiv \mathbf{R} + \boldsymbol{\mu}. \quad (1.1)$$

In the case of the bulk silicon (diamond structure), the Bravais lattice is an FCC and there are two atoms in the unit cell, whose positions are:

$$\boldsymbol{\mu} = \mathbf{0}, \mathbf{d}, \quad (1.2)$$

where  $\mathbf{d} = \frac{a}{4}(1, 1, 1)^1$ , and  $a$  is the lattice length.

The TB orbitals are localized at the atomic positions, and they are usually chosen in such a way to transform into each other under the crystal point group operations, according to a suitable irreducible representation (see Appendix (A) for more details on symmetries). Each orbital is characterized by a quantum number  $\sigma$ , which labels its transformation properties. We use the Dirac notation to represent orbitals, so we write

$$|\sigma\boldsymbol{\mu}\mathbf{R}\rangle \quad (1.3)$$

to label an orbital centered at the atomic position  $\mathbf{R} + \boldsymbol{\mu}$ , having  $\sigma$  symmetry. A possible basis set for the study of a bulk structure is obtained from the orbitals of the isolated, non interacting atoms. This choice leads to a

---

<sup>1</sup> We are using the standard, cubic coordinate system.

TB model, which is based on functions having the full rotational symmetry<sup>2</sup>, which are symmetric by inversion, and where  $\sigma$  labels the quantum numbers of the single atom states ( $nlmm_s$ ). In the case of the silicon, which is a crystal with a single atomic species, this method allows us to choose the basis set so that *all* the crystal orbitals are obtained by translations of those orbitals located in the coordinate origin. This simple method is very nice in that the basis orbitals have the symmetry of the whole rotation group (they are eigenstates of the atomic angular momentum operators). On the other side, it has the disadvantage that the basis functions are not orthogonal. For this reason, at least two kinds of parameters must be used: Hamiltonian matrix elements and overlap parameters. The difficulty of this non-orthogonal TB scheme [1] is in the large number of parameters that enter the fitting procedure, so that it is difficult to include interactions up to many neighbors without doing suitable approximations [7]. Another complication arises from the fact that the energy levels are solutions of a generalized eigenvalue problem. This is not a big problem in crystalline structures, where we always have a small number of orbitals in the unit cell. But this can give troubles in nanostructures, by increasing the computational time, when the Hamiltonian matrices become very large.

The use of an orthogonal basis set simplifies both the fitting and the Hamiltonian diagonalization procedures. Starting from a non-orthogonal basis set, a smart orthogonalization procedure can be performed, as it was shown by Löwdin [8], in such a way that the resulting orbitals maintain the same transformation properties of the original basis set under the space

---

<sup>2</sup> Of course, only in the hypothesis of neglecting the small non central corrections to the isolated atom Hamiltonian, the angular momentum is a good quantum number, and we can choose atomic functions with the full rotational symmetry.

group operations [1]. The as-built *Löwdin's orbitals* usually have a lower symmetry than the original functions. If we start from a set of eigenstates of the angular momentum operators of the isolated atoms, after the orthogonalization procedure we obtain a new set of orbitals which are symmetric only with respect to those (discrete) rotations which transform the crystal atoms into each other. And so, we eventually retrieve a basis set which is not symmetric with respect to the full rotational group. Moreover, if the point group is not symmorphic [9] (there are transformations associated to fractional translations, see Appendix (A)), there are couples of orbitals which belong to different sublattices that can be no longer related to each other through a simple spatial translation. In effect, this is the situation for the bulk silicon, where Löwdin's orbitals do not have the inversion symmetry, since the inversion is related to a fractional translation (when the origin has been taken on a silicon atom). The inversion operation plus the fractional translation transforms into each other the orbitals which belong to different sublattices.

In the Orthogonal TB model, the basis set is constituted by Löwdin's orbitals, and we have:

$$\langle \sigma \boldsymbol{\mu} \mathbf{R} | \sigma' \boldsymbol{\mu}' \mathbf{R}' \rangle = \delta_{\sigma\sigma'} \delta_{\boldsymbol{\mu}\boldsymbol{\mu}'} \delta_{\mathbf{R}\mathbf{R}'}. \quad (1.4)$$

The only parameters we need for electronic spectra calculations are the Hamiltonian matrix elements, that we label as

$$H_{\sigma\sigma'}^{\boldsymbol{\mu}\boldsymbol{\mu}'}(\mathbf{R}'_{\boldsymbol{\mu}'} - \mathbf{R}_{\boldsymbol{\mu}}) \equiv \langle \sigma \boldsymbol{\mu} \mathbf{R} | \hat{H} | \sigma' \boldsymbol{\mu}' \mathbf{R}' \rangle. \quad (1.5)$$

As usual in the study of the crystalline structures, we construct a basis set of Bloch sums, in order to take into account the translational symmetry of

the lattice. In our scheme we obtain the following orthogonal states:

$$|\sigma\boldsymbol{\mu}\mathbf{k}\rangle = \frac{1}{\sqrt{N}} \sum_{\mathbf{R}} e^{i\mathbf{k}\cdot(\mathbf{R}+\boldsymbol{\mu})} |\sigma\boldsymbol{\mu}\mathbf{R}\rangle, \quad (1.6)$$

in which  $N$  is the number of lattice sites included into the sum. These functions are invariant (up to a phase factor) by lattice translations, and therefore they form a basis set in which the Hamiltonian operator  $\hat{H}$  is diagonal with respect to  $\mathbf{k}$ . The Hamiltonian matrix in this new basis set is easily computed starting from the interaction parameters defined in Eq. (1.5) :

$$H_{\sigma\sigma'}^{\boldsymbol{\mu}\boldsymbol{\mu}'}(\mathbf{k}) \equiv \langle\sigma\boldsymbol{\mu}\mathbf{k}|H|\sigma'\boldsymbol{\mu}'\mathbf{k}\rangle = \sum_{\mathbf{R}} e^{i\mathbf{k}\cdot(\mathbf{R}+\boldsymbol{\mu}'-\boldsymbol{\mu})} \langle\sigma\boldsymbol{\mu}\mathbf{0}|H|\sigma'\boldsymbol{\mu}'\mathbf{R}\rangle \quad (1.7)$$

The band structure is now obtained solving the eigenvalue problem for the reciprocal space Hamiltonian matrix of Eq. (1.7), for each  $\mathbf{k}$ -vector lying inside the first Brillouin Zone (BZ):

$$\sum_{\sigma'\boldsymbol{\mu}'} \left[ H_{\sigma\sigma'}^{\boldsymbol{\mu}\boldsymbol{\mu}'}(\mathbf{k}) - E_n(\mathbf{k})\delta_{\sigma\sigma'}\delta_{\boldsymbol{\mu}\boldsymbol{\mu}'} \right] B_{\sigma'n}^{\boldsymbol{\mu}'}(\mathbf{k}) = 0, \quad (1.8)$$

and the crystalline eigenstates come from the expansion

$$|n\mathbf{k}\rangle = \sum_{\sigma\boldsymbol{\mu}} B_{\sigma n}^{\boldsymbol{\mu}}(\mathbf{k}) |\sigma\boldsymbol{\mu}\mathbf{k}\rangle. \quad (1.9)$$

The above procedure only requires the knowledge of the interaction parameters (1.5) in order to calculate the single-electron energy levels of bulk structures. Using symmetries, all these parameters can be reduced to a minimum number. As we shall see later, two factors enter into the definition of a TB scheme: the number of species of atomic orbitals (the values that  $\sigma$  can assume), and the number of nearest neighbors that interact with a single orbital. These two factors determine the number of independent parameters. By the analysis of the crystal, physical reasons can lead to prefer a, we

can say, *horizontal enlargement*, using a small basis set, and interactions up to many neighbors, or a *vertical enlargement*, using a few neighbors but a greater basis set.

Based on a physical ground, approximations can be done in order to reduce the number of parameters. A widely used one is the so called *two-center approximation* [1], that can significantly reduce the number of parameters [10]. The approximation consists in considering the potential energy<sup>3</sup> *invariant by rotations* with respect to the axis connecting the two atoms where the orbitals are located. The problem, in these terms, greatly simplifies, especially for far enough orbitals, in that a number of terms are automatically put equal to zero. The used labelling is that of the diatomic molecule spectra, and all the parameters are reduced to only  $\sigma, \pi \dots$  interactions. In effect, this approximation consists in retaining only that part of the crystalline potential energy which is located in the neighborhood of the two orbitals, and neglecting all the remaining terms (the so-called three center integrals). Some care should be taken in using this approximation, which often can be too rough for a quantitative study of crystals.

After that a suitable set of independent interaction parameters has been chosen, the next step of the Empirical TB scheme is based on calculating them in such a way to fit, after the diagonalization of Eq. (1.8), experimental data and/or *ab initio* calculation results of energy gaps and/or effective masses, in high symmetry k-points.

---

<sup>3</sup> The potential energy enters the interaction parameters in Eq. (1.5). The two center approximation leads to a simplification of the problem, with the reduction of the total number of parameters.

### 1.3 Empirical pseudopotentials

In this section we want to spend a few words on the empirical pseudopotential scheme, that we often use as a comparative computational tool, in order to address the precision of the Tight Binding method. The scheme is based on the expansion of the crystalline eigenstates into Plane Waves, organized in such a way to take into account the translational symmetry of the lattice:

$$|n\mathbf{k}\rangle = \sum_{\mathbf{G}} A_{n\mathbf{k}}(\mathbf{G}) |\mathbf{k} + \mathbf{G}\rangle. \quad (1.10)$$

Here, the sum is done on all the reciprocal lattice vectors  $\mathbf{G}$ , and Plane Waves are defined in real space as:

$$\langle \mathbf{r} | \mathbf{k} + \mathbf{G} \rangle \equiv \frac{1}{\sqrt{V}} e^{i(\mathbf{k} + \mathbf{G}) \cdot \mathbf{r}}, \quad (1.11)$$

where they have been normalized to the crystal volume  $V$ . In the local formulation of the method, the crystalline potential is written as the sum of atomic spherically symmetric contributions  $v(r)$ , so that the single-electron Hamiltonian for silicon is written as:

$$\hat{H} = \frac{\hat{\mathbf{P}}^2}{2m} + \sum_{\mu, \mathbf{R}} v(|\mathbf{r} - \mathbf{R} - \boldsymbol{\mu}|). \quad (1.12)$$

The method is very simple, and the Hamiltonian matrix elements are

$$\langle \mathbf{k} + \mathbf{G} | \hat{H} | \mathbf{k} + \mathbf{G}' \rangle = \frac{\hbar^2}{2m} |\mathbf{k} + \mathbf{G}|^2 \delta_{\mathbf{G}, \mathbf{G}'} + V(\mathbf{G} - \mathbf{G}'), \quad (1.13)$$

where for silicon<sup>4</sup> we have:

$$V(\mathbf{G}) = v(G) \sum_{\boldsymbol{\mu}} e^{-i\mathbf{G} \cdot \boldsymbol{\mu}} = v(G) (1 + e^{-i\mathbf{G} \cdot \mathbf{d}}). \quad (1.14)$$

---

<sup>4</sup> Where we use the atomic positions that we have defined in the previous section.

Here  $v(G)$  is the Fourier transform of the atomic potential. The use of the pseudopotential method as an empirical interpolation scheme consists in using  $v(G)$  as unknown parameters, and fit them in such a way to have a good agreement with the experimental data. The eigenvalue problem is written as:

$$\sum_{\mathbf{G}} \left[ \left( \frac{\hbar^2}{2m} |\mathbf{k} + \mathbf{G}|^2 - E_n(\mathbf{k}) \right) \delta_{\mathbf{G}, \mathbf{G}'} + V(\mathbf{G} - \mathbf{G}') \right] A_{n, \mathbf{k}}(\mathbf{G}) = 0, \quad (1.15)$$

and is characterized by a great simplicity of calculation of the matrix elements. The feasibility of this method is based on how many parameters are needed in order to reproduce a good band structure, as well as on the number of Plane Waves needed to reach the convergence.

The answer was given already many years ago, when it was shown that very few parameters and a not too large basis set succeeded in getting a quite good agreement with the experimental data, for a huge class of semiconductors [11, 12]. The physical motivations of this very nice behavior lie in the idea which is behind a pseudopotential [13]. In semiconductors, the whole space can be divided into a *core* region, quite close to the ions, and an *interstitial* region, constituted by the space between ions. We expect that the lower energy electrons (the so called core electrons), are mainly localized in the core region, while the higher energy electrons (the valence electrons) lie in the interstitial region. It is easy to realize that these latter electrons determines the band structures near the Fermi level, and therefore the optical properties of the crystal.

The explicit form of the potential inside the core region is not important in studying the optical properties, and we can use a fictitious potential (the pseudopotential) which is smoother than the real potential in the core

region, and equal to this one in the interstitial region. It has been widely demonstrated (in many different forms) that such pseudopotentials lead to the same optical properties of the real crystal, but, being very smooth in the core region, they have Fourier transforms  $v(G)$  which rapidly go to zero. Within the Empirical Pseudopotential Method (EPM), in the form it was first proposed [11,12], an excellent band structure of bulk silicon is obtained with *only three* independent parameters. It has been shown that this parameter set is indeed the best choice for taking into account in an effective way all the higher  $G$  contributions [14,15]. Moreover, it has been shown that EPM form factors can be calculated starting from an *ab initio* LDA screened pseudopotential [16]. This theoretical ground is the best reason for using the EPM as a comparative tool.

The method is very nice, elegant and very simple to implement. It does not require a great computational effort for bulk crystals and, more importantly, the convergence with respect to the basis set size is under control. We want to point out that this is a great advantage over the TB models. In fact, within a Pseudopotential method the convergence is obtained in a very simple way, by including into the basis set as many Plane Waves as we need. On the contrary, enlarging a TB basis set is not an easy task, and it is closely related to the parametrization, the number of parameters rapidly increasing with the number of basis functions (the only inclusion of the  $d$  orbitals requires an huge effort).

Unfortunately, the EPM, although very attracting for studying bulk crystals, gives rise to some difficulties when applied to nanostructures [16]. The usual way to study a finite structure within a plane waves approach is that

of building a fictitious periodic system, by placing infinite replicas of the original structure on the sites of a Bravais lattice, and therefore keeping using  $\mathbf{k}$  as a good quantum number. The structure that we want to study constitutes the unit cell (the supercell) of such a fictitious crystal, and the problem is equivalent to the isolated structure problem in the limit of choosing a lattice constant large enough to avoid any interaction between the replicas. The great computational difficulty arises from the necessity of leaving very much vacuum space between two replicas, having indeed very large lattice constants. In order to simulate the annihilation of the nanocrystal wavefunctions inside the vacuum zone, a great number of short-wavelength plane waves must be included into the basis set. On increasing the size of the structure, the supercell size increases, and so the Hamiltonian matrix size. With standard techniques, PW methods can hardly afford the study of nanostructures with more than a few hundreds of atoms. The TB methods, on the contrary, in a natural way take into account the vacuum zone outside the structure. The size of the TB basis set is linear in  $N$ , and this allows to study structures with thousands of atoms with a low computational effort.

## 1.4 Parametrizations

In this section we discuss different kinds of parametrizations currently used in the TB interpolation schemes. We only consider the case of bulk silicon, namely crystals with the diamond structure. The different parametrizations are characterized by the choice of both the basis set, formed by atomic orbitals up to a maximum quantum numbers  $\sigma$ , and the number of neighbors taken into account in the Hamiltonian matrix. These two factors determine

the parameters used for a given scheme.

A first, very simplified model could be an  $sp^3$  TB with nearest neighbor interactions. In this model only Löwdin's orbitals built by the external  $3s$  and  $3p$  silicon atomic states are included into the scheme (minimal basis set). We can label the basis orbitals with  $\sigma = s, x, y, z$ ; with the meaning that  $s$  labels a totalsymmetrical function, while  $(x, y, z)$  label three basis functions of the  $T_{1u}$  irreducible representation of the point group  $O_h$  (Appendix (A)). In this model we only include interactions up to nearest neighbors. Using symmetries, it is not difficult to reduce all the Hamiltonian matrix elements to the six independent parameters<sup>5</sup>:

$$H_{ss}^{\mathbf{00}}(\mathbf{0}), H_{xx}^{\mathbf{00}}(\mathbf{0}), H_{ss}^{\mathbf{0d}}(\mathbf{d}), H_{sx}^{\mathbf{0d}}(\mathbf{d}), H_{xx}^{\mathbf{0d}}(\mathbf{d}), H_{xy}^{\mathbf{0d}}(\mathbf{d}). \quad (1.16)$$

For the sake of simplicity, in the following we shall use  $E, V, W, U$  symbols for on-site, first, second and third nearest neighbors ( $a/4$  units are used for the positions)<sup>6</sup>:

$$E_\sigma \equiv H_{\sigma\sigma'}^{\mathbf{00}}(000), V_{\sigma\sigma'} \equiv H_{\sigma\sigma'}^{\mathbf{0d}}(111), W_{\sigma\sigma'} \equiv H_{\sigma\sigma'}^{\mathbf{00}}(220), U_{\sigma\sigma'} \equiv H_{\sigma\sigma'}^{\mathbf{0d}}(311) \quad (1.17)$$

and in this new notation we write the six parameters for the previous model as:

$$E_s, E_p, V_{ss}, V_{sx}, V_{xx}, V_{xy}. \quad (1.18)$$

This simple model, based on a small set of fitting parameters, has generally failed; in particular, it has been shown that it is not able to reproduce the indirect fundamental gap in silicon [18]. In order to overcome this serious

---

<sup>5</sup> Notation like in Eq. (1.5) has been used.

<sup>6</sup> A similar notation for the TB parameters can be found in the literature [17], with the difference of a multiplicative constant in the definition of the parameters.

problem, Vogl [18] proposed an enlargement of the Löwdin's orbital basis set, including an excited  $s$  state (the so called  $s^*$  state), for each atom. This nearest neighbor  $sp^3s^*$  model requires a greater number of independent parameters than the previous one, and between all the parameters Vogl, on a physical ground, only retained the following:

$$E_s, E_p, E_{s^*}, V_{ss}, V_{sx}, V_{xx}, V_{xy}, V_{s^*x}. \quad (1.19)$$

Based on this larger set of fitting parameters, this model for silicon has been shown to correctly describe not only the energy levels at the  $\Gamma$  point, but the lowest indirect energy gap, and the first conduction band at  $\Delta$  ( $\Gamma - X$ ) and  $\Lambda$  ( $\Gamma - L$ ) lines. On the other side, the behavior of the bands in the proximity of the  $X$  points in directions different from  $\Delta$ , such as the  $Z$  ( $X - W$ ) line, is not good. The largest disagreement is obtained close to the  $W$  point, and along the  $\Sigma$  ( $\Gamma - K$ ) symmetry line. All these discrepancies likely arise from the truncation of the interaction at a very low order of neighbors. We are motivated in thinking that a first neighbor model cannot fair reproduce the band structure in the whole first Brillouin Zone.

The overall behavior of the energy levels is well described by the density of states (DOS). In figure (1.1) the bulk silicon band structure and DOS have been shown, computed both with Vogl model [18] and a Pseudopotential method. All the above considerations can be noticed; in particular it is worth noting that the TB density of states is close to the pseudopotential curve only for the highest energy valence bands. For the unoccupied states, instead, the TB model largely overestimates the pseudopotential density of states. The Vogl model still today is largely used, whereas, as we have just shown, it should be used with care.

Before going ahead, we want to spend a few words on the density of states. For a generic system with  $N_s$  single-electron states, each one having an energy  $E_i$ , we define the density of states at energy  $E$  as<sup>7</sup>:

$$g(E) = \frac{1}{N_s} \sum_i \delta(E - E_i). \quad (1.20)$$

In the case of a bulk crystal, the sum is done on all the  $N_{\mathbf{k}}$  vectors which lie inside the first Brillouin Zone, and all the band complex, getting the final formula:

$$g(E) = \frac{1}{8N_{\mathbf{k}}} \sum_{n,\mathbf{k}} \delta(E - E_n(\mathbf{k})). \quad (1.21)$$

In order to compute the DOS, a grid in the first Brillouin Zone has to be constructed, dense enough to guarantee the convergence of the sum. The simplest way to build the grid consists in choosing periodic boundary conditions for the crystal surface, like the largely used Born-von Karman conditions. In this case, each primitive translation vector  $\mathbf{a}_i$  ( $i = 1, 2, 3$ ) is replied  $N$  times, and one chooses the  $\mathbf{k}$  vectors according to the conditions:

$$e^{iN\mathbf{k}\cdot\mathbf{a}_i} = 1. \quad (1.22)$$

Using values of  $N$  larger and larger, the sum finally converges to its end value. However, there are much better ways to perform such an integration procedure. Over the years, very smart grids have been invented, constituted by special points of the Brillouin zone, chosen in such a way that the sum rapidly reaches the convergence on increasing  $N_{\mathbf{k}}$ . A very efficient grid is

---

<sup>7</sup> Actually, we here define the density of states for each state. It is normalized to the unity, when the integration on all the energy range is considered. The current definition differs in a multiplicative factor from the usual definition of density of states for unit volume.

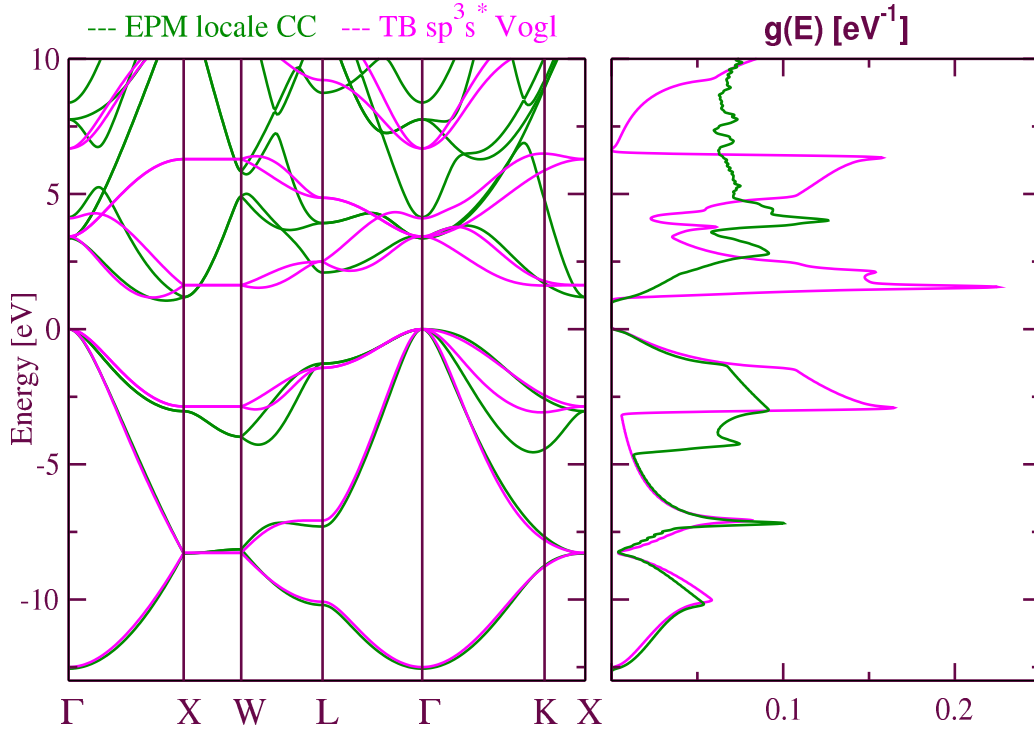


Figure 1.1: Bulk silicon band structure (left) and density of states (right) calculated with the Vogl  $sp^3s^*$  nearest neighbor model [18] (magenta lines), compared to a local empirical pseudopotential calculation (green lines), performed with the parameters of Ref. [12].

obtained with the Monkhorst and Pack scheme [19], that we have used together with the Born-von Karman grid to perform integrations over the first Brillouin zone.

In the recent years, computer performances have incredibly improved, allowing more complex fitting procedures than in the past. In this way, fitting of a band structure with many independent parameters is now possible, with the result of making TB band structures very close to *ab initio* results. Even if the first neighbor  $sp^3s^*$  TB is nowadays very used [20–25], because of its simplicity in considering only nearest neighbor interactions, better results are obtained using the minimal basis set  $sp^3$  and increasing the number of

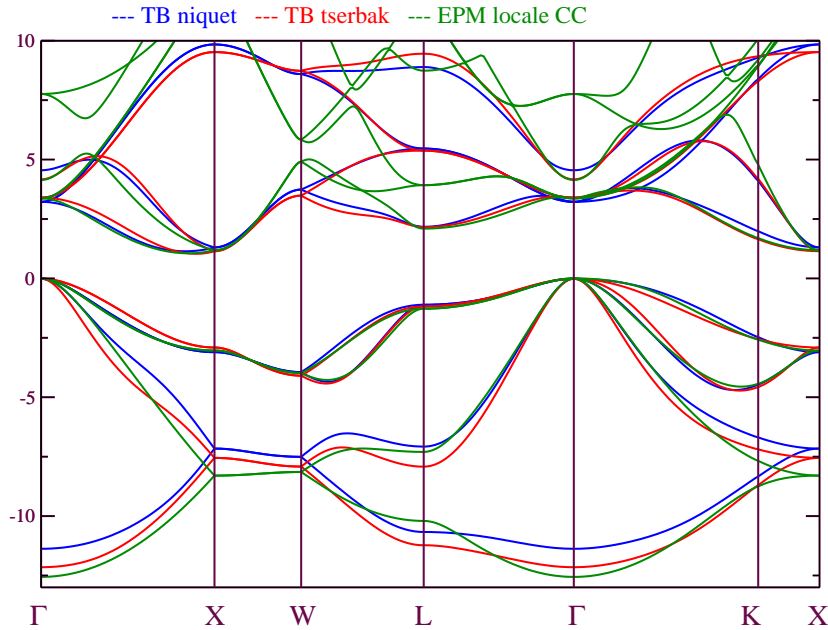


Figure 1.2: Bulk silicon band structure. Blue and red lines refer to, respectively, Niquet [28] and Tserbak [27] TB model; green lines come from a Pseudopotential calculation, with the Chelikowsky and Cohen parameters [12].

neighbors interacting with a single orbital.

The  $3^d$  nearest neighbor  $sp^3$  TB model is based on 20 independent parameters [26]. Tserbak *et al.* [27] found an optimum fit for these parameters, comparing the main band gaps computed with TB and pseudopotential method. Tserbak parameters lead to a band structure and a density of states that are indeed accurate over the whole first Brillouin Zone, not only at the lowest energies, in the valence band energy range, but also at the highest energies. In fact, the first conduction band agrees well to the pseudopotential curve over the most main symmetry lines. In figure (1.2) we report the bulk silicon band structure calculated with the pseudopotential method and the Tserbak model. We also show the band structure from the Niquet

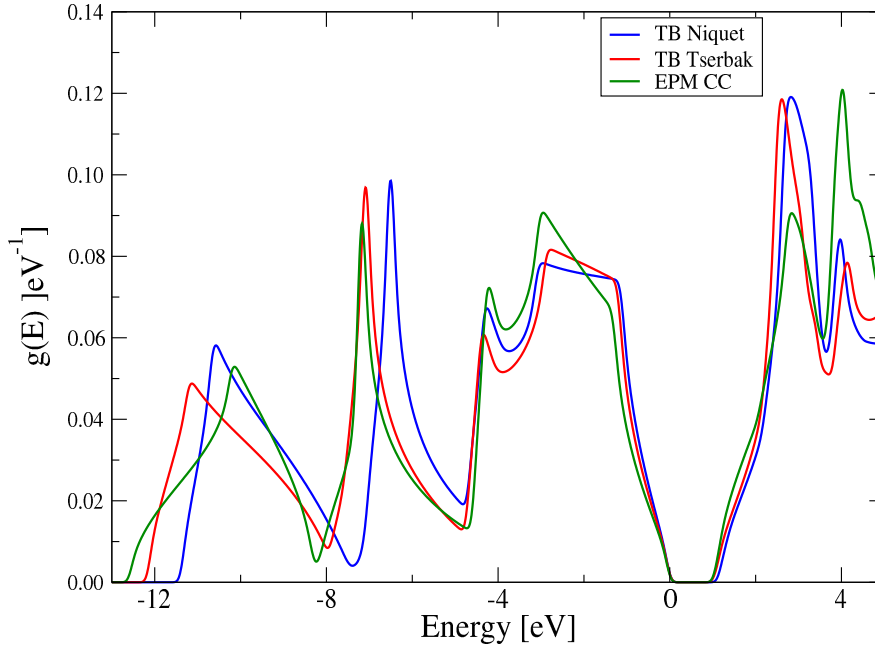


Figure 1.3: Bulk Silicon Density of States. Red and blue lines refer, respectively, to the Tserbak [27] and Niquet [28] TB parametrization; green line comes out from a pseudopotential calculation [12].

parametrizations, that we are going to discuss in the following.

The Tserbak model fails just on predicting very precisely the effective masses near the highest symmetry k-points. Especially when dealing with nanostructures, it is desirable that, in the limit of very large systems, the TB results merge with those coming from the Effective Mass Approximation (EMA) theory. For this reason, very precise values of the effective masses are required. Niquet *et al.* [28], starting from the Tserbak model, proposed a new set of parameters, obtained imposing the further condition that the main electron and hole calculated effective masses were equal to their experimental values. This new set of parameters leads to an overall less accurate band structure than that one of Tserbak, but they give good values of the hole and the electron effective masses. A comparison between the two parametriza-

Parameter	Tserbak	Niquet	Parameter	Tserbak	Niquet
$E_s$	-6.3193	-6.17334	$W_{xy}$	-0.0378	-0.05462
$E_p$	2.2494	2.39585	$W_{xz}$	0.0829	0.12754
$V_{ss}$	-1.8376	-1.78516	$W_{zz}$	-0.2646	-0.24379
$V_{sx}$	1.0087	0.78088	$U_{ss}$	-0.0674	-0.06857
$V_{xx}$	0.3209	0.35657	$U_{sx}$	0.2717	0.25209
$V_{xy}$	1.4889	1.47649	$U_{sy}$	-0.1262	-0.17098
$W_{ss}$	0.1940	0.23010	$U_{xx}$	0.0869	0.13968
$W_{sx}$	-0.1840	-0.21608	$U_{xy}$	0.0152	-0.03625
$W_{sz}$	-0.0395	-0.02496	$U_{yy}$	0.0094	-0.04580
$W_{xx}$	0.0626	0.02286	$U_{yz}$	0.0952	0.06921

Table 1.1: Interaction parameters in the  $3^{rd}$  nearest neighbor  $sp^3$  TB model, from Tserbak [27] and Niquet [28] parametrizations. All the parameters are in  $eV$ .

tions is in the DOS curves, that we report in figure (1.3).

In table (1.1) the two sets of parameters have been reported, while table (1.2) shows an accurate comparison between the various methods and the experimental data. It comes out from table (1.2) that the Tserbak parameters give energy values close to both the pseudopotential and the experimental band gaps, and indeed the DOS graph in figure (1.3) shows an overall agreement between the Tserbak's TB and the pseudopotential curves. The Niquet parameters, on the contrary, lose in precision at low energies. But they give a much better agreement in the neighborhood of the band gap, with a good prediction for the fundamental band gap and the conduction effective masses. Even for the hole effective masses the agreement with experiments is not too bad, when compared to the other theoretical calculations. For example, even

	Niquet	Tserbak	EPM CC	Experimental
$\Gamma_{2'}^c$	4.57	4.14	4.14	4.15
$\Gamma_{15}^c$	3.24	3.41	3.37	3.35
$\Gamma_{25'}^v$	0.0	0.0	0.0	0.0
$X_1^c$	1.32	1.16	1.19	1.13
$X_4^v$	-3.09	-2.89	3.03	-2.9
$L_1^c$	2.19	2.17	2.10	2.04
$L_{3'}^v$	-1.09	-1.19	-1.27	-1.2
$E_{gap}$	1.16	1.05	1.06	1.17
$m_l$	0.919	0.567	0.912	0.916
$m_t$	0.191	0.173	0.195	0.191
$m_{lh}[100]$	0.200	0.147	0.167	0.17
$m_{hh}[100]$	0.283	0.533	0.274	0.46
$m_{lh}[111]$	0.138	0.133	0.097	0.16
$m_{hh}[111]$	0.712	0.854	0.681	0.57

Table 1.2: Transition energies and effective masses from different methods.

a recent more sophisticated *DFT* calculation [29] gives only a value of 0.26 for the heavy hole along the (100) direction. A good discussion about the hole effective masses and the TB predictions, together with the  $\mathbf{k} \cdot \mathbf{p}$  parameters, can be found in Ref. [17]. The conclusions of the authors, who compare the Tserbak and Niquet  $sp^3$  models and the  $sp^3d^5s^*$  Jancu parametrization [10], is that, among all these schemes, the Niquet model gives the best hole effective masses, and the best  $\mathbf{k} \cdot \mathbf{p}$  parameters.



# Chapter 2

## Linear Response Theory

### 2.1 Introduction

In this chapter we are going to discuss the interaction of a crystalline structure with the electromagnetic field. First of all, we shall give a general definition of the dielectric tensor, in order to describe not only the cubic crystals (like bulk silicon), but also optical anisotropic media, with a lower-than-cubic symmetry. In the following section we shall state the problem, and underline the approximations at the basis of the calculation. Then we shall recover the constitutive relationships of a crystal, within a microscopic full quantum mechanical formulation. In the second part of this chapter, the extension of the TB interpolation scheme to the linear response theory is discussed. We will give the statement of the problem, with a brief overview of the methods that have been proposed over the years to solve it. Then we will focus on the approximation that we use, trying to show advantages and limits, in particular with the study of the longitudinal component of the dielectric function. Finally, we will show the calculated bulk silicon dielec-

tric properties, comparing the TB calculations to the EPM results and the experimental data.

## 2.2 Response of a crystal to an external field

When an electromagnetic wave travels through a dielectric non-magnetic medium, polarization effects induce currents and charges that interact with the external field. The macroscopic statement of the problem is based on the Maxwell equations inside the medium, that we write here for convenience, assuming that inside the medium there are neither external charges nor currents [30]:

$$\nabla \cdot \mathbf{D} = 0 \quad (2.1)$$

$$\nabla \cdot \mathbf{B} = 0 \quad (2.2)$$

$$\nabla \times \mathbf{E} = -\frac{1}{c} \frac{\partial \mathbf{B}}{\partial t} \quad (2.3)$$

$$\nabla \times \mathbf{B} = \frac{1}{c} \frac{\partial \mathbf{D}}{\partial t}. \quad (2.4)$$

Here,  $\mathbf{D}$  is the external electric field,  $\mathbf{B}$  is the magnetic field, while  $\mathbf{E}$  is the total electric field inside the medium. All the quantities considered here depend on the space and the time. We assume that all the fields are slowly varying in space with respect to the lattice constant of the structure. From the Maxwell equations, the following wave equation can be obtained:

$$\nabla^2 \mathbf{E} - \nabla(\nabla \cdot \mathbf{E}) - \frac{1}{c^2} \frac{\partial^2}{\partial t^2} \mathbf{D} = 0. \quad (2.5)$$

Starting from the constitutive equations of the medium, that define the response of the system to an external field, the dispersion relationships can be

obtained from the latter equation. For an anisotropic medium, the general relation that relates  $\mathbf{D}$  and  $\mathbf{E}$  can be written as<sup>1</sup>:

$$D_\alpha(\mathbf{r}t) = \int d\mathbf{r}_1 dt_1 \epsilon_{\alpha\beta}(\mathbf{r}, \mathbf{r}_1; t - t_1) E_\beta(\mathbf{r}_1, t_1). \quad (2.6)$$

Eq. (2.6) can be thought of as a definition of the dielectric tensor  $\epsilon$  in real space. Fourier-transforming Eq. (2.6), and using the crystal translational symmetry, we obtain the reciprocal space definition of the dielectric tensor [31]:

$$D_\alpha(\mathbf{q} + \mathbf{G}, \omega) = \sum_{\mathbf{G}'} \epsilon_{\alpha\beta}(\mathbf{q} + \mathbf{G}, \mathbf{q} + \mathbf{G}', \omega) E_\beta(\mathbf{q} + \mathbf{G}', \omega). \quad (2.7)$$

Here,  $\mathbf{G}$  and  $\mathbf{G}'$  are two crystal reciprocal space vectors, while  $\mathbf{q}$  belongs to the first Brillouin Zone. The  $\mathbf{G} \neq \mathbf{G}'$  components of the dielectric tensor give the so called local field effects (LFE). They take into account the fact that the effective perturbing field acting in a particular zone of the crystal, is not the bare external field but a local field which includes effects from all the charges within the medium, macroscopically far from that zone. In this real space formulation, neglecting the LFE is equal to assuming that the dielectric tensor depends only on the vector difference  $\mathbf{r} - \mathbf{r}'$ . LFE should be analyzed for each material, in that they could be of great importance. However, in the case of bulk silicon crystals, it has been shown that they do not significantly change the form of the dielectric function [32].

In the following, we shall use the so called Random Phase Approximation (RPA) for the dielectric tensor, treating the crystal as an homogeneous electron gas and neglecting the local field effects. In this approximation, we have:

$$D_\alpha(\mathbf{q}, \omega) = \epsilon_{\alpha\beta}(\mathbf{q}, \omega) E_\beta(\mathbf{q}, \omega). \quad (2.8)$$

---

<sup>1</sup> We assume here sum over the repeated indices.

Inserting this constitutive relations inside the wave equation (2.5), we obtain the system of equations:

$$\sum_{\beta} \left( q^2 \delta_{\alpha,\beta} - q_{\alpha} q_{\beta} - \frac{\omega^2}{c^2} \epsilon_{\alpha\beta}(\mathbf{q}, \omega) \right) E_{\beta} = 0, \quad (2.9)$$

which has non-trivial solutions when the determinant nullifies [30]:

$$\det \left| q^2 \delta_{\alpha,\beta} - q_{\alpha} q_{\beta} - \frac{\omega^2}{c^2} \epsilon_{\alpha\beta}(\mathbf{q}, \omega) \right| = 0. \quad (2.10)$$

This gives the so called Fresnel equation [30], whose solutions are the dispersion relationships for the crystal.

Defining  $\mathbf{e}$  and  $\mathbf{q}$  as, respectively, the polarization and the propagation versors of an electromagnetic wave traveling inside the medium, we find convenient to separate the longitudinal component of the field ( $\mathbf{E}^l \cdot \mathbf{e} = 0$ ) by the transverse component ( $\mathbf{E}^t \cdot \mathbf{q} = 0$ ). The dielectric tensor gives the most general information for the linear response of the system to an external field. In fact, starting from it, the longitudinal-longitudinal and the transverse-transverse dielectric components can be deduced from the equations:

$$\epsilon^{ll}(\mathbf{q}, \omega) = \hat{\mathbf{q}}_{\alpha} \epsilon_{\alpha\beta}(\mathbf{q}, \omega) \hat{\mathbf{q}}_{\beta} \quad (2.11)$$

$$\epsilon^{tt}(\mathbf{q}, \omega) = \hat{\mathbf{e}}_{\alpha} \epsilon_{\alpha\beta}(\mathbf{q}, \omega) \hat{\mathbf{e}}_{\beta}. \quad (2.12)$$

They represent the longitudinal (transverse) response to a longitudinal (transverse) external field. For non-cubic crystals, these two terms are not sufficient, and also the longitudinal-transverse and the transverse-longitudinal components have to be calculated, in order to study the response to a generic external field. In the cubic case, instead, the problem is fully separable into a longitudinal and a transverse part, and the dispersion relations  $\omega(\mathbf{q})$  can

be obtained from the Fresnel equations, which become:

$$\epsilon^{ll}(\mathbf{q}, \omega) = 0 \quad (2.13)$$

$$\omega^2 \epsilon^{tt}(\mathbf{q}, \omega) = q^2 c^2. \quad (2.14)$$

The first of this couple of equations gives the plasmon dispersion curve, the second one describes an external wave travelling inside the medium. We are mainly interested in the second equation, which gives the relations between the real and the imaginary part of the dielectric function and the optical properties of the medium (refraction index, extinction coefficient, reflection and transmission functions, absorption coefficient). In the limit  $\mathbf{q} \rightarrow 0$ , in the cubic case the two dielectric components are equal, and therefore the response of the system to both a longitudinal and a transverse external field is exactly the same.

The linear response problem consists in the calculation of the constitutive equations of a medium starting from a microscopic ground. The current induced by an external field, in reciprocal space, is related to the total electric field by means of the following relationships:

$$\delta J_\alpha(\mathbf{q}, \omega) = -\frac{i\omega}{4\pi} [\epsilon_{\alpha,\beta}(\mathbf{q}, \omega) - \delta_{\alpha,\beta}] E_\beta(\mathbf{q}, \omega). \quad (2.15)$$

Starting from this statement, in the next paragraphs we are going to derive a microscopic formulation of the dielectric tensor within the RPA.

## 2.3 Interaction picture and correlation functions

In the Schrödinger picture of quantum mechanics, the state of a system is represented by the vector of an Hilbert space, which explicitly depends on time. Using the Dirac notation, we write the state vectors and the operators in the Schrödinger picture as:

$$|\Psi_S(t)\rangle, \hat{O}_S. \quad (2.16)$$

The operators in the Schrödinger picture do not have an explicit time dependence, which is fully included into the state vectors through the Schrödinger equation

$$i\hbar\partial_t |\Psi_S(t)\rangle = \hat{H} |\Psi_S(t)\rangle, \quad (2.17)$$

which contains the Hamiltonian operator  $\hat{H}$ . Once that the initial conditions of the problem have been fixed (namely, the state vector at  $t_0$ ), the formal solution of Eq. (2.17) is

$$|\Psi_S(t)\rangle = e^{-i\hat{H}(t-t_0)/\hbar} |\Psi_S(t_0)\rangle. \quad (2.18)$$

In the linear response problems, a quantum system is subject to an external field, small enough to allow a perturbative approach. The Hamiltonian operator has the form:

$$\hat{H} = \hat{H}_0 + \hat{V}, \quad (2.19)$$

where  $\hat{H}_0$  is the unperturbed Hamiltonian of the isolated system, while the  $\hat{V}$  term is due to the external field action. In these situations an extremely

useful picture is the interaction picture, whose basic idea consists in splitting the time dependence between state vectors and operators. Using the unitary transformation:

$$|\Psi_I(t)\rangle = e^{i\hat{H}_0 t/\hbar} |\Psi_S(t)\rangle, \quad (2.20)$$

and the corresponding operator transformation:

$$\hat{O}_I(t) = e^{i\hat{H}_0 t/\hbar} \hat{O}_S e^{-i\hat{H}_0 t/\hbar}, \quad (2.21)$$

it is easy to verify that only the perturbation term contributes to the time dependence of the state vector, through the equation:

$$i\hbar\partial_t |\Psi_I(t)\rangle = \hat{V}_I(t) |\Psi_I(t)\rangle, \quad (2.22)$$

while  $\hat{H}_0$  gives the time dependence of the operators, through the motion equation:

$$i\hbar\partial_t \hat{O}_I(t) = [\hat{O}_I(t), \hat{H}_0]. \quad (2.23)$$

The formal explicit solution of Eq. (2.22) is<sup>2</sup>:

$$|\Psi_I(t)\rangle = \hat{T} \exp \left\{ -\frac{i}{\hbar} \int_{t_0}^t dt_1 V_I(t_1) \right\} |\Psi_I(t_0)\rangle, \quad (2.24)$$

which is an expression well suitable to a series expansion. We assume that the external potential is switched on at a finite instant of time  $\tau$ . Therefore, in the limit  $t_0 \rightarrow \infty$ , the starting state of the system is an eigenstate of  $\hat{H}_0$ . Let us label the unperturbed states with the notation  $|\Phi_m\rangle$ :

$$\hat{H}_0 |\Phi_m\rangle = E_m^0 |\Phi_m\rangle. \quad (2.25)$$

---

<sup>2</sup>  $\hat{T}$  is the Time-ordering operator, defined as:

$$\hat{T} [\hat{O}(t_1)\hat{B}(t_2)] \equiv \theta(t_1 - t_2)\hat{O}(t_1)\hat{B}(t_2) - \theta(t_2 - t_1)\hat{B}(t_2)\hat{O}(t_1),$$

$\theta$  is the Heaviside function.

We assume that the system is in its fundamental state  $|\Phi_0\rangle$  before the perturbation is switched on, and so we can put

$$|\Psi_I(-\infty)\rangle = |\Phi_0\rangle. \quad (2.26)$$

In this way, we can write the state vector at the first perturbative order, starting from the fundamental unperturbed state, as:

$$|\Psi_I(t)\rangle = \left(1 - \frac{i}{\hbar} \int_{-\infty}^t dt_1 V_I(t_1)\right) |\Phi_0\rangle. \quad (2.27)$$

The main quantities in the study of a physical quantum system are the expectation values of hermitian operators. These are picture-independent functions, and we shall see in the following the utility of using the interaction picture. Let us consider a physical variable  $O$ , represented by an hermitian operator  $\hat{O}$ . In the perturbed system, the expectation value of  $\hat{O}$  is

$$\langle \hat{O} \rangle (t) \equiv \langle \Psi_I(t) | \hat{O}_I(t) | \Psi_I(t) \rangle. \quad (2.28)$$

By substituting Eq. (2.27), we can calculate the linear response of  $O$  to an external field, and we find the result

$$\langle \hat{O} \rangle (t) = \langle \hat{O} \rangle_0 + \frac{i}{\hbar} \int_{-\infty}^t dt_1 \langle [\hat{V}_I(t_1), \hat{O}_I(t)] \rangle_0, \quad (2.29)$$

where the right side expectation values have been calculated on the unperturbed fundamental state:

$$\langle \hat{O} \rangle_0 \equiv \langle \Phi_0 | \hat{O} | \Phi_0 \rangle. \quad (2.30)$$

Therefore, we obtain the quite general formula of the variation of a physical quantity when the system is subject to the action of an external field:

$$\delta O(t) = \frac{i}{\hbar} \int_{-\infty}^{\infty} dt_1 \langle [\hat{V}_I(t_1), \hat{O}_I(t)] \rangle_0 \Theta(t_1 - t). \quad (2.31)$$

## 2.4 The dielectric tensor

In this section, we shall see in detail the linear response of an electron non-magnetic system subject to an external electromagnetic field. In order to study the dielectric tensor for a generic medium, we consider an external field, having both a longitudinal and a transverse component. We know that the optical properties of a crystal are gauge-independent [31], so we choose the gauge in which there is not any scalar potential. In this case the electric field is related to the only vector potential through the relationship:

$$\mathbf{E}(\mathbf{r}, t) = -\frac{1}{c} \frac{\partial \mathbf{A}}{\partial t}(\mathbf{r}, t). \quad (2.32)$$

or, in the conjugate space,

$$\mathbf{E}(\mathbf{q}, \omega) = \frac{i\omega}{c} \mathbf{A}(\mathbf{q}, \omega). \quad (2.33)$$

The microscopic current density operator  $\hat{\mathbf{J}}(\mathbf{r})$ , for a many body system in an electromagnetic field, is defined as the sum of two terms [33]:

$$\hat{\mathbf{J}}(\mathbf{r}) = \hat{\mathbf{J}}_1(\mathbf{r}) + \hat{\mathbf{J}}_2(\mathbf{r}), \quad (2.34)$$

where

$$\left\{ \begin{array}{l} \hat{\mathbf{J}}_1(\mathbf{r}) = -\frac{e^2}{mc} \sum_{i=1}^N \mathbf{A}(\mathbf{r}_i, t) \delta(\mathbf{r} - \mathbf{r}_i) \\ \hat{\mathbf{J}}_2(\mathbf{r}) = -\frac{e}{2m} \sum_{i=1}^N [\hat{\mathbf{p}}_i \delta(\mathbf{r} - \mathbf{r}_i) + \delta(\mathbf{r} - \mathbf{r}_i) \hat{\mathbf{p}}_i]. \end{array} \right. \quad (2.35)$$

$N$  is the total number of electrons inside the crystal. When considering the interaction with an external field, among the two components, only the second term in Eq. (2.35), which we called  $\hat{\mathbf{J}}_2(\mathbf{r})$ , gives a linear contribution

to the energy. We can write the potential energy operator as<sup>3</sup>:

$$\hat{V}(t) = \frac{1}{c} \int d\mathbf{r} \hat{\mathbf{J}}_2(\mathbf{r}, t) \cdot \mathbf{A}(\mathbf{r}, t). \quad (2.36)$$

The current density linear response is the sum of the variations of its two components. Using Eq.(2.31), we can write the induced current as:

$$\delta J_\alpha(\mathbf{r}, t) = -\frac{e^2 N}{mc\Omega} A_\alpha(\mathbf{r}, t) + \frac{1}{\hbar c} \int d\mathbf{r}_1 dt_1 \Pi_{\alpha,\beta}^R(\mathbf{r}t; \mathbf{r}_1 t_1) A_\beta(\mathbf{r}_1, t_1), \quad (2.37)$$

where the first term comes out from the  $\hat{\mathbf{J}}_1$  contribution ( $\Omega$  is the structure volume), while the second term comes out from  $\hat{\mathbf{J}}_2$ . We have introduced the retarded current-current correlation tensor

$$\Pi_{\alpha,\beta}^R(\mathbf{r}t; \mathbf{r}'t') \equiv -i \langle [J_{2\alpha}(\mathbf{r}t), J_{2\beta}(\mathbf{r}'t')] \rangle_0 \Theta(t - t'). \quad (2.38)$$

Using the well known Lehmann representation [34], by inserting a complete set of unperturbed many-body eigenstates, we obtain the Fourier transform of Eq. (2.38). In the following we neglect the local field effects, assuming a local response in  $\mathbf{q}$ -space, and we come to the result:

$$\Pi_{\alpha,\beta}^R(\mathbf{q}; \omega) = \sum_m \left[ \frac{J_{2\alpha}(\mathbf{q})_{0m} J_{2\beta}(-\mathbf{q})_{m0}}{\omega - \omega_m + i\eta} - \frac{J_{2\beta}(\mathbf{q})_{0m} J_{2\alpha}(-\mathbf{q})_{m0}}{\omega + \omega_m + i\eta} \right]. \quad (2.39)$$

We have defined the Fourier-transformed current operator  $\hat{\mathbf{J}}_2(\mathbf{q})$ :

$$\hat{J}_{2\alpha}(\mathbf{q}) = -\frac{e}{2m} \sum_{i=1}^N [\hat{\mathbf{p}}_i e^{-\mathbf{q}\cdot\mathbf{r}_i} + e^{-\mathbf{q}\cdot\mathbf{r}_i} \hat{\mathbf{p}}_i]. \quad (2.40)$$

The current density matrix elements between a couple of unperturbed many-body states, whose transition frequency is  $\omega_m = (E_m - E_0)/\hbar$ , are:

$$J_{2\alpha}(\mathbf{q})_{0m} \equiv \langle \Phi_0 | \hat{J}_{2\alpha}(\mathbf{q}) | \Phi_m \rangle. \quad (2.41)$$

---

<sup>3</sup> Here and in the following expressions, all the time-dependent operators are taken in the interaction picture.

We consider here the one-electron approximation, in which the unperturbed states are Slater determinants of single particle functions, and the induced current versus the electric field relationship becomes <sup>4</sup>:

$$\delta J_\alpha(\mathbf{q}, \omega) = \frac{ie^2 N}{m\Omega\omega} E_\alpha(\mathbf{q}, \omega) - \frac{i}{\Omega\omega} \sum_{n,n'} (f_{n'} - f_n) \left[ \frac{j_{2\alpha}(\mathbf{q})_{nn'} j_{2\beta}(-\mathbf{q})_{n'n}}{\hbar\omega - E_{nn'} + i\eta} \right] E_\beta(\mathbf{q}, \omega). \quad (2.42)$$

We have introduced the single particle current density matrix elements:

$$j_{2\alpha}(\mathbf{q})_{nn'} \equiv -\frac{e}{2m} \langle \phi_n | \hat{p}_\alpha e^{-i\mathbf{q}\cdot\mathbf{r}} + e^{-i\mathbf{q}\cdot\mathbf{r}} \hat{p}_\alpha | \phi_{n'} \rangle, \quad (2.43)$$

where  $|\phi_n\rangle$  is an unperturbed single particle state. We define  $f_n$  as the occupation of the  $n^{\text{th}}$  unperturbed single particle level. At zero temperature, for a semiconductor in its ground state, we know that  $f_n = 1$  for all the occupied, valence states, while  $f_n = 0$  for the conduction states. In this single particle picture,  $E_n$  is the single particle unperturbed energy, and we have taken  $E_{nn'} \equiv E_{n'} - E_n$ . Thus the final form for the dielectric tensor in the RPA is [31]:

$$\epsilon_{\alpha,\beta}(\mathbf{q}, \omega) = \left(1 - \frac{4\pi e^2 N}{m\Omega\omega^2}\right) \delta_{\alpha,\beta} + \frac{4\pi}{\Omega\omega^2} \sum_{n,n'} (f_{n'} - f_n) \left[ \frac{j_{2\alpha}(\mathbf{q})_{nn'} j_{2\beta}(-\mathbf{q})_{n'n}}{\hbar\omega - E_{nn'} + i\eta} \right]. \quad (2.44)$$

From this equation we can easily find the longitudinal-longitudinal component of the dielectric tensor, that is a basic quantity needed for the study of the crystal screening properties, and the transverse-transverse component, related to the optical properties of the crystal. The longitudinal-longitudinal component can be written in terms of the matrix elements of the charge

---

<sup>4</sup> We use  $E_\alpha$  as the  $\alpha$  component of the external electric field  $\mathbf{E}$ .

density operator, that we define as

$$\rho(\mathbf{q}) = -e e^{-i\mathbf{q}\cdot\mathbf{r}}. \quad (2.45)$$

The charge conservation equation is the link between a linear response based respectively on a current density or on a charge density formulation, as we shall see later. It is not difficult to verify the following generalized sum rule:

$$\sum_{n,n'} (f_{n'} - f_n) \frac{|\mathbf{q} \cdot \mathbf{j}_2(\mathbf{q})_{nn'}|^2}{E_{nn'}} = -e^2 \sum_n f_n = -N e^2, \quad (2.46)$$

that leads us to write down the longitudinal-longitudinal dielectric function in the following way:

$$\epsilon^{ll}(\mathbf{q}, \omega) = 1 + \frac{4\pi\hbar^2}{\Omega} \left( \frac{E + i\eta}{E} \right)^2 \sum_{n,n'} \frac{(f_{n'} - f_n)}{E_{nn'}^2} \left[ \frac{j_{2\alpha}(\mathbf{q})_{nn'} j_{2\beta}(-\mathbf{q})_{n'n}}{\hbar\omega - E_{nn'} + i\eta} \right]. \quad (2.47)$$

In the limit of negligible broadening  $\eta$ , this latter equation can be well approximated by the following one, that is a fundamental result of the linear response theory:

$$\epsilon^{ll}(\mathbf{q}, \omega) = 1 + \frac{4\pi\hbar^2}{\Omega} \sum_{n,n'} \frac{(f_{n'} - f_n)}{E_{nn'}^2} \left[ \frac{j_{2\alpha}(\mathbf{q})_{nn'} j_{2\beta}(-\mathbf{q})_{n'n}}{\hbar\omega - E_{nn'} + i\eta} \right]. \quad (2.48)$$

The longitudinal-longitudinal component could also be obtained starting from the Coulomb Gauge ( $\mathbf{q} \cdot \mathbf{A} = 0$ ), and working only in terms of the scalar potential. In this case, by studying the charge density response, and introducing a density-density correlation function, a different relationship is obtained for the longitudinal-longitudinal dielectric function. These two different formulations give identical results, because they only differ in a choice of gauge, and the dielectric tensor is a gauge-invariant quantity. The way for

getting one formulation from the other is the charge conservation equation. We write here such equation in the single particle operator form, connecting the longitudinal component of the current density to the commutator between the Hamiltonian ( $\hat{h}$  is the one-electron Hamiltonian) and the charge density:

$$\hbar \mathbf{q} \cdot \hat{\mathbf{j}}_2(\mathbf{q}) = [\hat{\rho}(\mathbf{q}), \hat{h}] = i \frac{\partial}{\partial t} \hat{\rho}(\mathbf{q}). \quad (2.49)$$

Using the expression (2.48) obtained before, together with the charge conservation equation (2.49), we find the longitudinal-longitudinal dielectric function that is obtained within a charge density response formulation:

$$\epsilon^{ll}(\mathbf{q}, \omega) = \delta_{\alpha, \beta} + \frac{4\pi e^2}{q^2 \Omega} \sum_{n, n'} (f_{n'} - f_n) \left[ \frac{|\langle \phi_n | e^{-i\mathbf{q} \cdot \mathbf{r}} | \phi_{n'} \rangle|^2}{\hbar \omega - E_{nn'} + i\eta} \right]. \quad (2.50)$$

Coming back to Eq. (2.44), it is useful to derive the limit of very long wavelengths, when  $\mathbf{q} \rightarrow 0$ , and we obtain the dielectric tensor<sup>5</sup>:

$$\epsilon_{\alpha, \beta}(\omega) = \delta_{\alpha, \beta} + \frac{4\pi e^2 \hbar^2}{\Omega m^2} \sum_{n, n'} \frac{(f_{n'} - f_n)}{E_{nn'}^2} \left[ \frac{\langle n | \hat{p}_\alpha | n' \rangle \langle n' | \hat{p}_\beta | n \rangle}{\hbar \omega - E_{nn'} + i\eta} \right]. \quad (2.51)$$

In the case of a cubic crystal, such as bulk silicon, the  $\mathbf{q} \rightarrow \mathbf{0}$  dielectric tensor reduces to the unit tensor times a scalar quantity, that is usually defined as the dielectric function<sup>6</sup>:

$$\epsilon(\omega) = 1 + \frac{4\pi e^2 \hbar^2}{3\Omega m^2} \sum_{n, n'} \frac{(f_{n'} - f_n)}{E_{nn'}^2} \frac{|\langle n | \mathbf{p} | n' \rangle|^2}{[\hbar \omega - E_{nn'} + i\eta]}. \quad (2.52)$$

---

<sup>5</sup> In order to obtain this equation, we have used a procedure similar to that shown before for the longitudinal component of the dielectric function.

<sup>6</sup> We use the following short notation for the square modulus of complex vector quantities:

$$|\mathbf{A}|^2 \equiv \sum_{\alpha=1}^3 |A_\alpha|^2.$$

As we have already pointed out, for cubic crystals, in the limit of long wavelengths, both the longitudinal and the transverse components of the dielectric tensor give the same dielectric function defined in the fundamental equation (2.52).

In the case of a bulk crystal, we explicitly write down the  $\mathbf{k}$ -dependent expressions. The longitudinal dielectric response, taking into account the spin degeneracy through a 2 factor, is:

$$\epsilon^l(\mathbf{q}, \omega) = \delta_{\alpha, \beta} + \frac{8\pi e^2}{q^2 \Omega} \sum_{n, n', \mathbf{k}} [f_{n'}(\mathbf{k} + \mathbf{q}) - f_n(\mathbf{k})] \left[ \frac{|\langle n\mathbf{k} | e^{-i\mathbf{q}\cdot\mathbf{r}} | n'\mathbf{k} + \mathbf{q} \rangle|^2}{\hbar\omega - E_{n'}(\mathbf{k} + \mathbf{q}) + E_n(\mathbf{k}) + i\eta} \right], \quad (2.53)$$

while the dielectric function is (limit of long wavelengths):

$$\epsilon(\omega) = 1 + \frac{8\pi e^2 \hbar^2}{3\Omega m^2} \sum_{n, n', \mathbf{k}} \frac{[f_{n'}(\mathbf{k}) - f_n(\mathbf{k})] |\langle n\mathbf{k} | \mathbf{p} | n'\mathbf{k} \rangle|^2}{E_{nn'}(\mathbf{k})^2 [\hbar\omega - E_{nn'}(\mathbf{k}) + i\eta]}. \quad (2.54)$$

It is useful introducing, for each allowed transition, the Oscillator Strength (OS), defined as:

$$F_{nn'}(\mathbf{k}) = \frac{2 |\langle n\mathbf{k} | \mathbf{p} | n'\mathbf{k} \rangle|^2}{3mE_{nn'}(\mathbf{k})}. \quad (2.55)$$

In terms of the OS, we can write the dielectric function in the form:

$$\epsilon(E) = 1 + \frac{4\pi e^2 \hbar^2}{\Omega m} \sum_{n, n', \mathbf{k}} \frac{[f_{n'}(\mathbf{k}) - f_n(\mathbf{k})] F_{nn'}(\mathbf{k})}{E_{nn'}(\mathbf{k}) [E - E_{nn'}(\mathbf{k}) + i\eta]}. \quad (2.56)$$

## 2.5 Linear response and TB

The Tight Binding method, used as an empirical interpolation scheme, has been a simple and powerful calculation tool for many years. In the form it was first stated in the classical paper of Slater and Koster [1], the method has been used to compute no more than crystalline band structures. Many authors have been trying to enlarge the model in order to make it more

flexible. Indeed, the great simplicity of the SK approach, consisting in only including into the scheme a (more or less) small number of Hamiltonian parameters, becomes an annoying limit when one asks something more than a simple one-electron energy level calculation! The problem is the lacking of an explicit knowledge of the basis wave functions, so that calculations of important quantities, such as, for example, charge densities, oscillator strengths and dielectric properties, Coulomb and exchange interaction terms, are forbidden within this primitive scheme.

Over the years, many methods have been proposed, with the hope of approximating the TB atomic orbitals, or, at least, the momentum matrix elements, without rejecting the simple and powerful empirical way. A typical approach consists in performing an explicit calculation of the orthogonal basis functions, by using, for instance, a Löwdin transformation of a basis set of Gaussian or Slater orbitals, and choosing between a Slater-Koster or a Pseudopotential Hamiltonian [25,35–39]. These approaches represent the attempts of preserving the simplicity of the Empirical Tight Binding avoiding the complications of an *ab initio* scheme, which requires a greater number of basis orbitals [40], or the cumbersome study of localized functions [41,42], and the explicit construction of the Hamiltonian matrix.

A different method, much simpler, consists in directly fitting the momentum matrix elements, parametrized in such a way to reproduce oscillator strengths, dielectric function, or  $\mathbf{k}\cdot\mathbf{p}$  coefficients [22,43]. A recent usage, that we shall analyze in detail in the following, starts from writing the momentum

operator using the relationship<sup>7</sup>:

$$\hat{\mathbf{p}} = \frac{im}{\hbar} \left[ \hat{H}, \hat{\mathbf{r}} \right], \quad (2.57)$$

therefore changing the problem into the search of a suitable approximation for the position matrix elements. The difference of this approach with respect to the direct parametrization of the momentum matrix elements consists in the inclusion of the Hamiltonian parameters into the Eq.(2.57). In other words, we define the momentum using the informations on the Hamiltonian coming out from the fitting of the band structure. This is a crucial point, because the risk of each of the above mentioned methods is the setting of momentum parameters disconnected from the Hamiltonian parametrization. In fact, the use of the SK scheme for the energy levels calculations, together with a new *completely arbitrary* parametrization for the momentum operator (or even for the wave functions or the position operator) for the dielectric response calculations can lead to problems of self-consistency with the theory, such as, for example, the breaking of the gauge invariance of the dielectric tensor, or the breaking of the charge conservation [44, 45]. A good setting of the problem, from this point of view, was the one proposed by Hanke [36], who used Gaussian functions for simulating atomic orbitals, choosing the Gaussian coefficients in such a way to satisfy the charge conservation equation, and this guaranteed the equality between charge density and current density linear response. This is a good self-consistency check which each method should comply to. Later, we shall come back on this point, showing how much density and current response can change when charge conservation is not verified.

---

<sup>7</sup> From now on, we shall only consider single particle operators.

## 2.6 The approximation

Between the many proposed approximations, we have used a very simple one, that nevertheless allows us to get a good estimation of the bulk silicon dielectric function. Although the method has been proposed some time ago [27, 46], it has raised a new interest in recent years, with several researchers that have been trying to give it a more formal justification [45, 47–49].

The starting point consists in writing the position operator as the sum of two contributions [48]:

$$\hat{\mathbf{r}} = \hat{\mathbf{r}}_c + \hat{\mathbf{r}}_{inter}. \quad (2.58)$$

that we define through their matrix elements in the TB basis set<sup>8</sup>:

$$\langle \sigma \boldsymbol{\mu} \mathbf{R} | \hat{\mathbf{r}}_c | \sigma' \boldsymbol{\mu}' \mathbf{R}' \rangle = \mathbf{R}_\mu \delta_{\sigma\sigma'} \delta_{\boldsymbol{\mu}\boldsymbol{\mu}'} \delta_{\mathbf{R}\mathbf{R}'} \quad (2.59)$$

$$\langle \sigma \boldsymbol{\mu} \mathbf{R} | \hat{\mathbf{r}}_{inter} | \sigma' \boldsymbol{\mu}' \mathbf{R}' \rangle = \mathbf{D}_{\sigma\sigma'}^{\boldsymbol{\mu}\boldsymbol{\mu}'} (\mathbf{R}'_{\boldsymbol{\mu}'} - \mathbf{R}_\mu). \quad (2.60)$$

The first term  $\hat{\mathbf{r}}_c$  contains the diagonal part of the position operator in the basis set. The atomic orbitals are its eigenstates, with eigenvalues given by the atomic positions. The second term, instead, takes into account the off-diagonal contributions. The  $\mathbf{D}$  vector matrix, defined in Eq. (2.60), rapidly goes to zero on increasing the distance between the atoms. Its most important contribution comes from the on-site terms  $\mathbf{D}_{\sigma\sigma'}^{\boldsymbol{\mu}\boldsymbol{\mu}'}(\mathbf{0})$ . For the  $sp^3$  bulk silicon basis set, there is only one independent off-diagonal on-site parameter:

$$(D^{(x)})_{sx}^{\mathbf{0}\mathbf{0}}(\mathbf{0}). \quad (2.61)$$

Therefore, we can divide all the position matrix elements into three different contributions: (1) on-site, diagonal terms; (2) on-site, off-diagonal terms; (3)

---

<sup>8</sup> We follow the formalism introduced in chapter (1) for TB atomic orbitals, using the labelling  $\mathbf{R}_\mu = \mathbf{R} + \boldsymbol{\mu}$ .

off-site, off-diagonal terms.

The approximation that we use consists in retaining only the first contribution, and consequently treating the atomic orbitals as eigenstates of the position operator in the dielectric properties calculations:

$$\hat{\mathbf{r}} \approx \hat{\mathbf{r}}_e. \quad (2.62)$$

In this approximation, the third contribution with off-site terms, is supposed to be of little importance, the main part of the position operator coming from the on-site terms. There is an open discussion on whether or not including the contribution (2) of on-site, off-diagonal terms [24, 48–50]. From one point of view, this is important in order to retrieve a non-null isolated-atom dipole matrix element in the limit of very large lattice constant [24, 50]. From another point of view, it has been shown that the inclusion of this term could lead to troubles of consistency with the gauge-invariance of the theory [48, 49]. In the case of an  $sp^3$  third neighbor basis set, we have verified that including the additional term (2.61) only slightly modifies the bulk silicon dielectric function (an almost rigid shift in the intensities is observed, while the peaks positions are unchanged). For these reasons we have chosen to neglect such contribution.

Starting from the approximation in Eq. (2.62) for the position, we define the momentum matrix elements in the TB basis set via Eq. (2.57) :

$$\langle \sigma \boldsymbol{\mu} \mathbf{R} | \hat{\mathbf{p}} | \sigma' \boldsymbol{\mu}' \mathbf{R}' \rangle = \frac{im}{\hbar} (\mathbf{R}'_{\boldsymbol{\mu}'} - \mathbf{R}_{\boldsymbol{\mu}}) \langle \sigma \boldsymbol{\mu} \mathbf{R} | \hat{H} | \sigma' \boldsymbol{\mu}' \mathbf{R}' \rangle. \quad (2.63)$$

We want to point out that the present approximation, performed on the position operator, allows us to include into the momentum all the informations coming from the Hamiltonian parametrization, resulting into a momentum

operator with many off-diagonal terms. We expect that this approach is formally more correct than a direct parametrization of the momentum matrix elements.

Within this on-site diagonal approximation for the position operator,  $\hat{\mathbf{p}}$  assumes a very simple  $k$ -space representation, being proportional to the gradient of the Hamiltonian matrix:

$$\langle \sigma \boldsymbol{\mu} \mathbf{k} | \hat{\mathbf{p}} | \sigma' \boldsymbol{\mu}' \mathbf{k} \rangle = \frac{m}{\hbar} \nabla_{\mathbf{k}} H_{\sigma\sigma'}^{\boldsymbol{\mu}\boldsymbol{\mu}'}(\mathbf{k}). \quad (2.64)$$

## 2.7 The charge conservation

We have seen in a previous section that the charge conservation condition can be written as<sup>9</sup>:

$$\left[ \hat{\rho}(\mathbf{q}), \hat{H} \right] = \hbar \mathbf{q} \cdot \hat{\mathbf{j}}_2(\mathbf{q}). \quad (2.65)$$

Because of the translational symmetry of the Bravais lattices, for a bulk crystal the operator equation (2.65) has the following matrix elements between couple of Bloch states:

$$\left\langle n\mathbf{k} \left| \hbar \mathbf{q} \cdot \hat{\mathbf{j}}(\mathbf{q}) \right| n'\mathbf{k} + \mathbf{q} \right\rangle = \langle n\mathbf{k} | \hat{\rho}(\mathbf{q}) | n'\mathbf{k} + \mathbf{q} \rangle [E_{n'}(\mathbf{k} + \mathbf{q}) - E_n(\mathbf{k})]. \quad (2.66)$$

Starting from the well known Baker-Hausdorff formula

$$e^{\hat{A}} \hat{B} e^{-\hat{A}} = \hat{1} + [\hat{A}, \hat{B}] + \frac{1}{2!} [\hat{A}, [\hat{A}, \hat{B}]] + \frac{1}{3!} [\hat{A}, [\hat{A}, [\hat{A}, \hat{B}]]] \dots, \quad (2.67)$$

it is easily verified that the charge conservation is equivalent to imposing two conditions on the commutators between  $\hat{\mathbf{r}}$  and  $\hat{H}$ :

$$\left[ \hat{r}_{\alpha}, \hat{H} \right] = \frac{i\hbar}{m} \hat{p}_{\alpha} \quad (2.68)$$

$$[\hat{r}_{\alpha}, \hat{p}_{\beta}] = i\hbar \delta_{\alpha,\beta}. \quad (2.69)$$

---

<sup>9</sup> We have written here again the charge conservation Eq. (2.49), with the definition of charge density and current density given in Eqs. (2.45) and (2.40).

In the limit of long wavelengths ( $\mathbf{q} \rightarrow \mathbf{0}$ ), only the first one of this couple of equations is needed to verify Eq. (2.65).

Within the approach presented here, we approximate the position  $\hat{\mathbf{r}}$  with  $\hat{\mathbf{r}}_c$ , whose eigenstates are exactly the TB atomic orbitals, and then we *define* the momentum operator from Eq. (2.57). Therefore, by construction our model verifies the charge conservation equation in the limit  $\mathbf{q} \rightarrow \mathbf{0}$ , and so it is fully self-consistent in calculations of the long wavelength dielectric tensor in Eq. (2.51). Instead, it does not verify the canonical commutator relations in Eq. (2.69) between position and momentum operators. This means that, for finite values of  $\mathbf{q}$ , the charge conservation is not verified and we expect a density response different from the current response.

In order to give a quantitative estimation of their relative shift, we have analyzed both the current- and the density-derived longitudinal dielectric function, with the help of Eq. (2.48) and (2.50), in the static limit  $\omega = 0$ . In figure (2.1) we show the longitudinal dielectric function that we have computed using TB and EPM methods, in current and density representation. It is clear that there is a unique EPM curve, because within the Local Pseudopotential method the charge conservation is well defined, and both the density and current responses give the same result. On the contrary, our TB approach is charge-conserving only in the limit of long wavelengths, explaining why we retrieve a unique static dielectric constant ( $\mathbf{q} = \mathbf{0}$ ). On the other side, as Fig (2.1) clearly shows, the results are quite different on increasing values of the transferred momentum. From a comparison between the TB and EPM curves, it can be noticed that the TB current-derived dielectric function is very close to the pseudopotential curve. Quite surprisingly, the

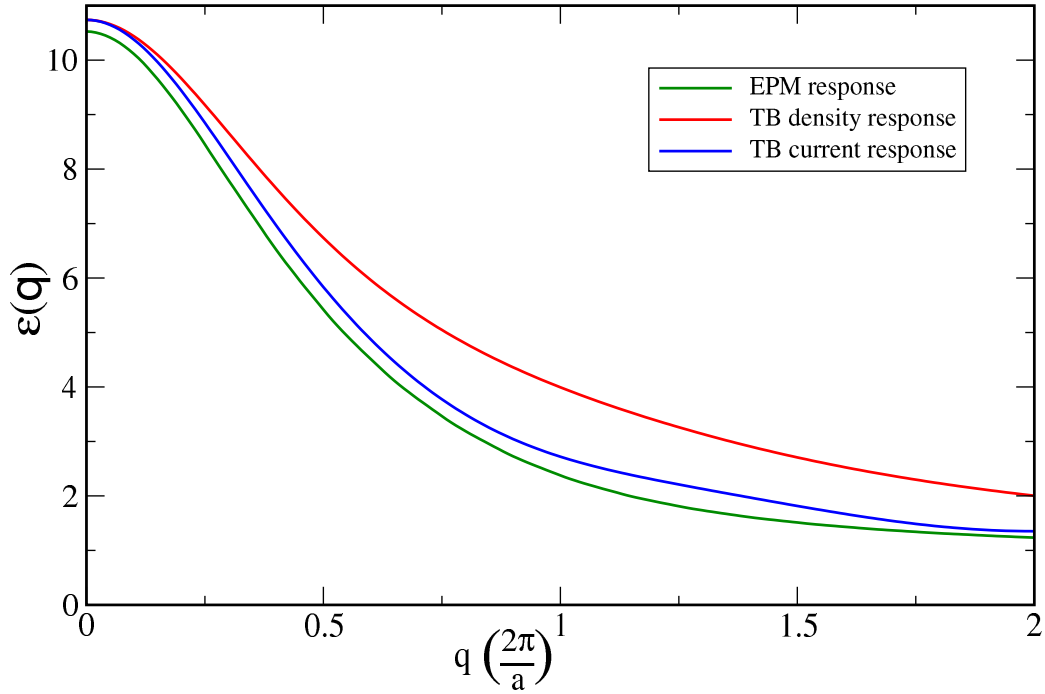


Figure 2.1: Longitudinal dielectric function along the (100) direction, calculated within both the density and current response approaches. We have used the Niquet parametrization [28] for TB and the Chelikowsky Local form factors [12] for EPM calculations. The green line refers to the EPM result, the blue and the red lines are, respectively, the TB current and density responses.

difference between the two curves is almost a simple vertical shift. Instead, the density response overestimates the EPM result. Somehow, this means that for finite values of  $\mathbf{q}$  the method gives a better estimation of current than density operator.

## 2.8 Results

In this section we are going to show the bulk silicon dielectric function, calculated using the so far described approximation, compared to EPM results and experimental data. We write here again the complex dielectric function for a bulk structure:

$$\epsilon(E) = 1 + \frac{4\pi e^2 \hbar^2}{\Omega m} \sum_{n,n',\mathbf{k}} \frac{[f_{n'}(\mathbf{k}) - f_n(\mathbf{k})] F_{nn'}(\mathbf{k})}{E_{nn'}(\mathbf{k}) [E - E_{nn'}(\mathbf{k}) + i\eta]}. \quad (2.70)$$

where we have used the oscillator strengths defined in Eq.(2.55). In particular, the imaginary part of the dielectric function can be written in the general form:

$$\epsilon_2(E) = \frac{4\pi^2 e^2 \hbar^2}{\Omega m} \sum_{n,n',\mathbf{k}} \frac{[f_{n'}(\mathbf{k}) - f_n(\mathbf{k})] F_{nn'}(\mathbf{k})}{E_{nn'}(\mathbf{k})} S(E - E_{nn'}(\mathbf{k})), \quad (2.71)$$

where  $S(x)$  is a broadening function, which is not necessarily a Lorentzian function, depending on the sort of broadening that the electronic levels feel. We here consider a Lorentzian broadening, and define  $S(x)$  as:

$$S(x) = \frac{\eta/\pi}{x^2 + \eta^2}. \quad (2.72)$$

Starting from the commutation relations in Eq. (2.69), it is simple to show that the following sum rule for the oscillator strengths holds:

$$\sum_{n'} F_{nn'}(\mathbf{k}) = 1. \quad (2.73)$$

Unfortunately, the present approximation does not verify Eq. (2.69), and so the sum rule neither. The calculation of the right hand of Eq.(2.73) is a good quantitative check on whether or not the oscillator strengths are well reproduced within our method. The sum rule (2.73) can be written as an

overall condition on the dielectric function imaginary part ( $N$  is the number of electrons contained inside the volume  $\Omega$ )<sup>10</sup>:

$$\frac{m\Omega}{2N\pi^2e^2\hbar^2} \int_0^\infty E\epsilon_2(E)dE = 1. \quad (2.74)$$

In the case of the bulk silicon, we obtain for the left side of this equation the value of 1.077, with both sets of TB parameters (Niquet and Tserbak parameters), showing that the sum rule is satisfied to within 8%.

In figure (2.2) we report the imaginary part of the bulk silicon dielectric function, calculated with EPM and TB. The experimental data are shown for comparison. Only no-phonon transitions are considered in the calculation. Phonon assisted transitions are expected to give a negligible contribution to  $\epsilon_2$ . Indeed, the measured dielectric function does not show any significant contributions at energies near the bulk Si indirect gap (at about 1.1 eV), which are dipole-forbidden. The analysis of the experimental  $\epsilon_2(E)$  shows two main peaks, that lie at energies of about 3.5 eV and 4.2 eV. Using both empirical [36] and *ab initio* models [32], it is nowadays clear that the first peak is due to excitonic effects, and can be theoretically calculated by only inserting the electron-hole interaction inside the dielectric function. This is not a simple task, and is well beyond the RPA approximation we are using. Within RPA, we are only able to predict a shoulder in correspondence of the first peak. Moreover, all the transition energies are slightly overestimated, because the excitonic effects make the one-electron energy levels closer. Keeping in mind these intrinsic limitations of RPA, we think, looking at figure (2.2), that there is a good agreement between the two TB parametrizations, EPM and experiments. Within the RPA, the solution we have chosen for

---

<sup>10</sup> The real and imaginary part of dielectric function are indicated with  $\epsilon_1$  and  $\epsilon_2$  respectively.

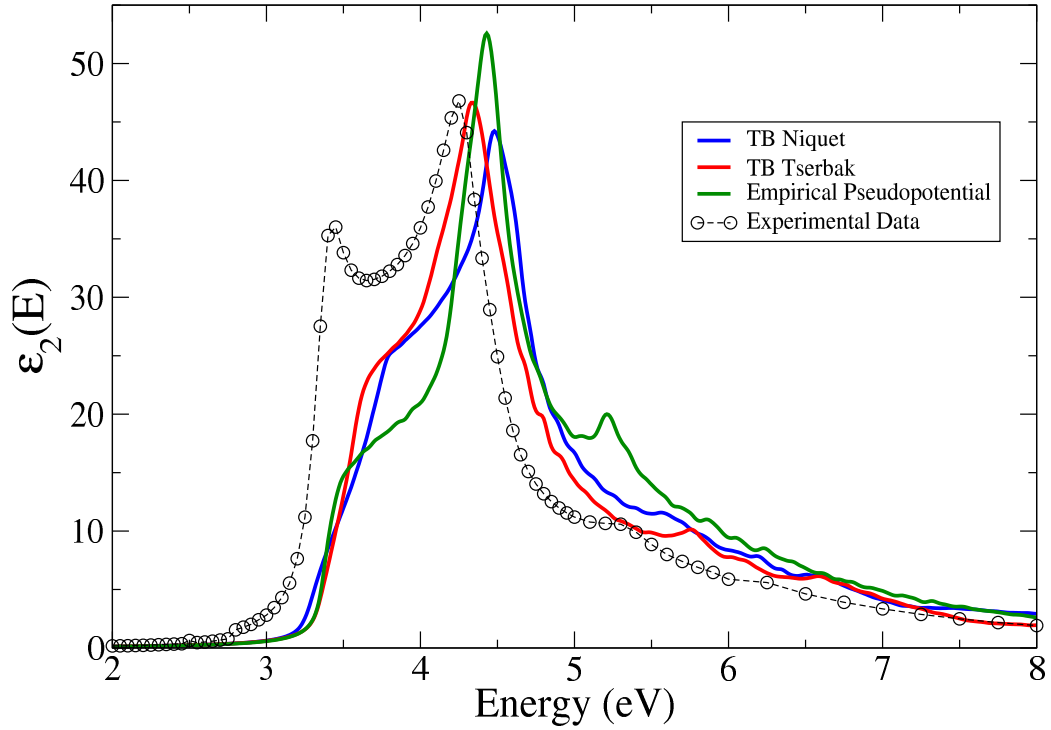


Figure 2.2: Imaginary part of the bulk silicon dielectric function. The empty circles are experimental data [51], the red and the blue lines are the Tight Binding curves calculated using, respectively, Tserbak [27] and Niquet [28] parameters, the green line refers to a Local Empirical Pseudopotential calculation performed with the Chelikowsky-Cohen parameters [12]. A Lorentzian broadening of  $\eta = 0.04$  eV has been used.

approximating the position operator gives very good results, and can give a right prediction of the highest peak in the imaginary part of the bulk silicon dielectric function.

Another interesting quantity is the static dielectric constant, which can be calculated either as the  $\omega \rightarrow 0$  limit of the real dielectric function, or starting from the knowledge of  $\epsilon_2(E)$  through the relation:

$$\epsilon_s = 1 + \frac{2}{\pi} \int_0^\infty \frac{\epsilon_2(E)}{E} dE. \quad (2.75)$$

In table (2.8) we report on a comparison between the calculated values of  $\epsilon_s$  and the experimental value. Calculations have been performed with Niquet [28] and Tserbak [27] parametrizations and with the Chelikowsky Local Pseudopotential form factors [12], the experimental data is taken by [52]. An error of about 10% is usually ascribed to excitonic effects.

Method	$\epsilon_s$
TB Niquet	10.74
TB Tserbak	10.63
EPM CC	10.53
Exp	11.40

Table 2.1: Bulk Si static dielectric constant.



# Chapter 3

## Spherical nanocrystals

### 3.1 Introduction

In this chapter we apply the Empirical Tight Binding method to the study of Silicon spherical nanocrystals. In a first step, the nanocrystal energy levels are calculated. The energy gap between the Highest Occupied Molecular Orbital (HOMO) and the Lowest Unoccupied Molecular Orbital (LUMO) is compared to the experimental data and to other theoretical results available in literature. The situation that comes out is quite chaotic, and a large scatter of the many measured and calculated energy gaps can be observed. Nevertheless, the ETB is seen to fit quite well most of the data, both for small and large nanocrystals.

The second part of the chapter concerns the optical properties. A comparison of a nanocrystal extinction coefficient with an experimental result is shown. This is a good check that the ETB works well. Then, the imaginary part of the nanocrystal dielectric function is studied. On increasing the nanocrystal size, the energy gap between the first transition energy and the

threshold of the absorption spectrum rapidly increases with it. This is an interesting feature of the Si nanocrystals, and is related to the fast annihilation of the oscillator strengths and to the rise of the radiative recombination time. The matter is discussed in detail, investigating the projection of the nanocrystal states on the bulk states. It comes out that the  $\mathbf{k}$ -space overlap between the HOMO and LUMO states rapidly nullifies, when the nanocrystal size increases. This behavior can well explain the exponential increase of the radiative recombination times. Finally, the static dielectric constant has been studied, and a comparison with other theoretical calculations is discussed.

## 3.2 The method

The application of the ETB to the nanocrystals is very simple. A nanocrystal can be thought of as composed by three parts: (1) an inner core, (2) a relaxed shell, and (3) a passivant layer. Inside the inner core the atoms behave as in the bulk, being the surface far enough that its effects are negligible. The relaxed shell covers the nanocrystal core, and the surface effects have to be taken into account. The atoms in the shell relax from their bulk positions, and a modulation of the Hamiltonian parameters is expected. Finally the nanocrystal is covered by a passivant layer, usually constituted by Hydrogen, Oxygen or Si dioxide. From an experimental point of view, the nanocrystals are always passivated, and the species covering the structures are determined by the experimental setup. The inclusion of the passivant layer into a theoretical model is very important, in order to avoid the appearance of *dangling bonds* (uncovered Si atoms), or bonds with other species (for instance, a sin-

gle Oxygen on a fully Hydrogenated surface). The presence of even a single *dangling bond* on the nanocrystal surface leads to the formation of a localized state with energy well inside the gap. These localized states work as electron traps, decreasing the nanocrystal optical efficiency and activating non-radiative recombination channels.

The ETB approximation in the study of nanocrystals consists on modelling the nanocrystal as formed by only an inner core and a passivant layer. Therefore, the method neglects the surface effects, and we shall not take into account the relaxation effects on the atomic positions, with the consequent modulation of the Hamiltonian parameters. This idea of *transferability* [4] of the Hamiltonian parameters from the bulk to the nanostructures indeed works well, as it has been shown by years of applications of ETB [21, 23, 24, 28, 43, 53–57].

For our calculations, we have used the  $sp^3$  3<sup>rd</sup> nearest neighbor ETB [28], which give a good estimation of the Bulk Si fundamental band gap and effective masses. We have studied spherical nanocrystals with a Si atom in the center, with the surface passivated by Hydrogen atoms. We have taken for Hydrogen only the 1s orbital, using the Si-H interaction parameters from Niquet [28], which have been chosen in such a way to reproduce the SiH<sub>4</sub> absorption spectra.

From the computational point of view, we have factorized the Hamiltonian matrix according to the five irreducible representations of the  $T_d$  symmetry group. Using the group theory, we have been able to reduce the size of the diagonalization problem, label the energy levels of the nanocrystal, and therefore use the selection rules for studying the dipole-allowed transitions.

The ETB method is a very efficient tool in the study of nanocrystals. In fact, the method needs very few atomic orbitals for each atom in the structure. Within the  $sp^3$  parametrization, only 4 functions are required for each silicon atom. This leads to very small matrices compared, for instance, to the Plane Wave methods, where at least one hundred basis functions are required for each atom. Moreover, the TB matrices show a huge degree of sparsity, which can be used to further reduce the computational effort<sup>1</sup>. This has been done using an iterative diagonalization routine, which makes a heavy use of the sparsity for calculating the first  $m$  eigenvectors of a  $N \times N$  matrix. Starting from the Hamiltonian matrix  $H$ , we have applied a folding procedure, near a reference energy  $\epsilon$ . We calculate the square matrix:

$$H_2 = (H - \epsilon)^2, \quad (3.1)$$

and from the eigenvalues of  $H_2$  we easily retrieve the  $H$  eigenvalues. With this procedure we reduce the problem of calculating a set of eigenvalues in the neighborhood of an energy reference, to the problem of calculating the first  $m$  eigenvalues of a given matrix. Making use of the sparsity, the overall computational time is reduced to a linear scaling:

$$t \propto m^2 N, \quad (3.2)$$

which is much faster than the  $t \propto N^3$  trend of the standard computational routines. In order to have an idea of the ETB efficiency, we want to give some numbers. Let us consider  $Si_{1707}H_{628}$ , a spherical nanocrystal with a 4 nm

---

<sup>1</sup> We have seen that an interaction up to  $3^{r_d}$  neighbors allows us to well reproduce the Si-Si Hamiltonian matrix elements, as it results from the fair agreement of the gap energies and the effective masses with the experimental results. Moreover, the use of a finite interaction range allows to put equal to zero all the further interactions, leading to very sparse matrices.

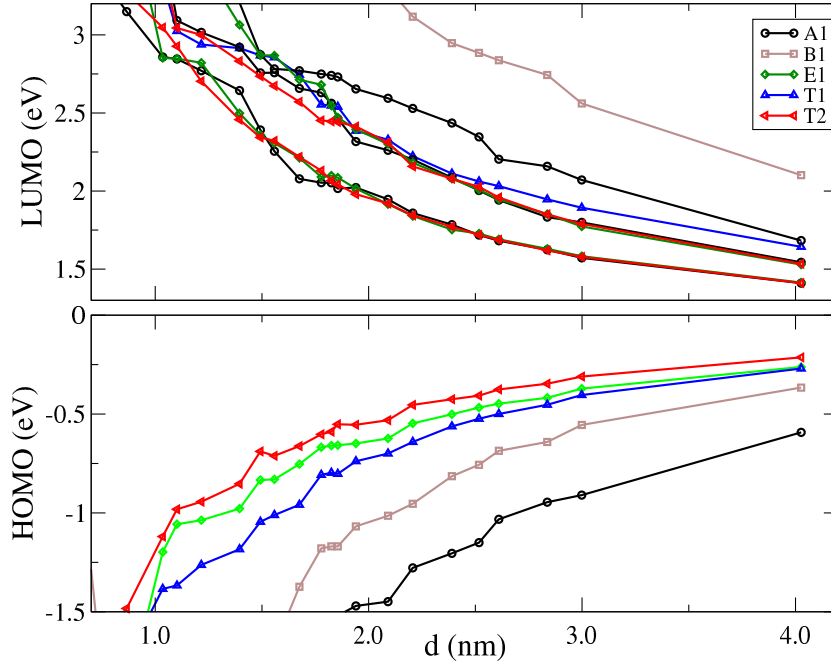


Figure 3.1: HOMO and LUMO states for spherical nanocrystals on varying their diameter. The lines are guides for the eyes.

diameter. The Hamiltonian matrix for this nanocrystal has a size  $N = 7456$ , with 664448 non null elements. This means that only the 1.2% of the whole matrix is different from zero! A larger nanocrystal is  $Si_{5707}H_{1372}$ , with a  $d = 6$  nm diameter. In this case the size of the problem is  $N = 24200$ , and the number of non null elements is only the 0.4% of the whole matrix.

### 3.3 Energy levels

In a first step, we have calculated the energy levels for a set of hydrogenated spherical nanocrystals, with increasing size. For each nanocrystal, the effective diameter is calculated as follows [28,58]. In the bulk, ideal structure, the volume associated to each Si atom is  $v_{Si} = a^3/8$  ( $a \simeq 0.5431$  nm is the Si lat-

tice constant). A good estimation of the nanocrystal volume can be  $v_{Si}N_{Si}$  from which, assuming a spherical shape, the diameter is easily calculated using the relation [28]:

$$d = a \left( \frac{3}{4\pi} N_{Si} \right)^{1/3} = 0.33691 N_{Si}^{1/3}. \quad (3.3)$$

In Fig. 3.1 we show the energy levels, labelled according to the five irreducible representations of the  $T_d$  symmetry group. The quantum confinement effect is well visible. In fact, on increasing the nanocrystal size, the HOMO energies increase, while the LUMO energies decrease, and the gap energy goes down to the bulk value of 1.1 eV.

In figure 3.2 we show the calculated first transition energy for spherical nanocrystals with increasing diameter. Our theoretical results have been indicated by means of crosses, while the solid line is a fit of the numerical data [28]. We compare the first transition energy to different sets of experimental results, coming from both photoluminescence (PL) and absorption (Abs) measurements. We want to point out the great difficulty in such a comparison. In fact, in literature there is a large scatter of the experimental data, caused by the different experimental setup that make the reproducibility of the measurements a formidable task. For instance, we expect different results between Porous Silicon (PSi) samples<sup>2</sup>, and Si nanocrystal (Si nc) samples. Another point is the kind of measurements performed on the samples. As a matter of fact, it is generally observed an energy difference, named the *Stokes shift*, between the absorption threshold and the main photoluminescence emission peak energy, with an effect that is stronger for smaller nanocrystals [57, 60–62]. It is of great interest to compare both the

---

<sup>2</sup> PSi has been shown with many experimental evidences to be constituted by Si nanocrystals [59].

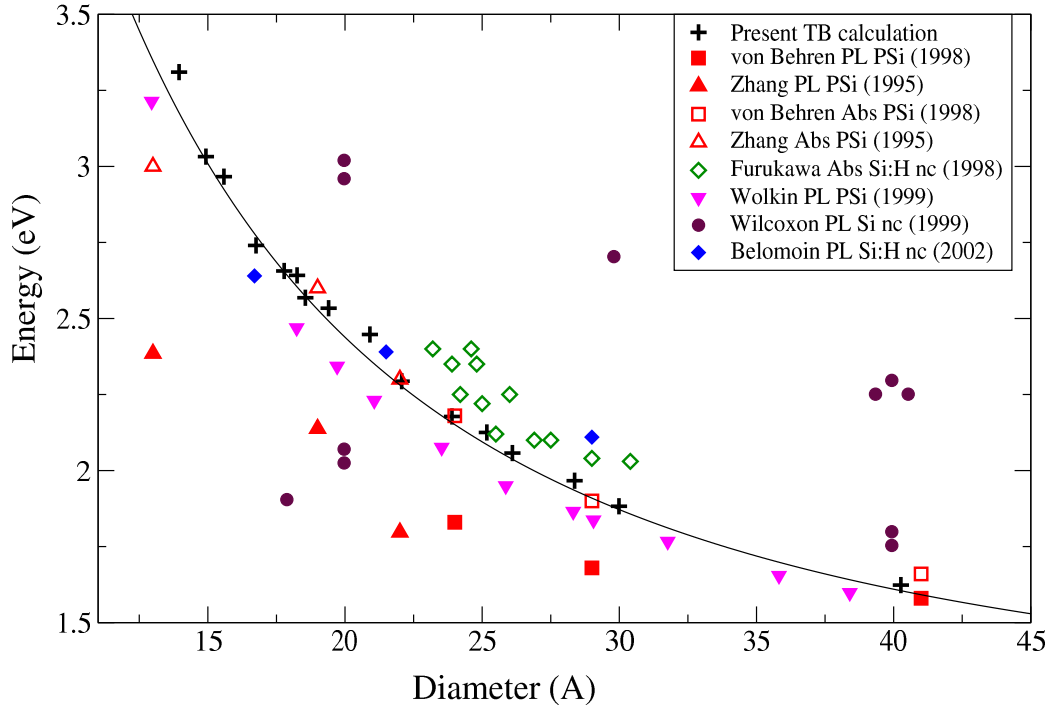


Figure 3.2: The first dipole-allowed transition energy (optical gap) for different nanocrystals with increasing size (crosses). The solid line is a fit of the calculated data. The experimental absorption (open symbols) and photoluminescence emission (filled symbols) are also shown for comparison. Squares are from [63], triangles-up from Ref. [64], open diamonds from [65], triangles-down from [66], filled circles from [67], filled diamonds from [68].

absorption and the photoluminescence data. In Fig. 3.2 we have included two couples of absorption and photoluminescence measurements (triangles-up and squares) performed on the same sample. From the theoretical point of view it is not completely clear the origin of the Stokes shift, even if many models have been proposed.

In the recent years, the fundamental role of the surface on the optical properties of nanocrystals has been becoming clearer. The presence of even just one Oxygen atom on an Hydrogenated surface can lead to a significantly

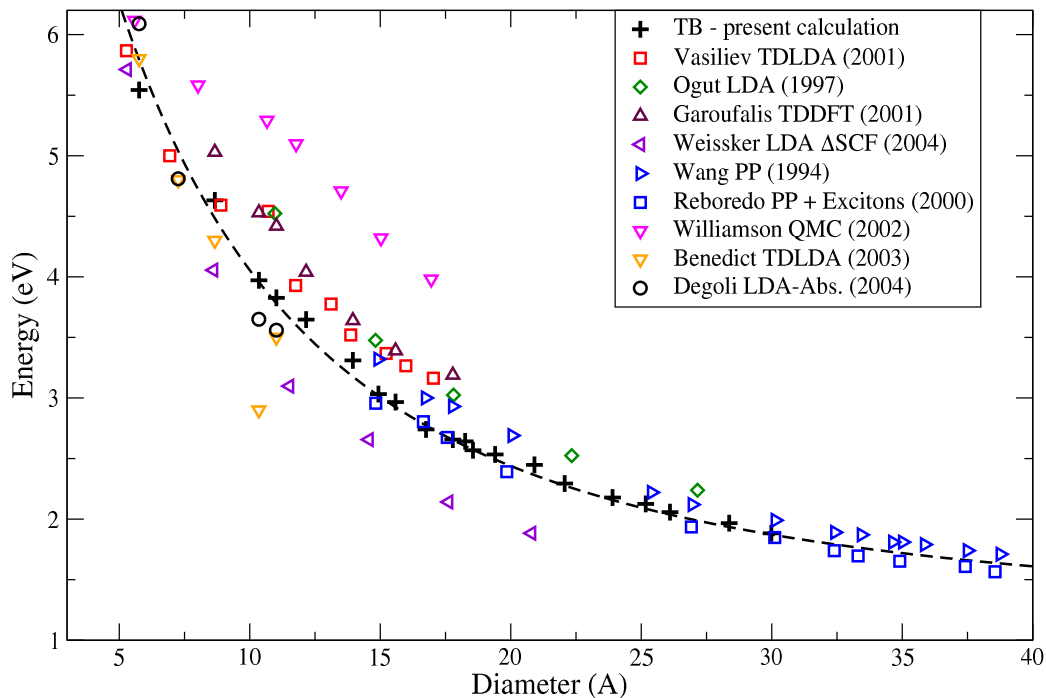


Figure 3.3: Spherical nanocrystals optical gap: comparison with other calculations. We have shown our calculated first dipole-allowed transition energies by open circles, while the solid line is a fit. Density functional data: red squares are taken from [70], green diamonds from [71], triangles-up from [72], triangles left from [73], yellow triangles-down from [74], green squares from [62]; Empirical Pseudopotential: triangles-right from [16], blue squares from [75]; the Quantum Monte Carlo results (pink triangles-down) are taken from [76].

red-shift of the optical gap, especially for small nanocrystals [69]. And an exposure in air of a sample, even for a few minutes, can decrease the PL peaks energies up to 1 eV [66]. In this respect, the triangles-down data of Wolkin [66] come out from carefully cleaned, Oxygen-free samples. The fair agreement of the present calculation with the Wolkin data is indeed an important experimental check that the method does indeed work well.

In Fig. 3.3 we show a comparison between our results and other theoretical results for Hydrogenated, spherical Si-nc. Also in this case there is

a large scatter of the calculated data, and this is especially true for the *ab initio* methods. Some considerations can be inferred by the graph. First of all, there is a good agreement with the other important semiempirical method, based on the Pseudopotentials (PP). In figure, PP calculations without (triangles-right) [16] or with the inclusion of the Coulomb e-h interaction (squares) [75], have been shown in blue. It is worth noting that the PP trend is very similar to our results, with a better agreement for larger nanocrystals. The situation for small nanocrystals is more complicated. Even for data reproduced within the same approach, like the Time Dependent Density Functional Theory (TDDFT), we can have quite different results. For instance, the Garoufalis [72] and Vasiliev [70] results are at higher energies than the Benedict [74] calculations. The methods differ in the choice of the Exchange-Correlation Kernel, and for an alternative definition of the optical gap, in the case of Ref. [70]. Instead, for the local density approximation (LDA), the problem consists in the lacking of an exact theoretical definition of the optical gap. The various approaches are based on a different definition of the optical gap [62, 71, 73], and there is an open debate on the subject. Looking at Fig. 3.3, it is interesting to note that our curve goes through all these data. In particular, we want to underline the fair agreement of our calculation with the most recent TDLDA calculations of Benedict [74], and the LDA results of Degoli [62].

### 3.4 Dielectric function

We have applied our TB method to the study of the nanocrystal dielectric function. As a check of our method, we have considered the  $Si_{159}H_{124}$

nanocrystal (which has an equivalent diameter of 1.83 nm), and compared the calculated extinction coefficient (related to the dielectric function) to an experimental curve, given by Wilcoxon for a silicon nanocrystal with a diameter of about 1.8 nm. In Fig. 3.4 the two curves are shown. The arrow indicates the first calculated transition energy. We have rescaled our theoretical data in such a way the two curves have the same height of the main peak. We want to point out the great similarity of the two curves. In fact, an overestimation of the calculated dielectric function is intrinsic of our parametrization, as it was clear already for the bulk, from Fig. 2.2. Nevertheless, there is a fair agreement in the relative intensities of the two main peaks, and in the overall broadening of the two curves.

In Fig. 3.5 we show the imaginary part of the dielectric function for a set of spherical silicon nanocrystals. A black solid arrow shows the first dipole allowed transition energy. On increasing the nanocrystal size, the first transition energy goes down quite fast, approaching the electron-forbidden bulk indirect band gap of 1.1 eV. On the other hand, the onset of the imaginary part of the dielectric function (and the threshold of the absorption coefficient) is much less sensitive to the size. A quantitative evaluation of the absorption threshold can be done using an experimental technique, consisting in calculating the integral absorption cross section. In fact, for molecules and direct gap semiconductors the absorption threshold is usually defined as the energy of the first allowed transition. However, in the case of Si, which has an indirect-gap behavior, we find a large number of very weak transitions at low energy. The indirect-gap behavior is well visible even for Si nanocrystals, leading to an experimentally observed onset of the absorption well above the

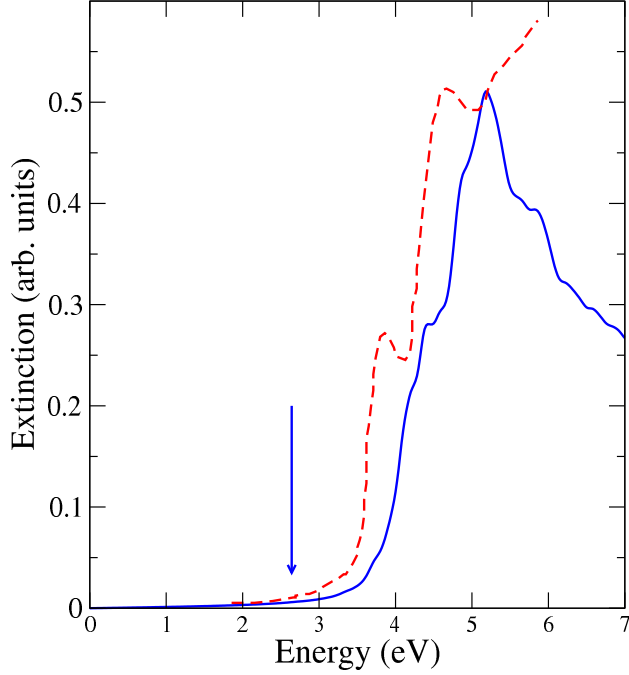


Figure 3.4: Extinction coefficient for a  $d = 1.8$  nm Si nanocrystal from absorption measurements [67], compared to a  $Si_{159}H_{124}$  nanocrystal ( $d=1.83$ nm) studied with our TB method. The arrow label the first calculated transition energy.

first dipole allowed transition energy. Therefore, a different definition of the absorption gap is needed in this case.

By studying the integral absorption cross section, we are able to take into account the cumulative effect of this great number of weak transitions, that lie in the vicinity of the band edge [70, 77]. We use the following definition of the photoabsorption cross section [78]:

$$\sigma(E) = 2 \frac{F_e}{4N_{Si}} \sum_{n,n'} f_n (1 - f_{n'}) F_{nn'} S(E - E_{nn'}), \quad (3.4)$$

where  $E_{nn'}$  and  $F_{nn'}$  are the transition energy and the oscillator strength for the  $n \rightarrow n'$  transition,  $f_n$  is the  $n^{th}$  level occupation, and the factor 2 takes into account the spin degeneracy. We have defined the so called complete

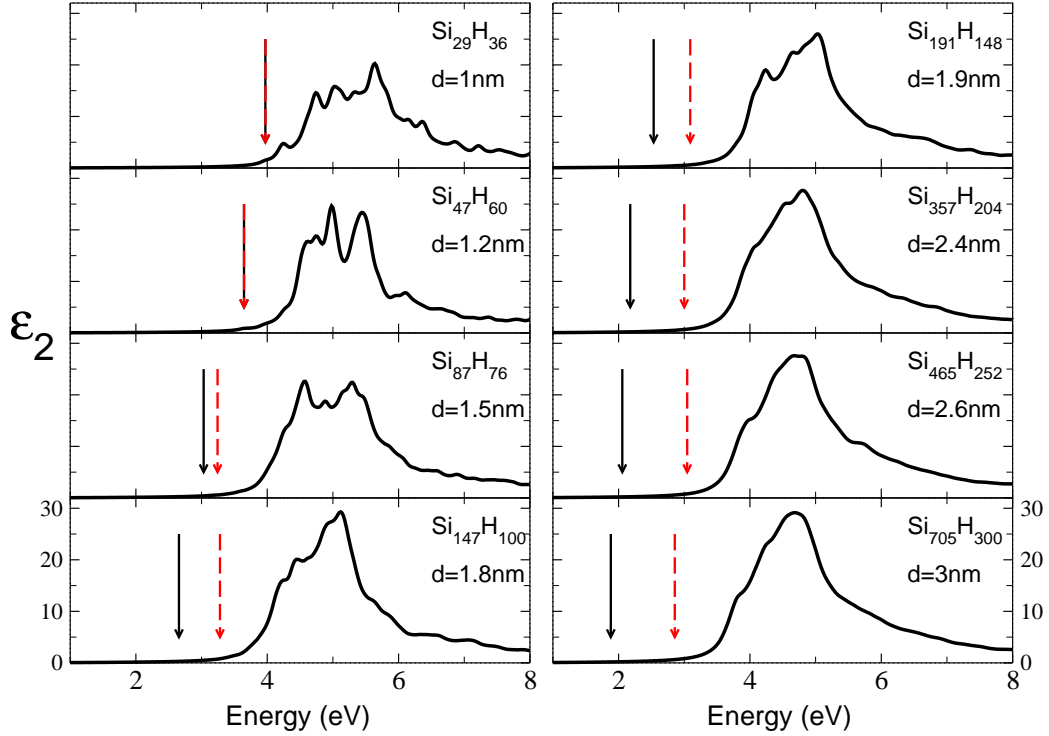


Figure 3.5: Imaginary part of spherical nanocrystals dielectric function, on increasing diameters. A 0.1 eV Lorentzian broadening has been used. The black arrows show the first dipole allowed transition, while the red arrows show the absorption threshold.

one electron oscillator strength  $F_e$  [77, 79] as:

$$F_e = \frac{2\pi^2\hbar e^2}{mc} \simeq 1.098eVA^2. \quad (3.5)$$

We suppose that the nanocrystal is embedded in a dielectric medium with a refraction index  $n = 1$ , and we neglect local field effects. Starting from the one electron cross section in Eq.(3.4), we define the absorption gap as the energy  $E_g$  such as:

$$\int_0^{E_g(p)} \sigma(E)dE = pF_e. \quad (3.6)$$

This procedure allows the determination of an energy  $E_g(p)$ , that depends on the external parameter  $p$ . We expect that  $p$  is related to the precision of the

experimental set up (in other words to the smallest oscillator strength which can be detected). We use the value  $p = 10^{-4}$ , which is consistent with the experimental measurements [79,80]. For each nanocrystal we have calculated the absorption gap. In Fig. 3.5, for each nanocrystal, we use a red dashed arrow to show the absorption gap. As we expected, the absorption gap lies exactly on the threshold of the imaginary part of the dielectric function. While for small structures,  $E_g$  lies quite close to the first transition energy, for large nanocrystals the energy gap between the two curves becomes very large. This is due to a huge number of very weak low energy transitions that, on increasing the nanocrystal size, tend to become zero. This interesting feature of Si nanocrystals will be analyzed in more detail in the next sections.

### 3.5 Oscillator strengths

In order to better understand the optical behavior in the vicinity of the band edge, we have calculated the first Oscillator Strengths (OS) and the radiative recombination times. In Fig. 3.6, on the right side, we show the OS versus the transition energies. On increasing the nanocrystal diameter, the quantum confinement effects lead to a decrease of the transition energies. At the same time, also the OS decrease, but much faster. This result is in a good agreement with the first DFT calculations of Delley [81]. Moreover, very recently Dovrat has reported on OS measurements as a function of the transition energy, which show an exponential dependence [80]. Even if the experimental conditions are quite different (nanocrystals embedded in a silicon dioxide matrix) and the considered sizes are larger than the ones studied here, it seems that both the trend and the order of magnitude are

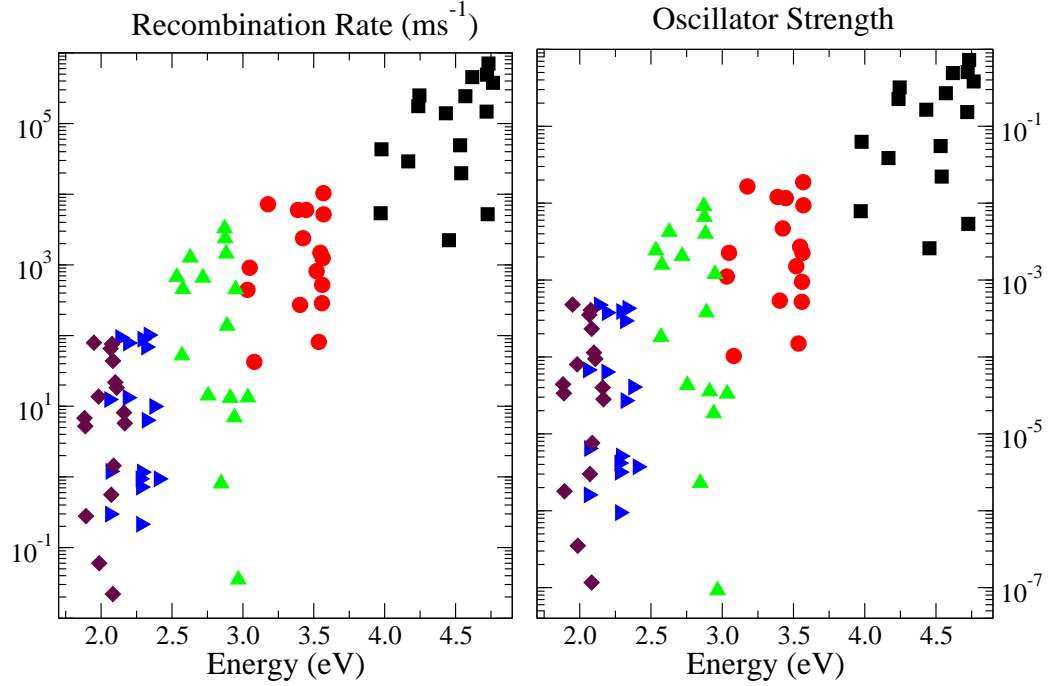


Figure 3.6: First lowest-energies recombination rates (left) and oscillator strengths (right) of spherical silicon nanocrystals on varying the diameter.  $Si_{29}H_{36}$  ( $d = 1.0$  nm), squares;  $Si_{87}H_{76}$  ( $d = 1.5$  nm), circles;  $Si_{191}H_{148}$  ( $d = 1.9$  nm), triangles-up;  $Si_{465}H_{252}$  ( $d = 2.6$  nm), triangles-right;  $Si_{705}H_{300}$  ( $d = 3$  nm), diamonds.

in a good agreement with our results. For instance, Dovrat finds an OS of about  $4 \times 10^{-3}$  for a transition energy of about 1.9 eV, where we find a value of  $5 \times 10^{-3}$  at 1.95 eV.

On the left side of Fig. 3.6, we show our calculated recombination rates, that we define as the inverse of the radiative recombination time [78]:

$$\frac{1}{\tau_{rad}} = \frac{2e^2}{\hbar^2 mc^3} E_{vc}^2 F_{vc}. \quad (3.7)$$

We have calculated it for the lowest energies transitions from occupied to unoccupied states. On increasing the nanocrystal size, the transition energies decrease, their recombination rates decrease and the radiative recombination

time increases. Already for a 3 nm nanocrystal, with energies at about 2 eV, we have the recombination time  $\tau_{rad} \simeq 10\mu s$ . When the nanocrystals size changes from a few Å to several nanometers, the radiative recombination times change from the range of the *ns* ( $d \simeq 1$  nm) to the  $\mu s$  ( $d \simeq 3$  nm) to the *ms* (bulk Si). Even in this case a comparison with the experimental data would be of huge interest. Radiative recombination times for Si Hydrogenated spherical nanocrystals have already been calculated in the past [53], and a comparison between experiments and theoretical results has been recently tried [73].

### 3.6 k-space projections

The decrease of the oscillator strengths and the increase of the radiative recombination times, on increasing the nanocrystal size, can be well explained looking at the projection of the nanocrystal eigenvectors on the bulk states. The TB interpolation scheme gives the eigenfunctions of the bulk Si Hamiltonian in terms of the atomic orbital basis set. In ket notation, joining the equations (1.6) and (1.9), we can write:

$$|n\mathbf{k}\rangle = C \sum_{\sigma, \mathbf{R}, \mu} B_{\sigma n}^{\mu}(\mathbf{k}) e^{i\mathbf{k} \cdot \mathbf{R}_{\mu}} |\sigma\mu\mathbf{R}\rangle, \quad (3.8)$$

where  $C$  is a normalization constant depending on the structure volume, and the sum is done all over the atomic orbitals. Instead, we can write the expansion:

$$|m\lambda\rangle = \sum_{\sigma, \mathbf{R}, \mu} C_{\sigma m}^{\lambda}(\mathbf{R}_{\mu}) |\sigma\mu\mathbf{R}\rangle, \quad (3.9)$$

for the  $m^{th}$  nanocrystal state of the  $\lambda$  irreducible representation of the  $T_d$  symmetry group, where the eigenvectors come out from the diagonalization

procedure. In order to quantitatively understand how much a nanocrystal state is far from a bulk state, we define the projection operator:

$$\hat{P}(\mathbf{k}) = \sum_n |n\mathbf{k}\rangle \langle n\mathbf{k}|. \quad (3.10)$$

The sum is done on the whole band-complex constituted by the top valence and the lowest conduction bands. We sum over the 8 calculated Tight Binding bands. This projection operator gives the nanocrystal states component on Bloch states with a fixed value of the crystalline momentum  $\mathbf{k}$ . It is important to note that for the confined systems the crystalline momentum is not a good quantum number, due to the lack of periodicity. Nevertheless, being both the bulk crystal Bloch states and the nanocrystal states expressed as a linear combination of the same atomic wavefunctions (see Eqs. (3.8) and (3.9)) the projection operator (3.10) allows to understand the size for which bulk states are almost retrieved. It is expected that beside a threshold size, the quantum confinement effects become negligible, and almost Bloch-like states are observed.

From Fig. 3.1 the behavior of spherical nanocrystal HOMO and LUMO states was visible. While the HOMO states have a quite size-independent  $T_2$  symmetry, the LUMO states indifferently show an  $A_1$ ,  $E_1$  or  $T_2$  symmetry, according to the diameter [28, 82]. Nevertheless, it is quite clear that, except for very small structures (with a few Si atoms), we have a 6 quasi-degenerate LUMO level, where the first six  $A_1 + E_1 + T_2$  states are very close in energy. This is fully consistent with the EMA theory, which gives the prediction of such sixfold degenerate LUMO states, due to the existence of six minima in the Bulk Si first conduction band. So, we have calculated the  $k$ -space projection for both (1) the threefold degenerate HOMO states and (2) the

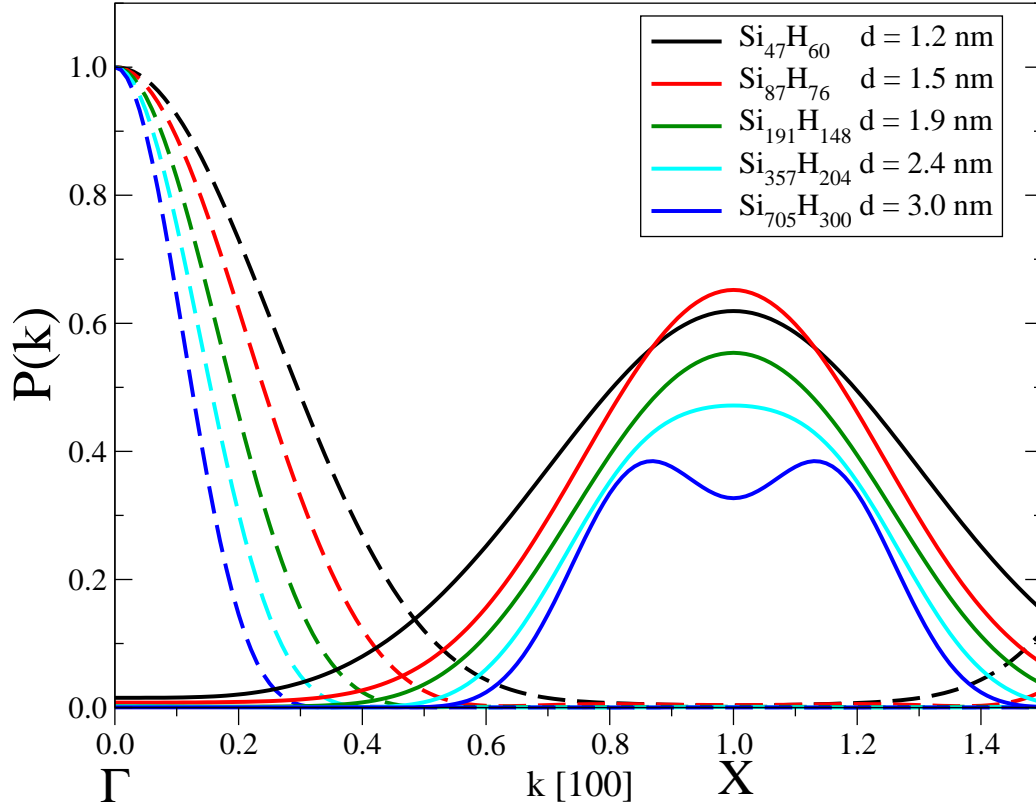


Figure 3.7:  $k$ -space projection of the eigenstates for nanocrystals with different sizes. The dashed and the solid lines are respectively the projections of the HOMO and LUMO states. The normalization has been done in such a way that the HOMO states projection is 1 in  $\Gamma$ .

sixfold quasi-degenerate LUMO states:

$$P(\mathbf{k}) = \sum_{m,\lambda} \langle m\lambda | \hat{P}(\mathbf{k}) | m\lambda \rangle. \quad (3.11)$$

The sum is done over all the 3 degenerate (or the 6 quasi-degenerate) states.

In Fig. 3.7 the  $\Delta$  line projection is shown for both the HOMO and LUMO states, for our set of spherical nanocrystals. The HOMO states have component especially at  $\Gamma$ , whereas the LUMO states have fundamentally an  $X$  behavior. It is worth noting that, on increasing the nanocrystal diameter, the overlap between HOMO and LUMO states annihilate in a quite fast way.

Together with this, we want to point out that the LUMO projection is well centered on  $X$  when the nanocrystal size is smaller than a certain threshold. For diameters higher than this threshold, the maximum of the LUMO states goes away from  $X$ , tending to the bulk limit of about 0.83. Therefore, we can differentiate the behavior of Si nanocrystals. For small sizes, there is a good  $k$ -space overlap of the HOMO and LUMO states, leading to non negligible OS strengths, recombination times of  $\mu s$  or  $ns$  and the absorption gap close to the HOMO-LUMO transition energy. For large sizes, instead, there is a very small overlap of the HOMO and LUMO states, the LUMO states tend to be centered at  $k = 0.83$ , the OS are very small, while the radiative recombination time becomes of the order of  $ms$ . The nanocrystals retrieve the bulk Si indirect gap behavior. This is very clearly understood from Fig. 3.7.

### 3.7 Dielectric constant

In recent years, a huge interest has been devoted to the study of the Si nanocrystal screening properties [58, 83–85]. This is an important task, because it is related to the calculation of the electron-hole interaction energy. We have calculated the static dielectric constant  $\epsilon_s$  for our spherical nanocrystals. In Fig. 3.8 we show our results (with circles), together with other theoretical curves. We have rescaled the values in order to retrieve the experimental bulk limit. We have shown in figure the Empirical Pseudopotential calculations (PP) of Ref. [58], the generalized Penn model (GPM) [58], and the self-consistent TB results of Ref. [83]. The PP calculations have been performed using the same procedure that we have used here, starting from the

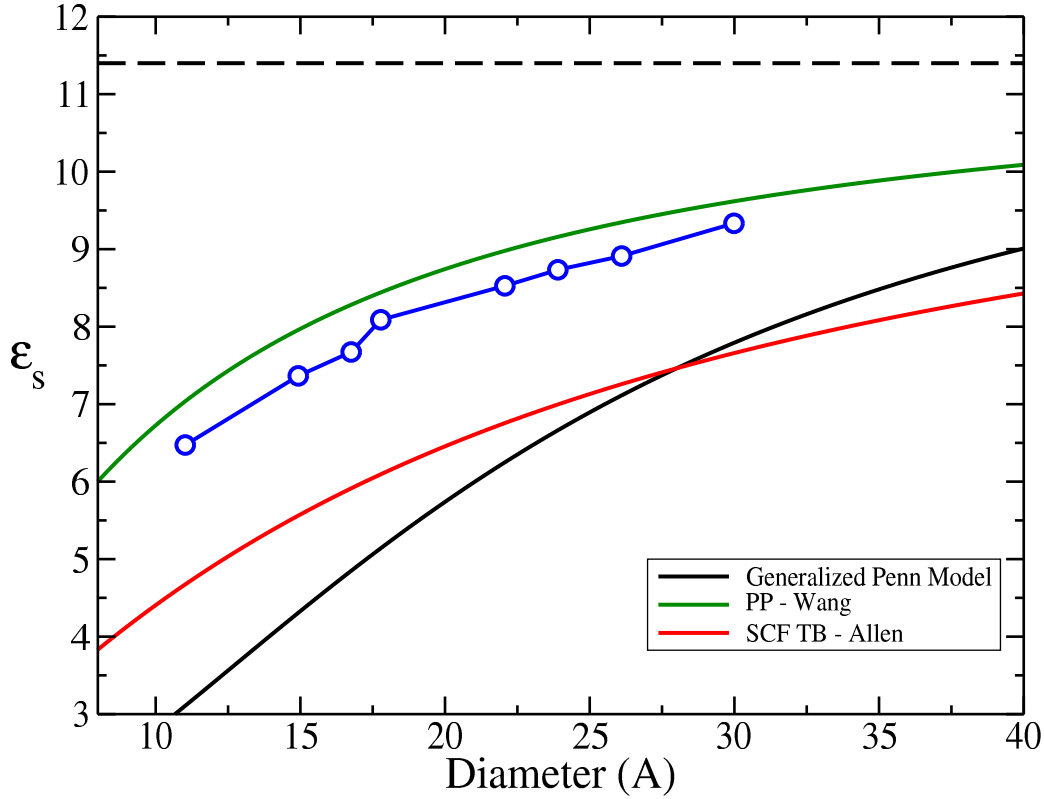


Figure 3.8: Calculated static dielectric constant for Si spherical nanocrystals. Circles correspond to our Tight Binding results (the line is only a guide for the eyes). The green lines are the Pseudopotential fits from Ref. [58] The black line corresponds to the generalized Penn model [58] while the red line is a calculation performed within a self-consistent potential Tight Binding model [83]. The bulk limit of 11.4 has been shown for comparison.

imaginary part of the RPA dielectric function and calculating the dielectric constant through Eq. (2.75). Indeed the agreement is quite good. The GPM is a model based on the nearly free electron gas for the band energies [86], and is expected to give good results in the limit of large nanocrystals. Instead, the self consistent TB [83] is applied to the problem of the nanocrystal screening by an hydrogenic impurity, and gives quite different results.



# Chapter 4

## Ellipsoidal nanocrystals

### 4.1 Introduction

In this chapter the optical and infrared properties of silicon ellipsoidal nanocrystals are illustrated. First, the anisotropy of the Photoluminescence from Porous Silicon samples is briefly described. This phenomenon can be considered as the experimental evidence of the realization of silicon ellipsoids, motivating our interest in this field. The nanocrystals that we have studied have a revolution axis along the  $[001]$  lattice direction. In a first step, the ellipsoidal axes lying in the plane perpendicular to the  $[001]$  direction have been kept fixed to a value of 2 nm, while the axis along the symmetry direction has been varied.

The optical properties of these nanocrystals have been studied, and the dependence of the dielectric tensor anisotropy on the geometrical anisotropy has been carefully analyzed. A particular interest has been focused on the onset of the absorption cross section, which has a significant dependence on the structure aspect ratio. A comparison between ellipsoids and quantum

wires is illustrated, showing that the quantum wire limit is reached for not large values of the aspect ratio. Next the static dielectric constant has been investigated. This is the first time that a similar calculation is performed. It can be of great importance in the study of the screening properties of ellipsoidal nanocrystals.

A second part of the work has been focused on the LUMO states and the infrared intraband transitions for very large ellipsoidal nanocrystals. A set of fixed semiaxes nanocrystals, and a set of fixed volume ellipsoids have been studied. The equivalent diameter of the structures is about 6 nm, and nanocrystals with up to tens of thousands of Si atoms have been analyzed. We have verified that for such huge sizes the Empirical Tight Binding gives results fairly consistent with the Effective Mass Approximation predictions.

## 4.2 Porous Silicon Photoluminescence

We want to begin the discussion on the optical properties of Si ellipsoids by pointing out their experimental evidence. Since its discovery in 1990 [88], the huge Photoluminescence (PL) from Porous Silicon samples (PSi) was explained in terms of Quantum Confinement Effect (QCE), assuming that quantum wires or, better, small photoluminescent nanoparticles are responsible of the Photoluminescence from porous silicon. Over the years, many alternative models have been suggested as at the origin of the PSi PL, such as hydrogenated amorphous silicon, defects, luminescent molecules or surface states [59]. But, after years of experimental and theoretical work, nowadays the QCE hypothesis is the most accepted one to explain the PL. Among the many proofs, TEM images have clearly shown the presence of Si nanocrystal-

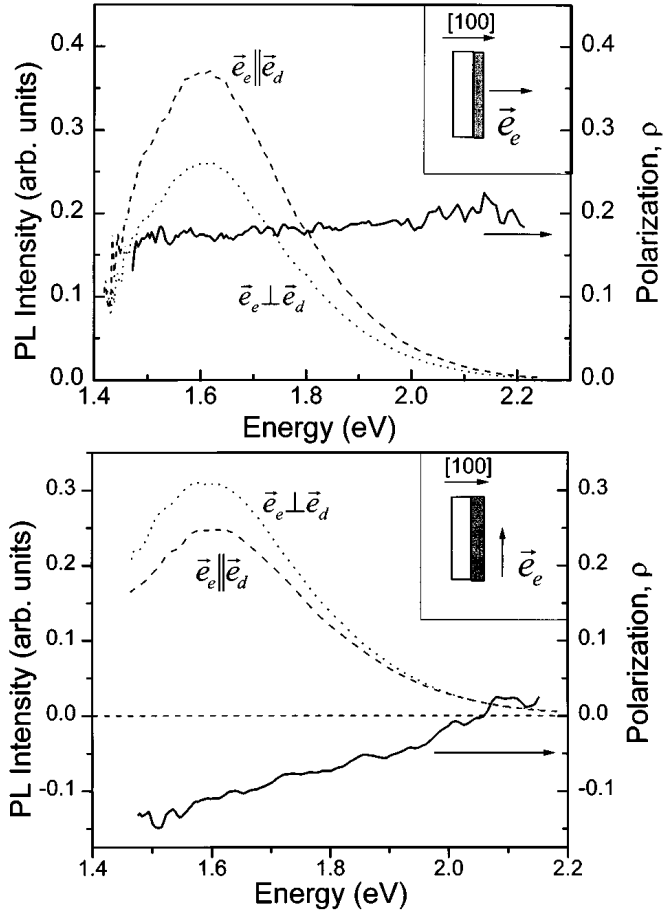


Figure 4.1: PL Anisotropy from a Porous Silicon layer (results taken from Ref. [87]). The sample has been exposed to an exciting radiation with a polarization vector parallel (upper figure) or perpendicular (lower figure) to the [100] growth direction. The PL radiation, with either parallel or perpendicular polarization with respect to that one of the exciting light, has been detected. The resulting degree of linear polarization of the detected light with respect to the exciting light, defined in Eq. (4.1), is also shown in figure.

lites in PSi samples. In addition, the great similarity of the PL from PSi and Si nanocrystals (Si-nc) has been supported by numerous evidences [89]. Nevertheless, an important difference exists between the two kinds of PL. While in the case of Si-nc an isotropic PL is observed, PSi samples are characterized

by a strong PL anisotropy. The reason at the basis of this phenomenon is quite clear, in that a porous silicon layer has a preferred orientation along the growth direction. We expect the formation of quantum wires, and pores, and elongated structures with a revolution axis parallel to the growth direction. In an important paper, Kovalev [87] measured the PL polarization for a PSi layer having a [100] growth direction. In Fig. 4.1 we report on the results of that paper. The degree of linear polarization has been defined as:

$$\rho = \frac{I_{\parallel} - I_{\perp}}{I_{\parallel} + I_{\perp}}, \quad (4.1)$$

where  $I_{\parallel}$  ( $I_{\perp}$ ) is the PL radiation polarized parallel (perpendicular) to the exciting light polarization. From Fig. 4.1 it clearly results a change of sign of  $\rho$ , when the exciting radiation changes its polarization from parallel to perpendicular, with respect to the [100] direction. This behavior is a clear proof of the strong PL anisotropy from PSi, whose emission radiation has a preferred [100] polarization. Kovalev [87] showed that the degree of anisotropy could be fairly fitted assuming that the PSi PL comes from a distribution of ellipsoidal Si nanocrystals, which can have either an elongated or a flattened shape. Most of the ellipsoids have a symmetry axis parallel to the [100] growth direction.

### 4.3 Silicon ellipsoids

We have applied our TB method to the study of Si ellipsoidal nanocrystals, having a rotational symmetry axis along the [100] direction. The ellipsoid surface is defined by the equation:

$$\frac{x^2 + y^2}{a^2} + \frac{z^2}{c^2} = 1, \quad (4.2)$$

where the origin of the coordinates has been taken on a Si atom. Here,  $a$  and  $c$  are the semi-axes along, respectively, the parallel and the perpendicular direction with respect to the symmetry axis. An important feature of the structures is  $\chi = c/a$ , the ellipsoid aspect ratio, which is a measurement of their geometric anisotropy. The ellipsoid symmetry group, within the TB approximation (in which the atoms do not relax from their bulk positions), is  $D_{2d}$ , a subgroup of the full Bulk Si point group.  $D_{2d}$  is constituted by 8 elements, and 5 irreducible representations (IR): the unidimensional  $A_1, A_2, B_1, B_2$  and the unique bi-dimensional  $E_1$  (see Appendix B for the character table and the symmetries related to the IR). The irreducible representations will be used to label the energy levels, and to define the transition rules.

In the first part of the work, a set of ellipsoidal nanocrystals, having a fixed value of the semi-axes lying in the  $xy$  plane, has been studied. A value  $a = 1$  nm has been chosen, and the optical properties of the ellipsoids have been investigating on varying the aspect ratio  $\chi$ . From a geometrical point of view, the nanocrystals tend to a quantum disk, in the limit of very small values of  $\chi$ . In the opposite limit,  $\chi \rightarrow \infty$ , the ellipsoids go to the cylindrical quantum wire, having a circular radius of 1 nm. The number of Silicon atoms increases almost linearly with the aspect ratio. Therefore, the signature of both the anisotropy due to the different sizes of the ellipsoids along different directions, and a quantum confinement effect, caused by the increase of the total number of atoms, is expected to be found in the optical properties.

In Fig. 4.2 the energy levels for the ellipsoids are shown. It is worth noting that, at least in the studied range of aspect ratios, both the LUMO

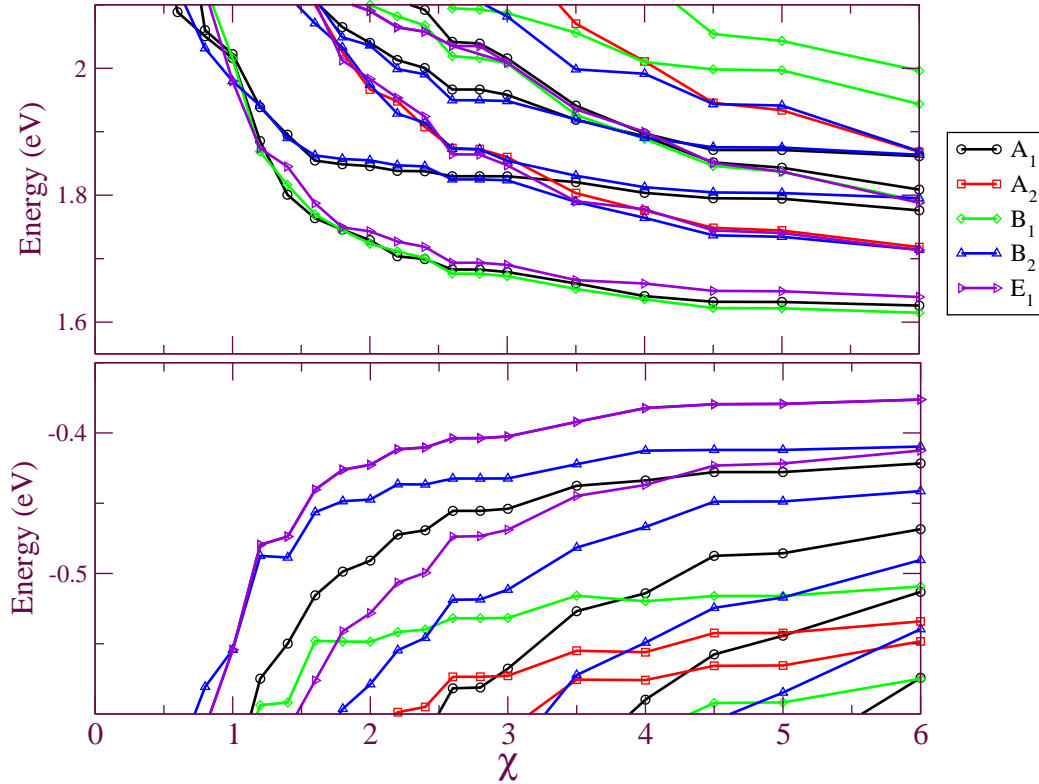


Figure 4.2: Energy levels for a set of silicon ellipsoidal nanocrystals, with  $a = 1$  nm, as a function of the aspect ratio  $\chi$ . The lines are guides for the eyes.

and the HOMO energy levels have a well defined symmetry, as we already noted for spherical nanocrystals. In fact, the lowest unoccupied states form a quasi-degenerate energy level, with the 4 states coming from the  $A_1 + B_1 + E_1$  representation. Instead, the top of the occupied states has a bi-dimensional  $E_1$  symmetry. And both the first LUMO and HOMO states are well separated from the other levels<sup>1</sup>. From Fig. 4.2 it clearly appears the quantum confinement effect, related to the increase of the number of Si atoms with

<sup>1</sup> It is worth noting that, as we have recently shown [90,91], there is a correspondence of the LUMO states calculated within TB, and within the EMA. Each EMA state comes out from a single bulk conduction band minimum in the first Brillouin Zone. The analysis of the  $k$ -space projections of the LUMO states confirms this feature. We shall come back in the next section on this point.

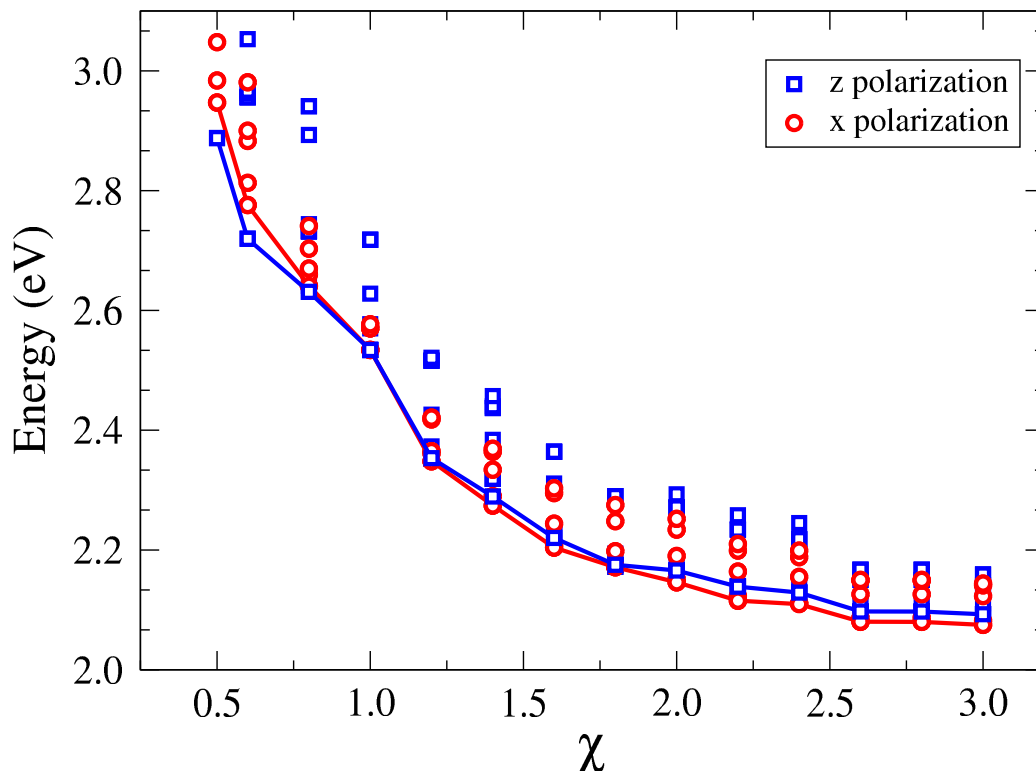


Figure 4.3: Lowest interband transition energies for a set of ellipsoids with  $a = 1$  nm. The circles represent the parallel polarized transitions, while the squares represent the perpendicular polarization, with respect to the ellipsoid symmetry axis. The lines highlight the first dipole-allowed transition.

$\chi$ . In fact, as we have seen in the previous chapter for spherical nanocrystals (see Fig. 3.1), the quantum confinement effect consists in a decrease of the LUMO energy, and an increase of the HOMO energy, on increasing the number of atoms. However, while in the limit of huge number of atoms, the sphere energy levels tend to the bulk band energies, the ellipsoid levels tend to the quantum wire limit, as we have verified. In fact, while for small values of  $\chi$  the energy levels have an oscillating behavior, already for  $\chi > 2$  the edge curves become very flat, tending to a constant value.

In Fig. 4.3 the transition energies are shown. Using the dipole selection

rules for the ellipsoid symmetry group, the polarization of each transition has been inferred. Even in this case the transition energy tends to become flatter and flatter for increasing values of the aspect ratio, tending to the quantum wire limit. The polarization of the first allowed transition depends very little on the geometrical aspect ratio, with a very small energy difference of the curves associated to a polarization parallel and perpendicular to the symmetry axis, shown in Fig. 4.3.

## 4.4 Dielectric properties

The silicon ellipsoids are non spherical structures. The ellipsoids that we have studied have a preferred direction, the ellipsoid symmetry axis, parallel to the [001] direction. Because of the  $D_{2d}$  symmetry, they behave as uniaxial birefringent structures, and their dielectric tensor has two independent components. According to the two kinds of polarization, there is a parallel and a perpendicular component of the dielectric tensor, with respect to the symmetry axis. The left panel of Fig. 4.4 shows the imaginary part of the dielectric tensor components. The arrow points to the first transition energy. The anisotropy effects are especially pronounced in the oblate case ( $\chi < 1$ ) where the structure has a lower number of Si atoms. For the spherical case ( $\chi = 1$ ) we retrieve the isotropic case, and the dielectric tensor is diagonal. Instead, for prolate structures ( $\chi > 1$ ), the anisotropy increases until reaching the quantum wire limit. In the right panel of Fig. 4.4 the density of states is shown for this set of ellipsoids, giving an estimation of the quantum confinement effect. Indeed, the more the nanocrystals are elongated, the more the wave-shaped, oscillating behavior becomes smooth and flat, while

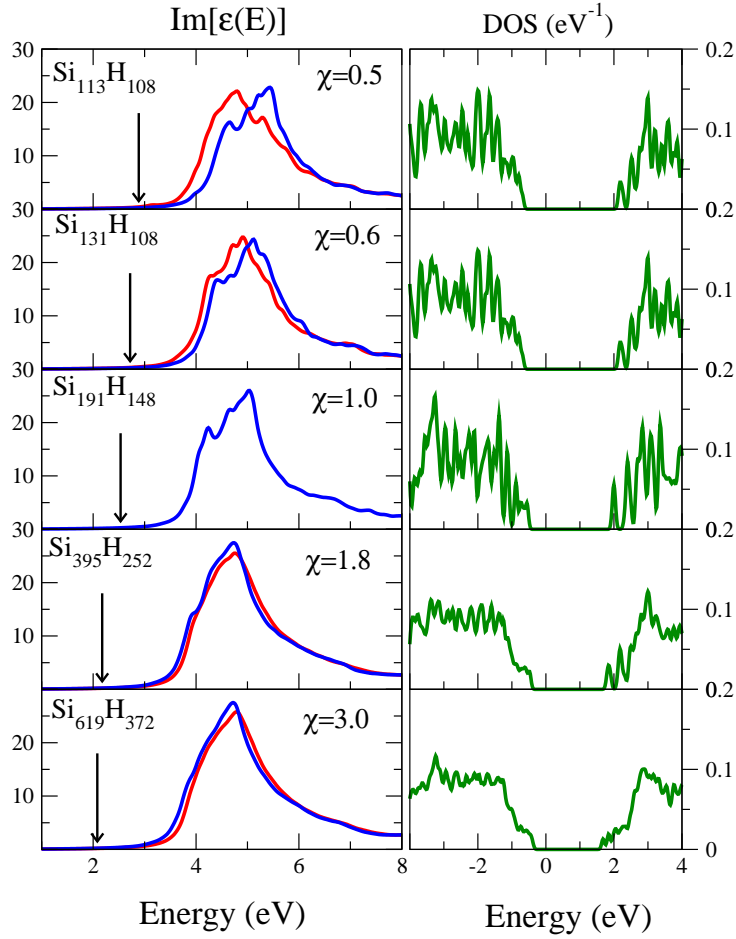


Figure 4.4: On the left: principal components of the imaginary part of the ellipsoids dielectric tensor. The red line is the perpendicular component to the symmetry axis, the blue line is the parallel component. On the right: density of states of the ellipsoids.

the HOMO and LUMO levels get closer to each other.

In order to check the convergence of the ellipsoid dielectric tensor on increasing the aspect ratio, we have explicitly calculated the quantum wire dielectric tensor. A comparison between the  $\chi = 3$  prolate ellipsoid, and the 1 nm radius quantum wire, is shown in Fig. 4.5, for both the dielectric tensor and the HOMO-LUMO gap. This is not a trivial check, being the two

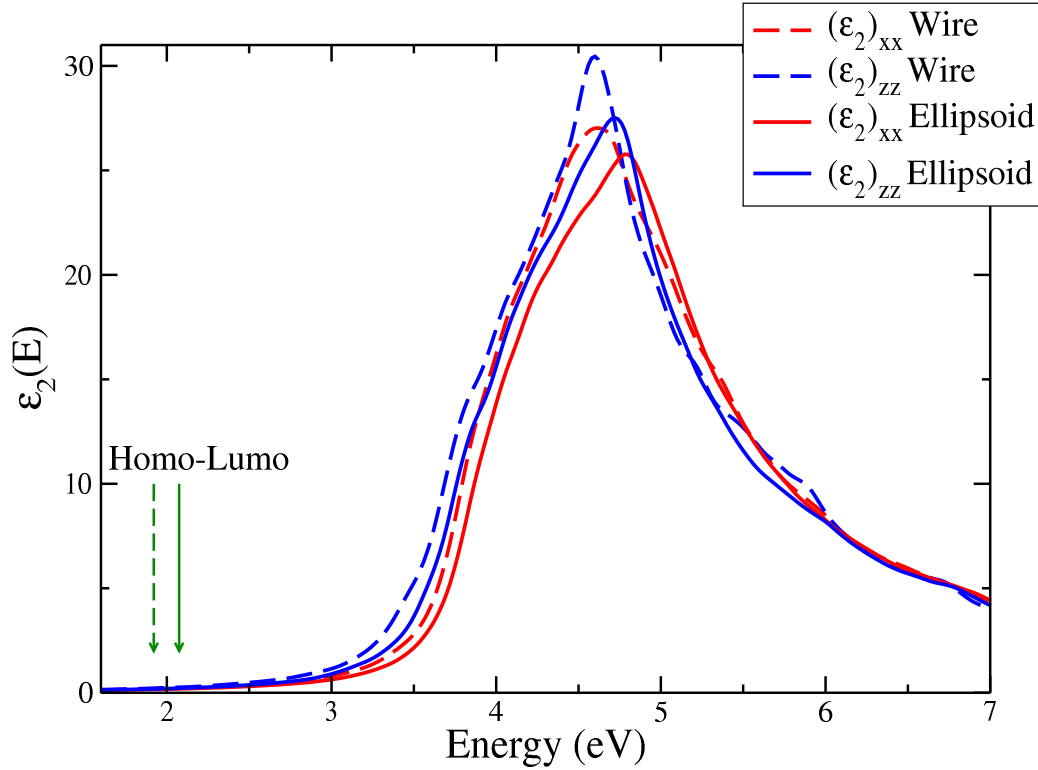


Figure 4.5: Comparison between an ellipsoid with  $a = 1$  nm,  $\chi = 3$  and a cylindrical quantum wire having the symmetry axis along the [001], and a circular section whose radius measures  $r = 1$  nm. The imaginary part of the dielectric function is shown, and the arrows point to the HOMO-LUMO transition energy.

results derived from independent calculations. It comes out that the  $\chi = 3$  ellipsoid essentially behave as the wire. This is not surprising, in that the number of Si atoms along the  $z$  direction is huge, and so we expect that the quantum confinement has a non negligible effect only along the other directions. It is worth noting that our calculated dielectric tensor is consistent with recent ab-initio calculations. In Ref. [92], using a Density Functional approach, Zhao has studied the imaginary part of the dielectric tensor for Si wires with different orientations. His results for a  $d = 2.2$  nm quantum wire are in a fair agreement, both in the curves intensities and in the peaks

energies, with our TB results.

It is useful to give a quantitative estimation of the optical anisotropy effects by introducing the degree of linear polarization for the imaginary part of the dielectric function<sup>2</sup>:

$$\rho = \frac{\text{Im} [\epsilon_{\parallel} - \epsilon_{\perp}]}{\text{Im} [\epsilon_{\parallel} + \epsilon_{\perp}]}.$$
 (4.3)

The degree of linear polarization  $\rho$  is a good measurement of the anisotropic ratio of the ellipsoidal nanocrystal optical properties. In fact,  $\rho = 0$  means that the imaginary part of the dielectric tensor is diagonal and therefore isotropic. Positive values of  $\rho$  are for a polarization along the  $z$  direction, while negative values of  $\rho$  are found when there is a preferred  $xy$  plane polarization of the absorbed light. In Fig. 4.6 the calculated  $\rho(E)$  is shown for our set of  $a = 1$  nm ellipsoidal nanocrystals. It is clear that, in the spherical case, we have an isotropic dielectric tensor, with  $\rho = 0$  (dashed line). It is interesting to study the variations of  $\rho$  when the nanocrystal shape changes. First of all, Fig. 4.6 shows a change of symmetry, for each nanocrystal, at a constant energy of nearly 5 eV. This is a nice feature, and a comparison with experimental data would be of great interest. A symmetry change of sign is observed when the nanocrystals change their shape from oblate to prolate. In the range of energies lower than 5 eV, oblate nanocrystals have a negative degree of linear polarization. Instead,  $\rho$  is positive for prolate ellipsoids. This behavior reflects the features of Fig. 4.4.

Finally, we have calculated the absorption gap starting from the integral absorption cross section, using the expressions defined in the previous chapter. In Fig. 4.7 we show the calculated cross section for our set of  $a = 1$

---

<sup>2</sup> This definition has been given according to the definition in Eq. (4.1) usually used for the PL intensity [87, 93].

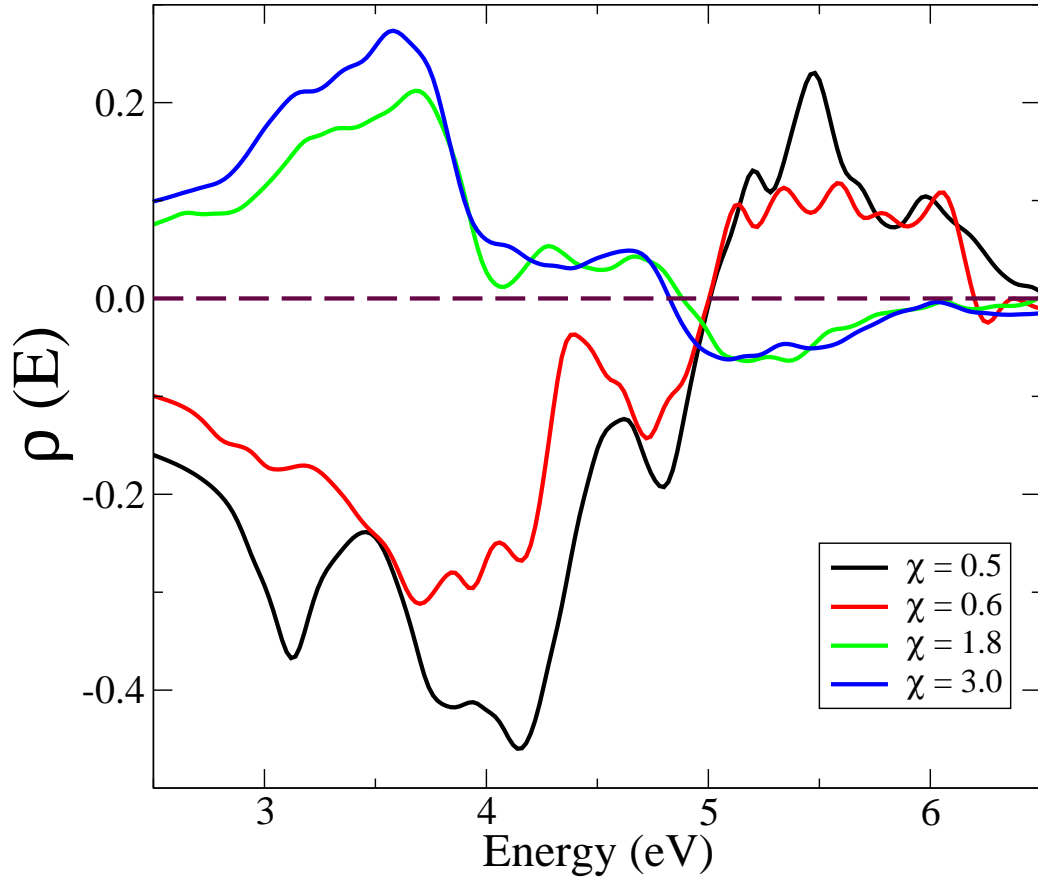


Figure 4.6: Degree of linear polarization  $\rho$  for the imaginary part of the ellipsoids dielectric function, for different values of the aspect ratio. In the case of oblate structures, the anisotropic ratio is negative, greater in modulus for more oblate ellipsoids. In the opposite case (prolate structures), the ratio is positive.

nm ellipsoids. These curves are obviously very similar to the imaginary part of the dielectric function, but the cross section has the advantage of being a measurable quantity. Starting from the definition given in Eq. (3.6), we have calculated the absorption threshold for ellipsoidal nanocrystals. In Fig. 4.7 we show both the first dipole-allowed transition energy (black arrow) and the absorption gap (red-blue arrows). The interesting result is that, while the first transition is almost independent of the polarization of the radiation,

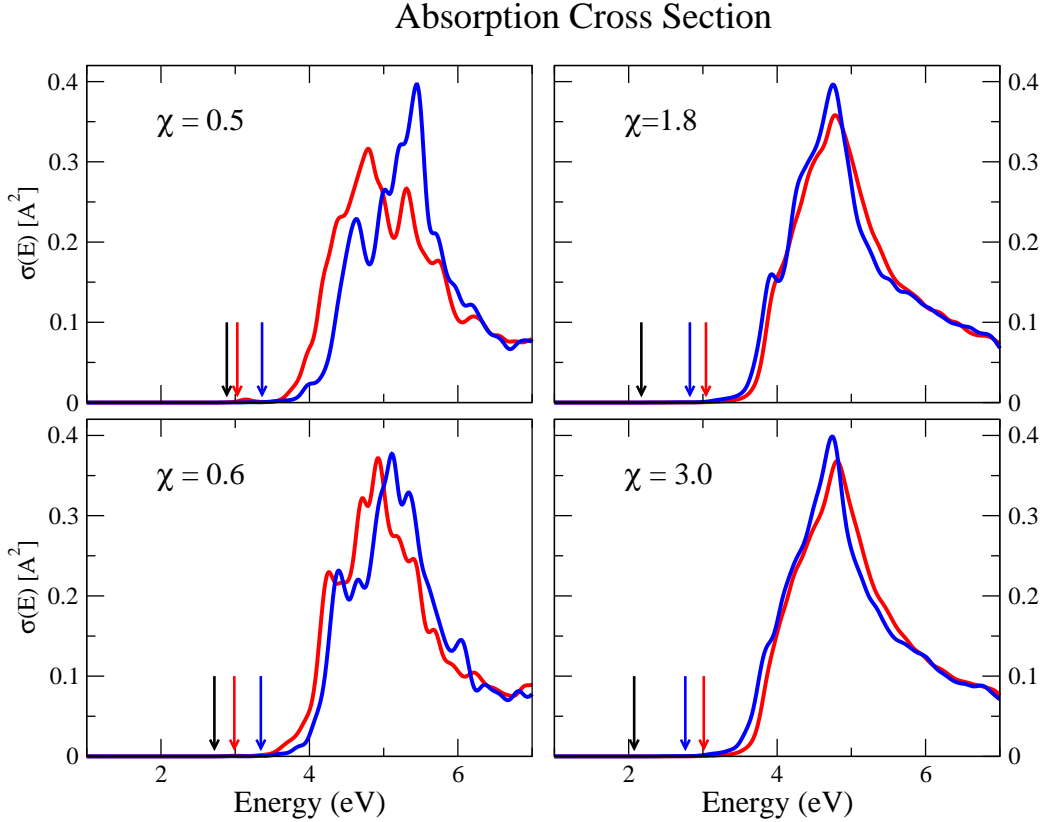


Figure 4.7: Absorption cross section for a set of Si ellipsoids having  $a = 1$  nm, as a function of the aspect ratio  $\chi$ . The red and the blue curves refer respectively to the perpendicular and the parallel polarization, with respect to the ellipsoid axis. The black arrow is the first transition energy, which depends very little on the polarization. Instead, the red and the blue arrows indicate the absorption thresholds for polarization respectively perpendicular and parallel to the  $z$  axis.

as we have already observed in Fig. 4.3, there is a significant dependence of the absorption gap on it.

Starting from the dielectric tensor, we have calculated the static dielectric constant for our ellipsoids. Our results are shown in Fig. 4.8. It is worth noting that, while the first-transition energy depends very weakly on the polarization (except that for very flattened structures), the dielectric constant can change quite a lot, just like we have seen for the optical gap. As in the

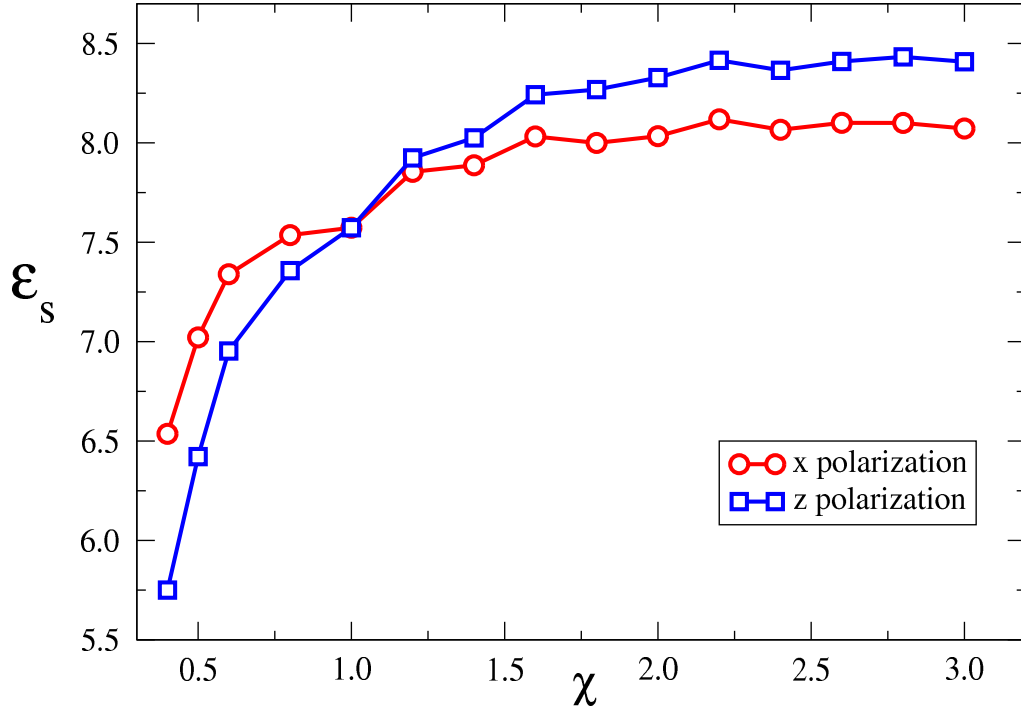


Figure 4.8: Principal components of the static dielectric tensor for a set of ellipsoids with a fixed semi-axis  $a = 1$  nm. The circles and the squares correspond, respectively, to the perpendicular and parallel component with respect to the ellipsoid symmetry axis.

previous figures, the largest effects are visible for oblate structures ( $\chi < 1$ ), while in the limit of very elongated nanocrystals the curves retrieve the quantum wire limit.

We want to mention here that the RPA calculations usually overestimate the perpendicular component of the dielectric tensor. In fact, we are not taking into account the local field effects, that can play an important role when the size becomes very small, as it has been shown for small Si clusters [74, 79]. In the case of an elongated structure, we have a confinement effect only along a single direction, and so the local field effects are important especially for the perpendicular components, with respect to the symmetry

axis. This feature has been recently shown for carbon nanotubes (see, for example, Ref. [94]). From a physical point of view, the depolarization effects are due to the charge accumulation on the nanocrystal surface which, for non spherical nanocrystals, gives different contributions for the different components of the external electric field [30].

## 4.5 Energy levels of large ellipsoids

In the second part of this chapter we discuss the LUMO states of huge ellipsoidal nanocrystals. First, we have studied a set of fixed-volume ellipsoidal nanocrystals. We define the ellipsoid equivalent radius as the radius of a sphere having the same volume of the ellipsoid. For these structures, the number of Si atoms is almost constant. In Fig. 4.9 we show, as an example, an elongated nanocrystal having an equivalent radius of 2 nm and an aspect ratio  $\chi = 2$ . It is constituted by 1675 Silicon and 660 Hydrogen atoms.

We have studied ellipsoids with an equivalent radius of 3 nm, having a symmetry axis along the [001] lattice direction. This size has been suggested by the fact that in most cases this is the average nanocrystal dimension obtained with different growth methods [59]. In Fig. 4.10 we show the results for the six LUMO states as a function of the aspect ratio  $\chi$ . We label the energy levels with the irreducible representations of the  $D_{2d}$  symmetry group. The energies are measured from the bottom of the first bulk conduction band. In the same figure we also show the Effective Mass Approximation results. We know that, according to the EMA, each nanocrystal state can have origin from either the 2 bulk conduction band minima which lie along the [001] direction (the  $k_z$  valleys), or the 4 minima lying in the perpendicular plane

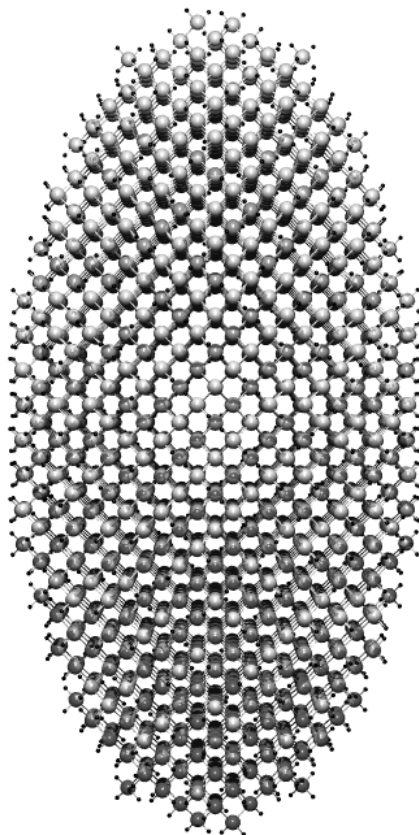


Figure 4.9: This is the  $Si_{1675}H_{660}$  TB nanocrystal. It is an ellipsoid, having  $a = 1.59$  nm, and  $c = 3.18$  nm. It has an equivalent radius  $r_{eq} = 2$  nm, and an aspect ratio  $\chi = 2$ .

to  $[001]$  (the  $k_x - k_y$  valleys). Within the EMA, we are able to calculate all the LUMO energy states coming from the  $k_z$  valleys (solid line in figure) and a unique point coming from the  $k_x - k_y$  valleys (filled circle), by reducing the EMA equations to a Schrödinger-like equation with hard-wall ellipsoidal boundary conditions [90,95]. From an analysis based on the EMA

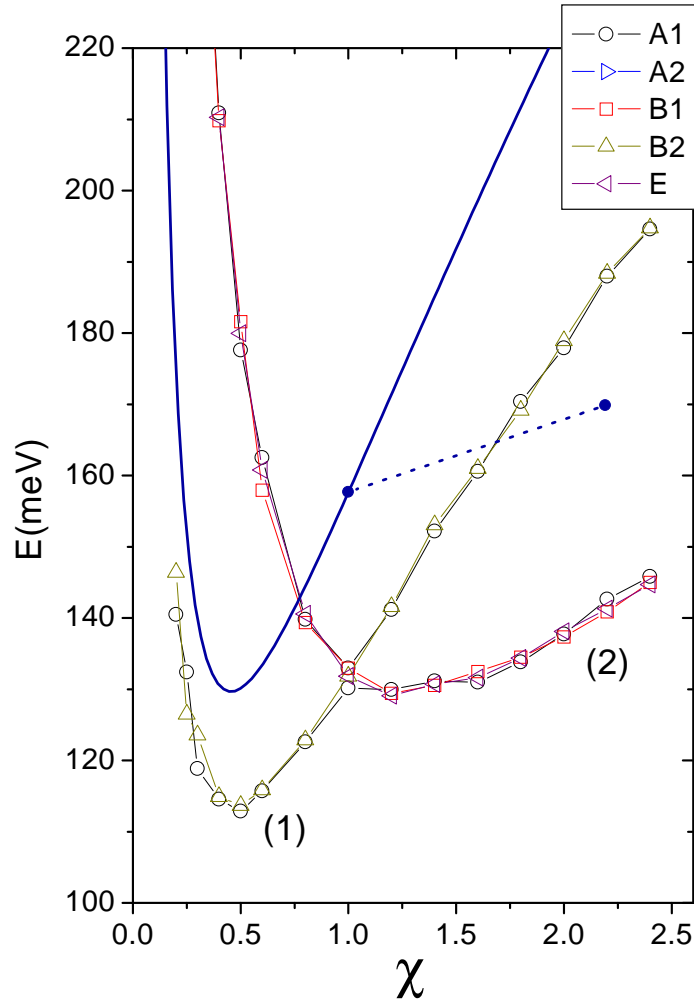


Figure 4.10: LUMO states for a set of volume-fixed ellipsoidal nanocrystals. The equivalent radius is 3 nm. The energies have been measured from the lowest bulk conduction band energy. The solid line is a EMA result. The states have been labelled according to the irreducible representations of the  $D_{2d}$  symmetry group. The lines are a guide for the eyes.

equations [90], it comes out a symmetry change for the LUMO states, when the shape changes from oblate to prolate. In fact, as it can be argued from Fig. 4.10, for flattened ellipsoids the first LUMO levels are 2-degenerate, and they come from the  $k_z$  valleys (solid line), while they are 4-degenerate for

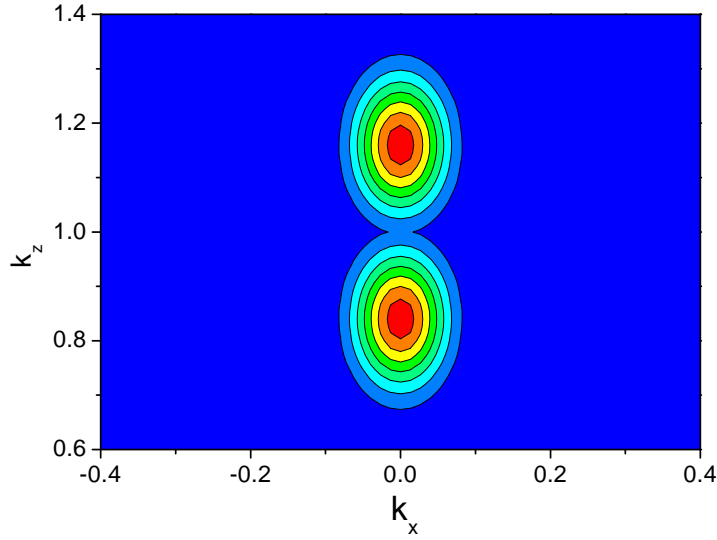


Figure 4.11:  $k$ -space projection of the first LUMO state, for a flattened ellipsoid with an equivalent radius of  $r = 3$  nm and an aspect ratio  $\chi = 0.5$ .

elongated ellipsoids, with states coming from  $k_x - k_y$  valleys (dashed line). For the sphere ( $\chi = 1$ ) we retrieve a 6-fold degenerate LUMO level. A nice feature of such huge structures is the close agreement of the TB calculations with the EMA results.

From the TB point of view, we see that the LUMO states have the symmetry either of the two 1D  $A_1, B_2$  (the points labelled as (1) in figure), or of the two 1D  $A_1, B_1$  and the 2D  $E_1$  irreducible representations (the points labelled as (2) in figure), when the ellipsoids are, respectively, oblate or prolate. A nice confirmation of the behavior of the states, that we have argued from the correspondence with the EMA results, is the  $k$ -space projection. In Fig. 4.11 we show the projection in the  $k_y = 0$  plane of the first Brillouin zone, of the first  $A_1$  LUMO state, for the oblate ellipsoid with  $\chi = 0.5$ . The only non null components come out from the  $k$  points in the vicinity of the  $k_z$  valleys,

which lie at about  $\pm(0, 0, 0.83)2\pi/a$ . On the other hand, we have verified that the first  $A_1$  LUMO state, for prolate ellipsoids, has non null components only in the neighborhood of the 4 valleys lying in the  $k_z = 0$  plane. An interesting feature of the curves in Fig. 4.10 is that the minimum energy is not in correspondence of the spherical nanocrystal. Instead, the structure with the minimum energy is a flattened ellipsoid with  $\chi \sim 0.5$ . This non obvious feature is a consequence of the Effective Mass tensor anisotropy in the bulk silicon. We want to point out that, once again, we find out that the bulk features of a material are reflected into the nanocrystalline electronic properties.

In a second step, we have studied a set of [001] ellipsoid nanocrystals, keeping fixed the  $a$  semiaxis, and varying the aspect ratio  $\chi$ . Even in this case, we consider very huge structures, choosing  $a = 3$  nm. The number of silicon atoms for these nanocrystals increases almost linearly with  $\chi$ . Therefore, flattened ellipsoids have less atoms, while in the limit of large values of  $\chi$ , we expect to retrieve the quantum wire limit. In Fig. 4.12 we show our TB results, including even in this case the EMA results coming from the  $k_z$  valleys (solid lines). We point out the change of symmetry. While for flattened ellipsoids the LUMO states are twofold quasi-degenerate, coming from the  $k_z$  valleys (indicated as (1) in figure), the prolate ellipsoid LUMO states are fourfold quasi-degenerate, and they come from the  $k_x - k_y$  valleys (indicated as (2) in figure). While for oblate ellipsoids, the LUMO curves are very steep, on increasing the aspect ratio they become more and more flattened, and we expect that they tend to a constant value, corresponding to the quantum wire limit, on the basis of the comparison that we have done in the previous

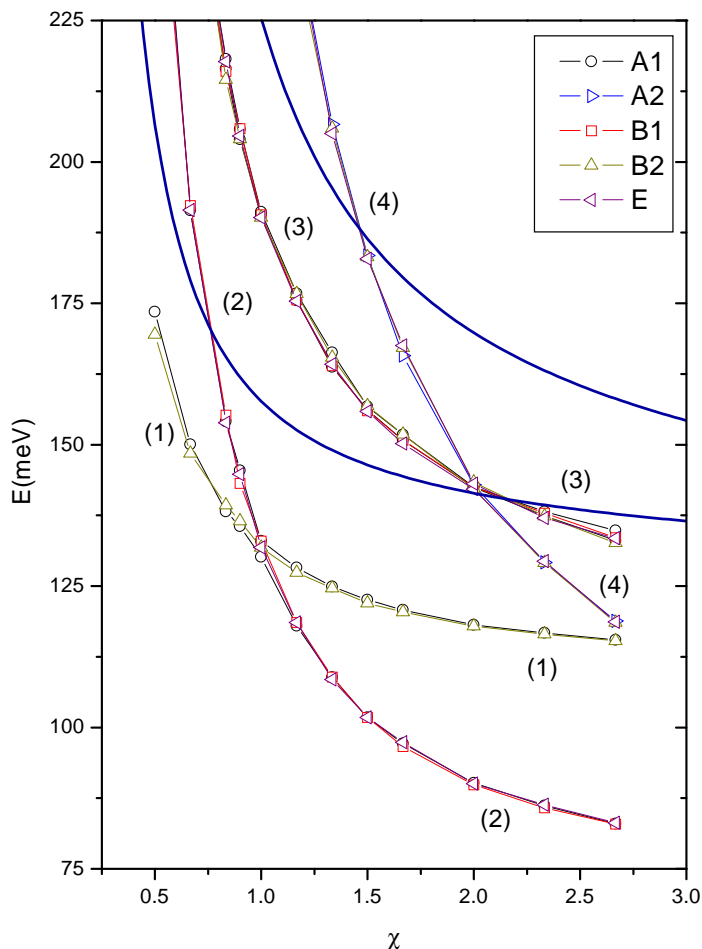


Figure 4.12: LUMO states for a set of  $a = 3$  nm Si ellipsoids. The states have been labelled according to the irreducible representations of the  $D_{2d}$  symmetry group. The lines are a guide for the eyes. The solid lines are EMA results for the states derived from the  $k_z$  valleys.

section. Even in this case we have verified that the TB nanocrystal states essentially come out from either the  $k_z$  or the  $k_x - k_y$  valleys. Therefore, there is a non null overlap of the wavefunctions only for states associated to the same valley. This behavior allows us to give a criterion for the calculation

of the infrared, intraband transition energies. In fact, only states with a non null  $k$ -space overlap corresponds to an allowed transition, with non negligible oscillator strengths (as we have seen in the previous chapter). Therefore, we have calculated, on increasing  $\chi$ , the infrared transition energies involving the lowest unoccupied state, only considering the transitions between states derived from the same valley (EMA allowed transitions). Then, between all the EMA-allowed transitions, we have selected the  $D_{2d}$  dipole allowed ones, and we have calculated the TB transition energies. Using the symmetry group selection rules we have then inferred the polarization associated to each transition. In Fig. 4.13 we show our results. According to the (1) – (2) ground state change of symmetry, we have a change of polarization of the lowest transition energy from the first LUMO state. Indeed, Fig. 4.13 shows that the polarization of the transition from the first lowest energy state changes from  $z$  ( $\chi < 1$ ) to  $x - y$  ( $1 < \chi < 2$ ) to  $z$  ( $\chi > 2$ ). The large size of these nanocrystals leads to small transition energies, which would be difficult to detect experimentally. However, such huge structures show that the EMA results are retrieved, which gives a further confirmation of the theory. Smaller nanocrystals show larger transition energies, within hundreds meV. For example, in Fig. 4.14 we show the infrared transition energies for a set of  $a = 1.5$  ellipsoids. The comparison with Fig. 4.13 shows that, due to the smaller size, higher transition energies are retrieved, even if the same trend with the aspect ratio is observed. The  $k$ -space overlap is responsible for the significant breaking of the degeneracy.

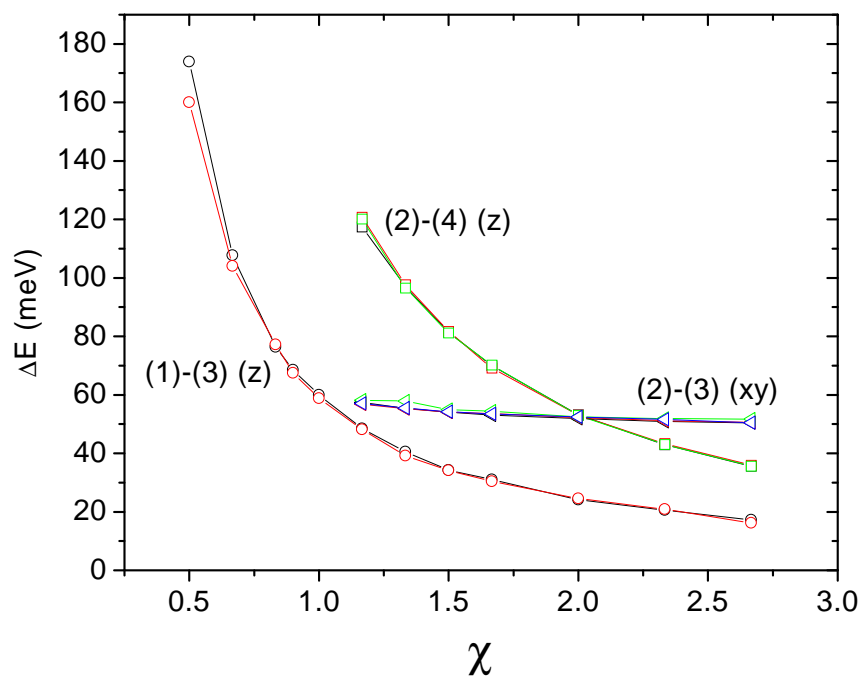


Figure 4.13: Infrared transition energies for ellipsoids with  $a = 3$  nm, on increasing the aspect ratio. The first LUMO states corresponds to (1) and (2), for, respectively, oblate and prolate structures. In the considered range of aspect ratios the lowest transition allowed from the ground state changes from (1)-(3) ( $z$  polarization) to (2)-(3) ( $x - y$  polarization) to (2)-(4) ( $z$  polarization), when the aspect ratio changes from  $\chi < 1$  to  $1 < \chi < 2$  to  $\chi > 2$ . The connecting lines are guides for the eyes.

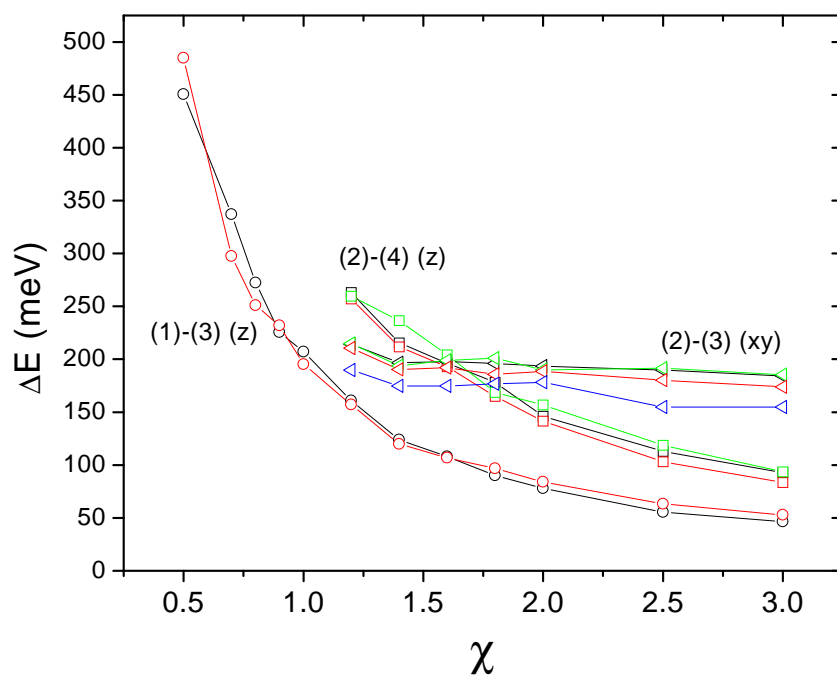


Figure 4.14: Infrared transition energies for ellipsoids with  $a = 1.5$  nm, on increasing the aspect ratio. The connecting lines are guides for the eyes.



# Conclusions

The quantum confinement effect is a well known feature of semiconductor nanocrystals. It especially consists in an increase of both the band gap and the radiative electron - hole recombination rate on decreasing the nanocrystal size. In silicon structures this effect is especially pronounced, and it has spectacular consequences, as the huge observed photoluminescence from silicon nanocrystals has demonstrated. Nevertheless, the mechanisms at the basis of the photoluminescence phenomena have not been completely understood.

We have analyzed in detail the optical properties of spherical structures, investigating the role of the bulk silicon indirect band gap. A fruitful comparison between the electron-hole radiative recombination times, the oscillator strengths and the  $k$ -space projections into bulk silicon Bloch functions has demonstrated a different behavior between small and large nanocrystals. Small nanocrystals have a *direct gap - like* behavior, with very short radiative lifetimes ( $ns$ ) and huge  $k$ -space overlaps between HOMO and LUMO states. On the opposite hand, large nanocrystals retrieve the indirect band gap features of the bulk silicon, large radiative lifetimes ( $ms$ ) and very small oscillator strengths. This behavior is confirmed by the experiments. We have verified the goodness of our theoretical framework showing very interesting comparisons with the experimental data. Indeed, our calculation tool,

an  $sp^3$   $3^{\text{rd}}$  nearest neighbor Tight Binding method, gives an excellent band structure and a good dielectric function for the bulk silicon. The method has been shown to be very efficient in the study of nanocrystals, because of its real space formulation, that leads to very sparse Hamiltonian matrices. This feature has been used, together with the group theory, to largely reduce the overall computational time. Within the Tight Binding method, we have shown to be able to study both very small and very large structures, ranging from a few atoms to several thousands atoms, keeping a good consistency with the other theoretical models and the experimental data.

While the quantum confinement effect due to the silicon nanocrystals change of size is a subject studied since many years ago, the shape effects are a quite recent issue. From the experimental point of view, silicon ellipsoidal nanocrystals have been recognized as the sources of the photoluminescence anisotropy of porous silicon samples. The nanocrystals that we have studied have a revolution axis along the [001] lattice direction. We have studied them keeping fixed the semiaxes in the plane orthogonal to the symmetry direction, and changing the ellipsoid aspect ratio. These structures have properties which range, on increasing the aspect ratio, from the quantum disk, to the spherical nanocrystal, to the quantum wire limit. We have analyzed the energy levels and the optical properties for a set of small ellipsoidal nanocrystals, focusing our work on the optical anisotropy of the dielectric tensor on changing the geometrical anisotropy. A nice check has been the comparison between an elongated ellipsoid and its quantum wire limit, which shows that, already for a not too large anisotropic ratio, the ellipsoid essentially behaves as a quantum wire. This feature is related to the number of

silicon atoms which lies along the ellipsoid revolution direction.

Next, we have studied the LUMO energy levels for a set of large silicon ellipsoids. A nice goal has been the merging of our TB results to the Effective Mass Approximation results. This has been a further confirmation of the goodness of our computational method. Because of the anisotropy of the bulk silicon Effective Mass tensor in the conduction band minima, the nanocrystal LUMO states and infrared transition energies have a non trivial trend on increasing the ellipsoid aspect ratio. It has been the first time that such a study has been performed.



# Appendix A

## Symmetries

An ideal crystal is characterized by having all the atoms located in regular positions, in such a way to form a periodic structure. All the atomic positions are related by means of a discrete set of transformations, that forms the symmetry group of the crystal, that in the following we shall call the crystal *space group*  $G$ . The space group is formed by translations and rotations, and the most general transformation can be written in the form  $\{\alpha|\mathbf{a}\}$ , that we intend acting on vectors (spatial transformations) or on functions (operators) according to the following prescription<sup>1</sup>:

$$\{\alpha|\mathbf{a}\}\mathbf{v} = \alpha\mathbf{v} + \mathbf{a} \quad (\text{A.1})$$

$$\{\alpha|\mathbf{a}\}f(\mathbf{r}) = f(\{\alpha|\mathbf{a}\}^{-1}(\mathbf{r})) = f(\alpha^{-1}(\mathbf{r} - \mathbf{a})). \quad (\text{A.2})$$

In this notation,  $\alpha$  is the rotational part, while  $\mathbf{a}$  is a space displacement vector. The crystal atomic positions transform into each other under the space group operations. Therefore, the crystal geometry is characterized by

---

<sup>1</sup> For a general view on the group theory, we suggest the reading of the book [96]. A good review on the use of symmetries in solid state physics can be found in [9].

the relationships:

$$\{\alpha|\mathbf{a}\}\mathbf{v}_i = \mathbf{v}_j, \quad (\text{A.3})$$

where the symmetry operations  $\{\alpha|\mathbf{a}\}$  span the whole space group  $G$ , while  $\mathbf{v}_i$  ( $i = 1 \dots N$ , with  $N$  atoms inside the structure) runs on all the crystal atomic positions. In the case of an infinite structure, the lattice is invariant under a set of discrete translations. So, the space group has two fundamental subgroups. The first one contains all the *lattice translations*, which have the form:

$$T_{\mathbf{R}} = \{1|\mathbf{R}\}, \quad (\text{A.4})$$

where 1 is the identity transformation (or the identity operator). It is easy to verify that  $T_{\mathbf{R}}$  transforms as a vector following the relation:

$$\{\alpha|\mathbf{a}\}T_{\mathbf{R}}\{\alpha|\mathbf{a}\}^{-1} = T_{\alpha\mathbf{R}}. \quad (\text{A.5})$$

All the remaining operations form the so called *point group* of  $G$ , which contains elements in the form

$$\{\alpha|\mathbf{f}_i\}, \quad (\text{A.6})$$

and, in general, to each rotation  $\alpha$  is usually associated an appropriate *fractional translation vector*  $\mathbf{f}_i$ . The lattice translation group is an abelian group, and it only has one-dimensional irreducible representations, which can be labelled using a  $\mathbf{k}$  vector. The irreducible representation basis functions satisfy the Bloch relation:

$$\hat{T}_{\mathbf{R}}f_{\mathbf{k}}(\mathbf{r}) = e^{-i\mathbf{k}\cdot\mathbf{R}}f_{\mathbf{k}}(\mathbf{r}). \quad (\text{A.7})$$

Instead, the irreducible representations of the crystal point group are characterized by sets of transformation matrices  $\Gamma(\alpha)$ , and the basis functions

satisfy the transformation rules:

$$\{\alpha|\mathbf{f}_i\}g_\sigma(\mathbf{r}) = \sum_{\sigma'} \Gamma_{\sigma\sigma'}(\alpha^{-1})g_{\sigma'}(\mathbf{r}). \quad (\text{A.8})$$

The irreducible representations of the whole space group are characterized by both a  $\mathbf{k}$  vector and a  $n$  quantum number, and we can write their basis functions in the form  $f_{n\mathbf{k}}$ . From Eq. (A.5) and assuming still true Eq. (A.7), it follows that:

$$\hat{T}_{\mathbf{R}}\{\alpha|\mathbf{a}\}^{-1}f_{n\mathbf{k}} = \{\alpha|\mathbf{a}\}^{-1}\hat{T}_{\alpha\mathbf{R}}f_{n\mathbf{k}} = e^{-i\alpha^{-1}\mathbf{k}\cdot\mathbf{R}}\{\alpha|\mathbf{a}\}^{-1}f_{n\mathbf{k}}, \quad (\text{A.9})$$

and therefore  $\{\alpha|\mathbf{a}\}^{-1}f_{n\mathbf{k}}$  belongs to the  $\alpha^{-1}\mathbf{k}$  irreducible representation of the translation subgroup. The irreducible representations of the whole space group are defined by the transformation matrices  $D_{\mathbf{k}}(\alpha)$ , which depend on the  $\mathbf{k}$  vector, and they transform in the following way:

$$\{1|\mathbf{R}\}f_{n\mathbf{k}} = e^{-i\mathbf{k}\cdot\mathbf{R}}f_{n\mathbf{k}} \quad (\text{A.10})$$

$$\{\alpha|\mathbf{f}_i\}f_{n\mathbf{k}} = \sum_{n'} D_{nn'}(\alpha^{-1})_{\mathbf{k}}f_{n'\alpha\mathbf{k}}. \quad (\text{A.11})$$

The TB atomic orbital basis set is usually constructed in such a way that the orbitals contained inside a unit cell are the basis functions for a given point group representation. Using the Dirac notation for the orbitals, we can write the transformation properties of the TB basis set as:

$$\{\alpha|\mathbf{a}\}|\sigma, \boldsymbol{\mu}, \mathbf{R}\rangle = \sum_{\sigma'} \Gamma_{\sigma\sigma'}(\alpha^{-1})|\sigma', \{\alpha|\mathbf{a}\}\boldsymbol{\mu}, \alpha\mathbf{R}\rangle. \quad (\text{A.12})$$

$\Gamma$  is the transformation matrix of a point group representation. For example, in the case of diamond-like crystals, point group is the cubic  $O_h$  group, and the  $s$  and  $p$  functions are chosen in such a way to transform as the totalsymmetric  $A_{1g}$  and the 3-dimensional  $T_{1u}$  irreducible representations.

The *character* of a representation with respect to a symmetry operation is defined as the trace of the transformation matrix of a basis function set of that representation. For instance, let's consider a group  $G = \{\alpha_i\}_{i=1,h}$ , and a representation  $\mu$  of  $G$ , having  $l_\mu$  basis functions  $g_n^\mu$  which transform as:

$$\hat{\alpha}_i g_n^\mu = \sum_m D(\alpha_i)_{mn}^\mu g_m^\mu. \quad (\text{A.13})$$

The character of the representation is defined as the trace of  $D$ :

$$\chi^\mu(\alpha_i) = \sum_n D(\alpha_i)_{nn}^\mu. \quad (\text{A.14})$$

A fundamental result of the group theory is that the projection operator into the space spanned by the representation basis functions, can be written as

$$\hat{P}^\mu = \frac{l_\mu}{h} \sum_{i=1}^h \chi^\mu(\alpha_i) \hat{\alpha}_i. \quad (\text{A.15})$$

The huge importance of the projection operators in physics lies in the fact that the Hamiltonian eigenstates are basis functions of an irreducible representation of the symmetry group. This means that the Hamiltonian matrix is formed by independent blocks, when it is written in a symmetrized function basis set. Using the projection operators, we have symmetrized the TB atomic orbitals with respect to the irreducible representations of the nanocrystal symmetry group. In the symmetrized TB basis set the Hamiltonian is constituted by independent blocks, each one with a smaller size than the original matrix. In this way we have largely reduced the overall diagonalization computational time.

# Appendix B

## Character Tables

In this section we report the symmetry group character tables of the nanocrystals that we have studied<sup>1</sup>.  $O_h$  is the point group of the bulk silicon structure,  $T_d$  is the symmetry group of the TB spherical nanocrystals, while  $D_{2d}$  is the symmetry group of the ellipsoidal nanocrystals.  $O_h$  is constituted by 48 elements,  $T_d$  and  $D_{2d}$  are, respectively, 24- and 8-dimensional. For  $D_{2d}$  we explicitly write the group elements, as transformations of the cartesian coordinate system. On the left of the irreducible representations, we report their symmetry with respect to the group transformations, in terms of first- or second-order polynomials. For an explicit definition of the character table, and for a clarification of the crystallographic notation, see [96]. Then, we report the compatibility relations between the irreducible representations of the  $T_d$  and  $D_{2d}$  symmetry groups. The compatibility table is important for understanding how the energy levels split when the nanocrystal shape changes from spherical to ellipsoidal.

---

<sup>1</sup> The character tables have been taken from the Bilbao Crystallographic Server, at the link: <http://www.cryst.ehu.es/rep/point>.

$T_d$		E	$8C_3$	$3C_2$	$6\sigma_d$	$6S_4$
$x^2 + y^2 + z^2$	$A_1$	1	1	1	1	1
	$A_2$	1	1	1	-1	-1
$(2z^2 - x^2 - y^2, x^2 - y^2)$	$E_1$	2	-1	2	0	0
$(j_x, j_y, j_z)$	$T_1$	3	0	-1	-1	1
$(x, y, z), (xy, xz, yz)$	$T_2$	3	0	-1	1	-1

Table B.1: Character table of the  $T_d$  symmetry group.

$D_{2d}$		E	$C_2$	$2S_4$	$2C'_2$	$2\sigma_d$
		$(xyz)$	$(\bar{x}\bar{y}\bar{z})$	$(\bar{y}\bar{x}\bar{z}), (\bar{y}\bar{x}\bar{z})$	$(x\bar{y}\bar{z}), (\bar{x}y\bar{z})$	$(yxz), (\bar{y}\bar{x}z)$
$x^2 + y^2, z^2$	$A_1$	1	1	1	1	1
$j_z$	$A_2$	1	1	1	-1	-1
$x^2 - y^2$	$B_1$	1	1	-1	1	-1
$z, xy$	$B_2$	1	1	-1	-1	1
$(x, y), (xz, yz), (j_x, j_y)$	$E_1$	2	-2	0	0	0

Table B.2: Character table of the  $D_{2d}$  symmetry group.

$T_d$	$A_1$	$A_2$	$E_1$	$T_1$	$T_2$
$D_{2d}$	$A_1$	$B_1$	$A_1 + B_1$	$E_1 + A_2$	$E_1 + B_2$

Table B.3: Compatibility relations between the  $T_d$  and  $D_{2d}$  symmetry groups.

$O_h$		E	$6C_4$	$3C_2$	$8C_3$	$6C'_2$	$i$	$6S_4$	$3\sigma_d$	$8S_3$	$6\sigma'_d$
$x^2 + y^2 + z^2$	$A_{1g}$	1	1	1	1	1	1	1	1	1	1
	$A_{1u}$	1	1	1	1	1	-1	-1	-1	-1	-1
	$A_{2g}$	1	-1	1	1	-1	1	-1	1	1	-1
	$A_{2u}$	1	-1	1	1	-1	-1	1	-1	-1	1
$(2z^2 - x^2 - y^2, x^2 - y^2)$	$E_g$	2	0	2	-1	0	2	0	2	-1	0
	$E_u$	2	0	2	-1	0	-2	0	-2	1	0
	$T_{2u}$	3	-1	-1	0	1	-3	1	1	0	-1
$(xy, xz, yz)$	$T_{2g}$	3	-1	-1	0	1	3	-1	-1	0	1
$(x, y, z)$	$T_{1u}$	3	1	-1	0	-1	-3	-1	1	0	1
$(j_x, j_y, j_z)$	$T_{1g}$	3	1	-1	0	-1	3	1	-1	0	-1

Table B.4: Character table of the  $O_h$  symmetry group.



# Acknowledgments

A conclusione di questo dottorato di ricerca, vorrei ringraziare in modo particolare il Prof. Domenico Ninno, che con tanta pazienza mi ha incoraggiato nel lavoro, dandomi fiducia, e spronandomi sempre, contribuendo in modo fondamentale a questo lavoro. Vorrei ringraziare il Dr. Giovanni Cantele, per le tante fruttuose discussioni scientifiche, per i suoi preziosi consigli, e per il suo contributo alla stesura finale di questa tesi. Un ringraziamento particolare va anche al Prof. Stefano Ossicini, per il suo interessamento ed i suoi utili suggerimenti.



# Bibliography

- [1] J. C. Slater and G. F. Koster. *Phys. Rev.*, 94:1498–1524, 1954.
- [2] M. Lannoo and J. Burgoin. *Point Defects in Semiconductors I*. Springer-Verlag, 1981.
- [3] D. A. Papaconstantopoulos and M. J. Mehl. *J. Phys.: Condens. Matter*, 15:R413, 2003.
- [4] P. B. Allen, J. Q. Broughton, and A. K. McMahan. *Phys. Rev. B*, 34:859–862, 1986.
- [5] O. F. Sankey and D. J. Niklewski. *Phys. Rev. B*, 40:3979–3995, 1989.
- [6] S. Goedecker and L. Colombo. *Phys. Rev. Lett.*, 73:122–125, 1994.
- [7] L. F. Mattheiss and J. R. Patel. *Phys. Rev. B*, 23:5384–5396, 1981.
- [8] P. O. Löwdin. *J. Chem. Phys.*, 18:365, 1950.
- [9] F. Bassani and G. Pastori Pallavicini. *Electronic states and optical transitions in solids*. Pergamon Press, 1975.
- [10] J. M. Jancu, R. Scholz, F. Beltram, and F. Bassani. *Phys. Rev. B*, 57:6493–6507, 1998.

- [11] M. L. Cohen and T. K. Bergstresser. *Phys. Rev.*, 141:789–796, 1966.
- [12] J. R. Chelikowsky and M. L. Cohen. *Phys. Rev. B*, 10:5095, 1974.
- [13] J. R. Chelikowsky. *J. Phys. D*, 33:R33, 2000.
- [14] V. Heine. *Solid State Physics*, 24:1, 1970.
- [15] M. L. Cohen and V. Heine. *Solid State Physics*, 24:38, 1970.
- [16] L. W. Wang and A. Zunger. *J. Phys. Chem.*, 98:2158, 1994.
- [17] D. Helmholz and L. C. L. Yan Voon. *Phys. Rev. B*, 65:233204, 2002.
- [18] P. Vogl, H. P. Hjalmarson, and J. D. Dow. *J. Phys. Chem. Solids*, 44:365, 1983.
- [19] H. J. Monkhorst and J. D. Pack. *Phys. Rev. B*, 13:5188–5192, 1976.
- [20] A. Selloni, P. Marsella, and R. DelSole. *Phys. Rev. B*, 33:8885, 1986.
- [21] S. Y. Ren and J. D. Dow. *Phys. Rev. B*, 45:6492, 1992.
- [22] Fu Huaxiang, Ye Ling, and Xia Xide. *Phys. Rev. B*, 48:10978, 1993.
- [23] N. A. Hill and K. B. Whaley. *Phys. Rev. Lett.*, 75:1130–1133, 1995.
- [24] M. Cruz, M. R. Beltrám, C. Wang, J. Tagüeña-Martínez, and Y. G. Rubo. *Phys. Rev. B*, 59:15381, 1999.
- [25] S. Lee, L. Jonsson, J. W. Wilkins, G. W. Bryant, and G. Klimeck. *Phys. Rev. B*, 63(19):195318, 2001.
- [26] D. A. Papaconstantopoulos and E. N. Economou. *Phys. Rev. B*, 22:2903–2907, 1980.

- [27] C. Tserbak, H. M. Polatoglou, and G. Theodorou. *Phys. Rev. B*, 47:7104, 1993.
- [28] Y. M. Niquet, C. Delerue, G. Allan, and M. Lannoo. *Phys. Rev. B*, 62:5109, 2000.
- [29] L. E. Ramos, L. K. Teles, L. M. R. Scolfaro, J. L. P. Castineira, A. L. Rosa, and J. R. Leite. *Phys. Rev. B*, 63:165210, 2001.
- [30] L. D. Landau and E. M. Lifshitz. *Electrodynamics of Continuous Media*. London: Pergamon Press, 1960.
- [31] S. L. Adler. *Phys. Rev.*, 126:413, 1962.
- [32] G. Onida, L. Reining, and A. Rubio. *Rev. Mod. Phys.*, 74:601, 2002.
- [33] G. D. Mahan. *Many-Particle Physics*. Plenum Press, New York, 2nd edition, 1990.
- [34] A. L. Fetter and J. D. Walecka. *Quantum Theory of Many-Particle Systems*. McGraw-Hill, New York, 1971.
- [35] E. O. Kane. *Phys. Rev. B*, 13:3478–3483, 1976.
- [36] W. Hanke and L. J. Sham. *Phys. Rev. B*, 21:4656, 1980.
- [37] D. J. Chadi. *Phys. Rev. B*, 16:3572–3578, 1977.
- [38] A. B. Chen and A. Sher. *Phys. Rev. B*, 26:6603–6609, 1982.
- [39] L. Brey, C. Tejedor, and J. A. Vergés. *Phys. Rev. B*, 29:6840–6845, 1984.
- [40] J. R. Chelikowsky and S. G. Louie. *Phys. Rev. B*, 29:3470–3481, 1984.

- [41] N. Marzari and D. Vanderbilt. *Phys. Rev. B*, 56:12847–12865, 1997.
- [42] B. Sporkmann and H. Bross. *J. Phys.: Condens. Matter*, 9:5593, 1997.
- [43] G. D. Sanders and Y.-C. Chang. *Phys. Rev. B*, 45:9202, 1992.
- [44] R. DelSole and R. Ghirlanda. *Phys. Rev. B*, 48:11789–11795, 1993.
- [45] M. Graf and P. Vogl. *Phys. Rev. B*, 51:4940, 1995.
- [46] G. Dresselhaus and M. S. Dresselhaus. *Phys. Rev.*, 160:649, 1967.
- [47] L. C. L. Yan Voon and L. R. Ram-Mohan. *Phys. Rev. B*, 47:15500–15508, 1993.
- [48] T. B. Boykin and P. Vogl. *Phys. Rev. B*, 65:035202, 2002.
- [49] B. A. Foreman. *Phys. Rev. B*, 66:165212, 2002.
- [50] T. G. Pedersen, K. Pedersen, and T. B. Kriestensen. *Phys. Rev. B*, 63:201101, 2001.
- [51] D. E. Aspnes. *EMIS Datareviews series n 4*, pages 70–79. INSPEC, The Institution of Electrical Engineers, London and New York, 1988.
- [52] R. A. Faulkner. *Phys. Rev.*, 184:713, 1969.
- [53] C. Delerue, G. Allan, and M. Lannoo. *Phys. Rev. B*, 48:11024, 1993.
- [54] M. Lannoo, C. Delerue, and G. Allan. *Phys. Rev. Lett.*, 74:3415–3418, 1995.
- [55] C. Delerue, G. Allan, and M. Lannoo. *J. Lumin.*, 80:65, 1999.

- [56] C. Delerue, M. Lannoo, and G. Allan. *Phys. Rev. Lett.*, 84:2457–2460, 2000.
- [57] C. Delerue, M. Lannoo, and G. Allan. *Phys. Status Solidi B*, 227:115, 2001.
- [58] L. W. Wang and A. Zunger. *Phys. Rev. Lett.*, 73:1039, 1994.
- [59] A. G. Cullis, L. T. Canham, and P. D. J. Calcott. *J. Appl. Phys.*, 82(3):909–965, 1997.
- [60] D. Kovalev, H. Heckler, G. Polisski, and F. Koch. *Phys. Status Solidi B*, 215:871, 1999.
- [61] D. J. Lockwood. *Solid State Commun.*, 92:101, 1994.
- [62] E. Degoli, G. Cantele, E. Luppi, R. Magri, D. Ninno, O. Bisi, and S. Ossicini. *Phys. Rev. B*, 69:155411, 2004.
- [63] J. von Behren, T. van Buuren, M. Zacharis, E. H. Chimovitz, and P. M. Fauchet. *Solid State Commun.*, 105:317, 1998.
- [64] Qi Zhang and S. C. Bayliss. *J. Appl. Phys.*, 79:1351, 1995.
- [65] S. Furukawa and T. Miyasato. *Phys. Rev. B*, 38:5726, 1988.
- [66] M. V. Wolkin, J. Jorne, P. M. Fauchet, G. Allan, and C. Delerue. *Phys. Rev. Lett.*, 82:197, 1999.
- [67] J. P. Wilcoxon, G. A. Samara, and P. N. Provencio. *Phys. Rev. B*, 60:2704, 1999.

- [68] G. Belomoin, J. Therrien, A. Smith, S. Rao, R. Twesten, S. Chaieb, M. H. Nayfeh, L. Wagner, and L. Mitás. *Appl. Phys. Lett.*, 80(5):841–843, 2002.
- [69] M. Luppi and S. Ossicini. *J. Appl. Phys.*, 94:2130–2132, 2003.
- [70] I. Vasiliev, S. Ögüt, and J. R. Chelikowsky. *Phys. Rev. Lett.*, 86:1813, 2001.
- [71] S. Ögüt, J. R. Chelikowsky, and S. G. Louie. *Phys. Rev. Lett.*, 79:1770–1773, 1997.
- [72] C. S. Garoufalis, A. D. Zdetsis, and S. Grimme. *Phys. Rev. Lett.*, 87:276402, 2001.
- [73] H.-Ch. Weissker, J. Furthmüller, and F. Bechstedt. *Phys. Rev. B*, 69:115310, 2004.
- [74] L. X. Benedict, A. Puzder, A. J. Williamson, J. C. Grossman, G. Galli, J. E. Klepeis, J. Y. Raty, and O. Pankratov. *Phys. Rev. B*, 68:085310, 2003.
- [75] F. A. Reboredo, A. Franceschetti, and A. Zunger. *Phys. Rev. B*, 61:13073, 2000.
- [76] A. J. Williamson, J. C. Grossman, R. Q. Hood, A. Puzder, and G. Galli. *Phys. Rev. Lett.*, 89(19):196803, 2002.
- [77] R. Schäfer and J. A. Becker. *Phys. Rev. B*, 54:10296–10299, 1996.
- [78] D. L. Dexter. *Solid State Physics*, 6:353–411, 1958.

- [79] I. Vasiliev, S. Ögüt, and J. R. Chelikowsky. *Phys. Rev. B*, 65:115416, 2002.
- [80] M. Dovrat, Y. Goshen, J. Jedrzejewski, I. Balberg, and A. Sa'ar. *Phys. Rev. B*, 69:155311, 2004.
- [81] B. Delley and E. F. Steigmeier. *Phys. Rev. B*, 47:1397, 1993.
- [82] S. Y. Ren. *Phys. Rev. B*, 55:4665–4669, 1997.
- [83] G. Allan, C. Delerue, M. Lannoo, and E. Martin. *Phys. Rev. B*, 52:11982, 1995.
- [84] S. Ögüt, R. Burdick, Y. Saad, and J. R. Chelikowsky. *Phys. Rev. Lett.*, 90:127401, 2003.
- [85] C. Delerue, M. Lannoo, and G. Allan. *Phys. Rev. B*, 68:115411, 2003.
- [86] D. R. Penn. *Phys. Rev.*, 128:2093–2097, 1962.
- [87] D. Kovalev, M. Ben-Chorin, J. Diener, F. Koch, Al. L. Efros, M. Rosen, N. A. Gippius, and S. G. Tikhodeev. *Appl. Phys. Lett.*, 67:1585, 1995.
- [88] L. T. Canham. *Appl. Phys. Lett.*, 57(10):1046–1048, 1990.
- [89] S. Schuppler, S. L. Friedman, M. A. Marcus, D. L. Adler, Y. H. Xie, F. M. Ross, Y. J. Chabal, T. D. Harris, L. E. Brus, W. L. Brown, E. E. Chaban, P. F. Szajowski, S. B. Christman, and P. H. Citrin. *Phys. Rev. B*, 52:4910–4925, 1995.
- [90] G. Cantele, F. Trani, D. Ninno, and G. Iadonisi. *J. Phys.:Condens. Matter*, 15:5715, 2003.

- [91] F. Trani, G. Cantele, D. Ninno, and G. Iadonisi. *Physica E*, 22:808, 2004.
- [92] X. Zhao, C. M. Wei, L. Yang, and M. Y. Chou. *Phys. Rev. Lett.*, 92:236805, 2004.
- [93] G. Allan, C. Delerue, and Y. M. Niquet. *Phys. Rev. B*, 63:205301, 2001.
- [94] A. G. Marinopoulos, L. Reining, A. Rubio, and N. Vast. *Phys. Rev. Lett.*, 91(4):046402, 2003.
- [95] G. Cantele, D. Ninno, and G. Iadonisi. *J. Phys.: Condens. Matter*, 12:9019, 2000.
- [96] M. Tinkham. *Group Theory and Quantum Mechanics*. Mc Graw-Hill Book Company, 1964.